NASA CR-66965

THE EFFECT OF EXHAUST CONDITIONS, SURFACE WINDS, AND GEOMETRIC SCALE ON HOT GAS INGESTION FOR TWO JET VTOL CONFIGURATIONS

by PATRICK E. RYAN and WAYNE J. COSGROVE

THE EFFECT OF EXHAUST CONDITIONS, SURFACE WINDS, AND GEOMETRIC SCALE ON HOT GAS INGESTION FOR TWO JET VTOL CONFIGURATIONS

by PATRICK E. RYAN and WAYNE J. COSGROVE

ABSTRACT

The main objective of this program was to determine whether there was an effect of geometric model scale on the Inlet Temperature Rise (ITR) caused by recirculating hot exhaust gases from VTOL lift jet engines in static proximity to ground. The approach used was to conduct small-scale tests in which ITR was measured over a range of exhaust pressure ratio, exhaust gas temperature and surface wind velocity for two configurations of a jet VTOL fighter-type model containing four lift jets and comparing the results with large-scale data of similar configurations.

The small-scale tests were conducted at the Bell Aerospace Company Jet Impingement Test Facility. These tests provided a range of simulated inlet and exhaust conditions which included those typical of full-scale turbojet engines.

CONTENTS

THE EFFECT OF EXHAUST CONDITIONS,

SURFACE WINDS, AND GEOMETRIC SCALE ON HOT GAS INGESTION

FOR TWO JET VTOL CONFIGURATIONS

By Patrick E. Ryan and Wayne J. Cosgrove
Bell Aerospace Company

SUMMARY

Small-scale tests were conducted at the Bell Aerospace Company Jet Impingement Test Facility during 1969 to investigate the Inlet Temperature Rise (ITR) of two fighter-type jet VTOL aircraft configurations. This program was sponsored by the National Aeronautics and Space Administration's Langley Research Center under Contract NAS1-9584.

Two 0.24 scale configurations of a NASA jet VTOL fighter-type model were operated through a range of exhaust temperatures (900°F to 1400°F) and exhaust total pressure ratios (1.1 to 2.0) at various wind speeds (0 to 55 fps) and azimuth directions (0, 45° and 90°).

Temperature time histories measured at the simulated engine inlets were used to compute steady state ITR values. The effects of exhaust pressure ratio, exhaust gas temperature and surface winds on ITR were determined and observations on the functional dependence of the variables were made. The small-scale ITR data were then compared with large-scale data at conditions of (1) equal exhaust velocity and temperature and (2) equal buoyancy. Poor comparisons resulted from both methods of comparison, and the objective of determining an ITR scale factor was not realized.

The results indicate however, that further analyses of the data obtained in this program are warranted. This effort would serve to empirically establish a valid dynamic similarity parameter which is required to determine the existence and magnitude of an ITR scale factor.

INTRODUCTION

One of the most critical problems unique to jet VTOL aircraft when operating near the ground is hot gas ingestion or inlet temperature rise (ITR). This ingestion of heated air into the lift engine inlets can result in a severe loss in engine thrust, and could prevent or severely restrict VTOL operations in ground proximity.

Several ITR investigations have been conducted using both large and small-scale models (Reference 1 through 16) and a general discussion of the shortcomings of theoretical analysis of this problem is contained in reference 17. The results of these evaluations have provided much insight into ITR effects; however, many important questions still remain unanswered. Two of these are: (1) What are the effects of exhaust conditions (exhaust pressure ratio and exhaust gas temperature) on ITR and (2) Is there an ITR scale effect associated with geometric model scale?

The first is important because exhaust conditions are prime operating characteristics of jet engines. The effect of these characteristics on ITR is useful in the selection of power plants for jet VTOL aircraft design. In addition, this information is required to provide a valid basis for comparison between small-scale and large-scale data for the establishment of valid scaling factors.

The second question is economically important. If small-scale test data is found reliable, then the necessary future experimental investigations may be more economically accomplished through the use of small, more versatile models and test facilities.

These two questions were experimentally investigated during the course of this program. The analysis of results and pertinent conclusions are presented in this report.

2

SYMBOL LIST

D_e — nozzle effective diameter (diameter of circle whose area is equal to the sum of the areas of all the individual nozzles), ft (m)

g — acceleration due to gravity, ft/sec^2 (m/sec^2)

h — exhaust nozzle height above ground plane, ft (m)

ITR — inlet temperature rise above ambient, °F

k — constant

P — pressure, psf (N/m^2)

q_j — jet exit dynamic pressure, psf (N/m^2)

q_∞ — ground wind dynamic pressure, psf (N/m^2)

r — radial distance along ground plane from exhaust pattern center, ft (m)

R — Reynolds Number

S — wing planform area, ft^2 (m^2)

S_j — total exhaust area at nozzle exit, ft^2 (m^2)

T — Temperature, °F

ΔT_j — excess exhaust gas temperature $(T_j - T_a)$, °F = °R

V_∞ — ground wind speed, fps (m/sec)

V_j — jet exit velocity, fps (m/sec)

$\dot{w}$ — mass flow rate, lbm/sec (kg/sec)

Subscripts

a   ambient condition

bar   barometric

j   jet nozzle exit condition

T   total condition

LS   large scale

SS   small scale

Greek

β bulk coefficient of thermal expansion (reciprocal of ambient temperature), $^{\circ}R^{-1}$

δ incremental change

θ absolute temperature, $^{\circ}R$

ψ surface wind azimuth angle, deg

4

TEST FACILITY, MODEL AND INSTRUMENTATION

Jet Impingement Test Facility

The Jet Impingement Test Facility, shown in Figure 1, provides variable hot exhaust gas flows typical of conventional jet engine exhaust temperatures and pressures. Simulated engine inlet flows are induced by a vacuum producing steam ejector system. Facility controls and instrumentation readouts are located in the adjacent Aerodynamics Laboratory.

Filtered compressed air and JP-4 fuel are metered to a combustor (modified J-47 burner can) in the test area. Ignition of the fuel/air mixture is by electrical spark. The combustor exhaust flow is ducted through relatively short insulated pipes to the simulated jet engine exhaust nozzles in the model. Compressed air and fuel pressure regulator systems maintain steady exhaust flow conditions during each test. Exhaust flows with exit pressure ratios from 1.1 to 2.0 and exhaust temperatures from 500°F to 1700°F can be produced at a maximum exhaust flow rate of 2.8 lb/sec.

The main ground plane of the facility is rectangular, smooth and level to a minimum radial distance of 13 ft. (approximately 49 equivalent diameters). A trap door located in the ground plane directly beneath the model opens to ducting beneath the ground plane which carries the hot jet exhaust gases away from the test site prior to test start. This minimizes preheating of the surrounding ground plane and model during the pretest engine start operation. An auxiliary ground plane (10 ft. by 8 ft.) scaled to the dimensions of the test section platform of the NASA Langley Research Center full-scale wind tunnel was positioned approximately 12 in. above the main ground plane. This ground plane had a manually operated sliding trap door (36 in. by 18 in.) located directly below the model. The closing of this trap door initiated test start.

The hinged roof of the test facility is raised to eliminate any trapping of hot gases in the test area during test operations. During inclement weather, the roof is closed to protect the test area and equipment.

The model and model flow systems are supported from above by a single, high pressure hydraulic actuator. This provides unobstructed space around the model and permits vertical positioning of the model to be remotely controlled from the control panel in the Aerodynamics Laboratory.

A wind machine with a 6 x 10 foot exit section was used to produce simulated ground wind speeds up to 55 fps. It was variously positioned in a 90 degree arc about the test facility ground plane to provide simulated ground winds at headings (ψ) of 0, -45°, and -90° to the model.

A servo operated probe was used to measure the temperature and pressure distribution in each of the exhaust jets of the model. The device consisted of total pressure and total temperature probes connected to a hydraulic cylinder. An electrical potentiometer and servo valve system were used to remotely control the probe position with respect to the exhaust nozzle.

Model

Two 0.24 scale model configurations (top inlets and side inlets) of the NASA model described in Reference 1 were used. Both configurations featured four exhausts located in the fuselage in a rectangular arrangement and a high delta wing with a planform to jet exit area ratio (S/S_j) of 43. This aluminum–stainless steel model was thoroughly packed with thermal insulation to prevent internal heat transfer from the hot exhaust system to the inlet thermocouples. The top inlets configuration is shown mounted for tests in figure 2. The exhaust gases from the combustor were quadracated and supplied individually to each of the four 1.49 inch diameter convergent exhaust nozzles, $(D_e = 0.248$ ft). The inlet line was similarly divided such that inlet flows were induced individually through each of the four 1.92 inch diameter bellmouth inlets of the top inlets configuration and each of the side inlets. The area of each of the side inlets (approximately rectangular in cross section) was 5.88 sq. in.

Except for the aerodynamically insignificant difference at the aft end of the fuselage (see figure 3), external model surface scaling was closely maintained to provide a firm geometric basis from which ITR scale effects might be assessed. The tests were conducted with the model at constant ground heights of $h/D_e = 1.2$ and 3.0 for the side and top inlets configurations respectively.

Instrumentation

In general, instrumentation consisted of 30 gauge (AWG) bare bead iron-constantan thermocouples to measure inlet temperature time histories and pressure and temperature probes to monitor internal model flow conditions. To simplify data reduction, the thermocouples of each inlet were electrically averaged as well as individually recorded by oscillograph. The location of the inlet thermocouples for both model configurations is illustrated in figure 4. Most of the internal model flow data were recorded from manometer banks, point recorders, or gages. The temperature and pressure probes used to determine the internal flow characteristics of both model configurations were located as shown in figure 5. Nominal total inlet and exhaust flow conditions ($\overset{\circ}{w}$, T_T, P_T) were measured in the supply lines upstream of the model. Oscillographs were employed to collect permanent time histories of all the inlet temperatures, the wind conditions, and selected temperatures and pressures in the model inlet and exhaust systems.

Ambient temperature was measured by a conventional mercury thermometer as well as a specially shielded thermocouple. The two values were averaged to provide

one reading. The random (prevailing) wind conditions were sampled prior to each test using a hand held rotary arm anemometer. The surface wind produced by the wind machine was monitored by means of a tachometer (direct drive engine RPM) and recorded permanently with an oscillograph. The generated surface wind was corrected to account for random wind.

TESTS AND TECHNIQUES

During this program 159 tests were performed on the side inlets configuration and 161 tests were conducted on the top inlets configuration. These included several test runs to check repeatability, determine the effect of inlet flow rate on ITR, and obtain data at intermediate wind speeds and at low values of jet exit velocity (V_j). A summary of tests conducted is presented in table I.

The test procedure, which was the same for both configurations is outlined below:

(1) The random wind speed was measured. Most of the tests were conducted during the early morning hours to take advantage of the calm wind conditions. The random winds were generally from zero to 2 fps and no tests were conducted when random winds exceeded 5 fps.

(2) The wind machine was started and throttled to the RPM which would produce the desired nominal wind speed.

(3) The trap door was opened and the simulated engines started.

(4) After two to three minutes, which was the time required to establish the desired inlet and exhaust conditions and to heat the hardware to steady state, the steam ejector was turned on and adjusted to give the desired inlet mass flow.

(5) A check was made of the test conditions, the oscillographs were activated and the trap door was closed one to three seconds later (test start).

(6) After 16 to 20 seconds, the trap door was opened (end of test) and one to five seconds later the oscillographs were turned off.

(7) The inlet and exhaust pressure data were read from manometers and manually recorded.

Prior to conducting any ITR tests, the model was adjusted to obtain vertical impingement of all jets. In addition, temperature and pressure surveys of each exhaust plume were made to insure that the impact pressure decay rates were similar to the large-scale tests. During the tests, the variance in exhaust pressure ratio between engine exits was held to within 1.5 percent. The inlet to exhaust total mass flow ratio was held to within ±20 percent.

The data reduction process used during this program was semi-automatic and employed a Decimal Converter System and a high speed digital computer system to compute the internal model flow conditions and the ITR derived from the electrical

8

average circuit for each inlet. The inlet and exhaust flow conditions were calculated using standard isentropic flow relations with the application of appropriate efficiency factors that resulted from calibrations of the various ducts, orifices, and nozzles of the test stand and model.

Since for several samplings, the ITR measured at each thermocouple at randomly selected points in time when averaged were found to compare to within 1 percent of the value obtained from the electrically averaged trace at this same point in time, all ITR data were based on the electrically averaged value. It was assumed that all electrically averaged values agreed to within at least 3 percent of the arithmetic average for all tests during this program. The improvement in accuracy over the 5.2 percent claimed in reference 2 was due to a change made to the electrical circuit which allowed the operator to better match the individual sensitivities of each thermocouple channel.

The ITR at each inlet was determined in the following manner. Each oscillograph record was examined and a time interval selected which was representative of pseudo-steady state temperatures, and during which the test conditions were stable. A typical oscillograph is represented in figure 6 and schematically describes the computation of ITR.

RESULTS AND DISCUSSION

The results presented herein provide information on the effect of exhaust pressure ratio, exhaust gas temperature and surface winds on ITR as well as a discussion of correlating parameters, and finally a comparison between large-scale and small-scale data to assess the effect of geometric model scale on ITR.

Presentation of Results

The basic small-scale data for both model configurations are presented first followed by a presentation of these results in terms of selected correlation parameters. The comparison between large and small-scale data is then presented along with comments on the effect of geometric model scale.

The results are presented in the following figures:

	Figure	
	Side Inlets	Top Inlets
Basic Small Scale Data		
ITR vs $P_{T,j}/P_{bar}$ for various V_∞ , $\psi = 0$	11	17
ITR vs V_∞ for various $P_{T,j}/P_{bar}$, $\psi = 0$	12	18
ITR vs ΔT_j for various $P_{T,j}/P_{bar}$ and V_∞ , $\psi = 0$	13	19
ITR vs $P_{T,j}/P_{bar}$ for various V_∞ and ψ	14	20
ITR vs V_∞ for various $P_{T,j}/P_{bar}$ and ψ	15	21
ITR vs ψ for various $P_{T,j}/P_{bar}$ and V_∞	16	22
Selected Correlation Parameters		
ITR vs V_∞/V_j for various $P_{T,j}/P_{bar}$ and T_j , $\psi = 0$	23	25
ITR vs V_∞/V_j for various V_∞ and ψ	24	26
ITR/ΔT_j vs V_∞ for various $P_{T,j}/P_{bar}$, $\psi = 0$	27	28
ITR/ΔT_j vs $P_{bar} V_\infty/P_{T,j} V_j$ for various $P_{T,j}/P_{bar}$, $\psi = 0$	29	30
ITR vs V_∞ at equal buoyancy conditions	31	31

10

	Figure	
	Side Inlets	Top Inlets

Large and Small Scale Data Comparison

	Side Inlets	Top Inlets
T vs $P_{T,j}/P_{bar}$ (large-scale exhaust conditions)	32	32
ITR vs V_∞ , $\psi = 0$	33	36
ITR vs ψ at various V_∞	34	37
ITR vs V_∞/V_j at various ψ	35	38
$(ITR_{LS} - ITR_{SS})/ITR_{LS}$ vs V_∞ (equal exhaust conditions)	39	39
$ITR/\Delta T_j$ vs buoyancy parameter	40	40
$(ITR_{LS} - ITR_{SS})/ITR_{LS}$ vs V_∞ (equal buoyancy conditions)	41	41

General Considerations

Various phenomenon associated with hot gas ingestion, some of which have also been observed in other investigations (ref. 1 through 16), have been used to interpret results of this study. Of particular interest is the observation (ref. 2, 3 and 4) that the radial and reinforced ground jets are "peeled" by surface winds and blown back toward the model. Reference 2 presents a discussion of the characteristics of the recirculating flow field related to the model configurations used in this present program. The graphic representation of the recirculating flow field from reference 2 is reproduced here in figure 7. At relatively low wind speeds the hot gases are blown back over the top of the model. As the wind speed increases, peeling occurs closer to the model (for fixed exhaust pressure ratio) and the gases can be blown directly into the inlets. At high wind speeds, distortion of the flow field is such that the gases are blown underneath the model resulting in very little or no ingestion. The fact that for a given wind speed, peeling occurs closer to the model as exhaust pressure ratio decreases was verified both by flow visualization (smoke, see figure 8) and measured ITR during this test program. It is noted that the variation of the reinforced ground jet peeling distance (r/D_e) versus ground wind speed presented in figure 8 agrees well with that predicted by the equation $(q_\infty/q_j)^{-\frac{1}{2}} = 2\ r/D_e$, developed from the work of Cox and Abbott in Reference 18.

11

In the interest of providing a basis from which to interpret the absolute values of ITR presented in the data, the reader is advised that ITR is computed to an accuracy of approximately $\pm 5\,^{\circ}F$. Repeatability of results presented in figure 9 verifies this accuracy band and shows that data for zero ground winds is not nearly as repeatable. This inaccuracy of data at zero wind speeds is reflected throughout the data and is probably due to the unstable characteristics of the fountain (ref. 2, 5, and 6) and the turbulent viscous mixing of these fountain gases with an environment which is influenced by small random winds. Data collected during this program indicated that small random winds (less than 5 fps) do not appear to effect ITR at exhaust pressure ratios greater than approximately 1.6, however are influential for pressure ratios less than approximately 1.6. It is noted in passing that the random fluctuation of ingestion by first one inlet and then the other due to fountain instability, as discussed in reference 2, was again observed during the present test series for the zero wind case only. As was noted in reference 2, the technique of averaging the ITR at each inlet provided a means for determining the ITR at $V_\infty = 0$.

To further establish confidence in the absolute value of ITR the generally good agreement between the small-scale data measured during this program with data measured in reference 2 is shown in figure 10. Both sets of data are at $P_{T,j}/P_{bar} = 1.7$, and extrapolation of the reference 2 data have been made where required to form the basis of comparison at constant h/D_e.

<div style="text-align:center">Basic Small-Scale Data</div>

Side inlets configuration, $\psi = 0^{\circ}$. - The variation of ITR with exhaust pressure ratio for various wind speeds and exhaust gas temperatures for the side inlets configuration is shown in figure 11. Here since $\psi = 0^{\circ}$, flow symmetry was assumed and the ITR at inlets 1 and 2 were averaged. ITR is seen generally to increase with increasing pressure ratio for all V_∞. It is also observed that in the limit (not shown), as pressure ratio approaches unity, ITR tends to zero. Further, ITR approaches a maximum level near critical (choked flow) pressure ratios. For supercritical pressure ratios, V_j is constant but additional mass flow (momentum) is supplied to the ground jet, therefore for constant V_∞ peeling occurs even farther from the model resulting in a decrease of ITR. The effect of wind speed is to raise or lower the general level of ITR without significantly altering the characteristic variation of ITR with pressure ratio except for wind speeds near that which yields maximum ITR. At this speed (from 15 to 30 fps) ITR is relatively independent of pressure ratio over the range tested. The increasing decay rate of ITR with decreasing pressure ratio is evidence of the ground jet peeling close to the model and passing back underneath the model away from the inlets. It is noted that the observation at $V_\infty = 0$ made in Appendix E of reference 2, "ITR was independent of inlet and exhaust conditions for this specific configuration only," was, unfortunately, made for a very low ingestion configuration and the present investigation does show a significant effect of exhaust nozzle pressure ratio and temperature on ITR.

12

Cross plots (figure 12) of the figure 11 data show the variation of ITR with headwinds at various pressure ratios and exhaust gas temperatures. The characteristic increase of ITR to a maximum and subsequent decrease with increasing wind speed is observed. Increasing pressure ratio tends to make the slopes (δ ITR/δ V_∞) less steep over the entire wind speed range. In addition, both ITR_{max} and V_∞ at ITR_{max} increase with increasing pressure ratio. These observations may again be understood in light of the dependence of ground jet peeling on pressure ratio and V_∞.

Additional cross plots presented in figure 13 illustrate the variation of ITR with excess exhaust gas temperature for various pressure ratios and wind speeds. ITR varies linearly with ΔT_j, and when the curves were extrapolated linearly to the limit (ITR = 0 at ΔT_j = 0), it was found that ITR = $k\Delta T_j$ where the proportionality constant k is a second order function of pressure ratio and V_∞. The general form of an equation relating ITR, pressure ratio and V_∞ is:

$$ITR = k \left(P_{T,j}/P_{bar}, V_\infty \right) \Delta T_j,$$

where the functional dependence of k on pressure ratio and V_∞ appears to be determinate from available data.

Side inlets configuration, ψ = -45° and -90°. - The variation of ITR with exhaust pressure ratio, V_∞, and ψ for the side inlets configuration at T_j = 1200°F is presented in figures 14, 15, and 16. In general, the ITR measured in the downstream inlet was higher than that measured in the upstream inlet, which agrees with observations made in references 1 and 2. The fact that the downstream inlet ingests the hottest air probably results from a deflection of the forward flowing reinforced ground jet toward the downstream inlet which is located such (h/D_e = 1.2) as to be directly influenced by the high temperature gases in this concentrated ground jet. The general trends of ITR variation with pressure ratio that were observed for the headwind case (see figure 11) are also present for ψ = -45°. (See figure 14a.) Thus the general recirculation flow characteristics of the peeled ground jet discussed earlier is apparently not significantly altered for ψ = -45°. The effect of exhaust pressure ratio on ITR for ψ = -90° (see figure 14b) is considerably different from the ψ = 0 and -45° cases. The recirculating flow field, excluding fountain effects, is assumed to have the same general characteristics as the headwind case. However, interpretation of the ITR trends in figure 14b is complicated by the fact that the inlet faces are aligned parallel to the flow. It seems reasonable to assume that distortion of the flow field by cross flows over the fuselage contributes to these unusual data trends. The variation of ITR with V_∞ and ψ in figures 15 and 16 illustrates that high pressure ratios result in highest ITR over the entire wind speed range tested. Additionally, the upstream inlet is seen to reach a minimum ingestion level at ψ = -45° while the downstream inlet reaches a maximum. (See figure 16.) This indicates that for this wind direction and these inlet locations, the high energy reinforced ground jets are distorted such as to influence the downstream inlet. The fact that ITR at ψ = 0° is approximately equal to the ITR at ψ = 90° for the upstream inlet lends credence to the above assumption that the general recirculating flow characteristics about the model are similar for ψ = 0° and ψ = -90°.

Top inlets configuration, $\psi = 0°$. - The variation of ITR with exhaust pressure ratio for the top inlets configuration at various headwind speeds and exhaust gas temperatures is presented in figure 17. Again the flow symmetry assumption for $\psi = 0°$ is made and the average of the ITR at inlets 1 and 2 and inlets 3 and 4 are shown. The general observations of the variation of ITR with $P_{T,j}/P_{bar}$ made for the side inlets configuration are the same for this configuration, however, as expected, the general level of ITR is much lower. Cross plots (figures 18 and 19) of the data in figure 17 show remarkable similarity to the trends observed for the side inlets with the major difference being that top inlets are less sensitive to variations in exhaust gas temperature. This indicates that the proportionality constant (k) between ITR and ΔT_j is dependent on geometry as well as $P_{T,j}/P_{bar}$ and V_∞. The functional dependence on geometry is of course complex, but for the configurations tested during this program it would include simply h/D_e and inlet location. A preliminary assessment of recirculation path lengths resulting from an analysis of smoke pattern photographs from reference 2, peeling distances measured during this program (figure 8), and unpublished smoke pattern photographs supplied by NASA, Langley, indicates that a recirculation path length could be determined which would correlate the influence of h/D_e and inlet location. Final correlation of recirculation path length with h/D_e and inlet location, and determination of the relationship between ITR and ΔT_j including the effect of pressure ratio and V_∞ could provide the basis for future studies using available data.

Top inlets configuration, $\psi = -45°$ and $-90°$. - The variation of ITR with pressure ratio for each individual inlet of the top inlets configuration is presented in figure 20 for various wind speeds and ψ. It is noted that the trends are not significantly changed with ψ, indicating that for top inlets, the presence of the wing effectively diminishes the strong effect of the recirculating reinforced ground jet. Here, as expected, the upstream inlets experience the highest ITR. Cross plots of the figure 20 data presented in figures 21 and 22 show that minimum ITR occurs at $\psi = -45°$ and maximum ITR at $\psi = -90°$.

Selected Correlation Parameters

To effectively model fluid flow phenomenon at small-scale, the flow system must be geometrically, kinematically and dynamically similar to the full-scale system. For the problem at hand, geometric similarity was maintained for the model, ground plane expanse, model height above the ground plane, and relative wind direction. Although the vertical and horizontal extent of the relative wind stream was not simulated exactly, it was assumed to be adequate because in both the large and small-scale tests the model was totally immersed in the free stream. Kinematic similarity was achieved since both the large and small-scale models were stationary and both tests were conducted over the same range of V_∞. Dynamic similarity demands that the relationship between the inertial, normal, shear and field forces be correctly maintained in the flow system; i.e. dynamic similarity exists at similar points in each system if the ratio of inertia force to viscous force and the ratio of inertia force to gravity force is maintained between the large and small-scale systems (see Reference 19).

14

Complete dynamic similarity cannot, strictly speaking, be achieved in model testing since both force ratios cannot be simultaneously maintained. Generally, in any given flow system one force ratio dominates and the other may be neglected. Historically, hot gas ingestion studies in the U.S. have been conducted for dynamic similarity of inertia forces to viscous forces while work in Europe has emphasized scaling of inertia forces to gravity forces. Both techniques have met with some measure of success. Reference 20 has shown that "results of detailed comparisons of recirculation effects of a full-scale and geometrically similar small-scale VTOL lift engine pod, operating at the same exhaust pressure/temperature conditions, have indicated that the overall near flow-field, external thermal environment, and hot gas ingestion are scalable, in terms of both dynamic and time-average characteristics". On the other hand, W. A. Abbott of the National Gas Turbine Establishment at Pyestock, England in a restricted report dated March 1966, has shown reasonably good comparison of the mean ITR between a small-scale model and the H.S. P1127 aircraft. The model tests were conducted at buoyancy conditions nearly equal to full scale. Full-scale exhaust conditions were not maintained. These two independent results indicate that the correct method for small-scale testing of hot gas ingestion is not yet well defined.

The data collected during the present program provides a basis from which to attempt an empirical determination of a dynamic similarity parameter. A stated objective at the outset of this program was to determine if V_∞/V_j was the desired parameter. When the small-scale ITR data was plotted versus this velocity ratio, (see figures 23, 24, 25 and 26) it was found that; (1) V_∞ appeared as an independent parameter, and (2) V_∞/V_j approached a constant value for fixed V_∞ as the exhaust pressure approached a critical (choked flow) pressure ratio. This indicated that V_∞/V_j was not a correlation parameter and that at best, trends of ITR vs V_∞/V_j have significance only for subcritical pressure ratios. Thus the value of comparing large-scale with small-scale ITR data on the basis of V_∞/V_j is questionable.

A methodology to determine a precise correlation of all the small-scale data would consist of examining nondimensional parameters resulting from dimensional analysis as well as determining the functional relationships between the dependent variable (ITR) and each of the independent variables while holding all other independent variables constant. The dimensional analysis would suggest the form of the parameter while the functional relationships would indicate the relative importance of the independent variables. Thereafter, with an awareness of a crude mathematical model of the flow field along with the aforementioned information, the data would be plotted against selected trial parameters (these selected parameters subsequently modified as required) until correlation is achieved. Although such an effort was beyond the scope of this program, several selected parameters were examined for correlation of the small-scale data.

First of all the validity of normalizing ITR to ΔT_j is verified in figures 27 and 28 for the side and top inlets configurations respectively. These curves indicate that for a constant pressure ratio, the ITR at any of the three exhaust gas temperatures tested, falls within a maximum band of $ITR/\Delta T_j = \pm 0.006$ over the entire velocity range which is consistent with the $\pm 5°F$ accuracy to which ITR is measured.

The normalized ITR was then plotted versus various parameters which included :
(1) free stream to jet dynamic pressure ratio (q_∞/q_j), both compressible and incompressible, (2) free stream to jet Reynolds Number ratio (R_∞/R_j) which accounted for variations in temperature, viscosity and the ratio of specific heats in the exhaust jet and free stream flows, (3) a dimensioned parameter, the ratio of free stream velocity to exhaust momentum flux $(V_\infty/w_j V_j)$, and (4) velocity ratio divided by exhaust pressure ratio $(P_{bar}V_\infty/P_{T,j}V_j)$. When ITR was plotted against each of these parameters, V_∞ and/or exhaust pressure ratio showed as an independent parameter indicating that correlation was not achieved. The best correlation was found using parameters (3) and (4) above. It is seen that these parameters avoid the shortcoming of V_∞/V_j, i.e. tending toward a constant value at critical or supercritical exhaust pressure ratios. To indicate this near correlation, ITR normalized to excess gas temperature is plotted versus $P_{bar}V_\infty/P_{T,j}V_j$ for all V_∞, exhaust pressure ratios, and T_j in figures 29 and 30 for both model configurations. It is noted that the accuracy of data plotted along the ordinate is from ±0.003 to ±0.006, the highest variance associated with $T_j = 900^\circ F$ data, and the lowest with the $1400^\circ F$ data. A crude correlation is seen in figure 27 for $1.4 < P_{T,j}/P_{bar} < 2.0$ which yields results within an accuracy band of $ITR/\Delta T_j = \pm0.007$. The observation that correlation is better at high values of $P_{bar}V_\infty/P_{T,j}V_j$ than at low values for the side inlets (figure 27) and vice versa for the top inlets (figure 28) is probably due to configuration and/or h/D_e effects and should be interpreted as indicating that a correlation band of thickness ±0.007 persists over the whole range of $P_{bar}V_\infty/P_{T,j}V_j$. In light of this near correlation, and since simulation of this parameter can be attained by testing at equal V_j, T_j and V_∞, it appears that large and small-scale data comparisons made at equal exhaust conditions should be valid.

Dimensional analysis yields the parameter, $V_j^2/g\,\beta\,\Delta T_j D_e$ which represents the ratio of jet kinetic energy per unit mass to buoyant forces in a fluid. This is also recognized as the ratio of the jet Reynolds Number squared to Grashof Number. Cox (reference 18) has shown a more suitable parameter for correlating experimental data for a single jet case to be $(V_j^2/g\,\beta\,\Delta T_j D_e)(\theta_a/\theta_j)^{\frac{1}{2}}$. This says that model data should be compared with full-scale data at equal values of this buoyancy parameter, rather than at equal exhaust velocity and temperature. It seems reasonable to assume that if ITR were plotted versus this buoyancy parameter for various surface wind speeds, wind speed would show up as an independent parameter in the plot. This was found to be so for the data collected during this program over a buoyancy parameter range of from 40,000 to 120,000. Additional tests were conducted to extend this range down to 16,000 for the top inlets case since the large-scale data were measured over a range of this buoyancy parameter from 14,000 to 22,000. Summary curves of $ITR/\Delta T_j$ versus the buoyancy parameter at various V_∞ are shown in figure 31 for both model configurations. These curves represent median values obtained from data plots presented in the appendix.

Large and Small Scale Data Comparison

Comparison of large and small-scale ITR data based on equal full-scale exhaust conditions can be made by simply interpolating the small-scale data at exhaust conditions equal to the full-scale. The exhaust conditions range of the small-scale data, however, is such that it lends itself to further analysis which permits an additional data comparison based on equal buoyancy conditions. Comparisons made by these two methods are presented in the following.

Prior to making these comparisons, the published large-scale exhaust pressure data was examined for consistency. Since the large-scale model was powered by a turbojet engine (GE-YJ85-7), the exhaust pressure ratio will vary with inlet temperature in a manner characteristic of jet engines. The measured exhaust pressure ratio is plotted versus inlet temperature for both model configurations in figure 32. These data were faired to be consistent with the characteristics of the J-85-13 engine described in reference 21 which are also shown in figure 32. These faired curves (solid lines) were then used to prescribe the exhaust conditions at which the large-scale ITR data were measured.

It is also noted that since crosswinds were directed from the right side of the small-scale model and from the left side of the large-scale model, ITR data at inlets 2 and 4 of the large-scale model were compared with ITR data at inlets 1 and 3 respectively of the small-scale model.

Equal V_j and T_j Comparison. - The large and small-scale data is compared at equal exhaust conditions (V_j, T_j) in figures 33 through 38. The comparison is poor. This is further exemplified in figure 39 where the percentage difference between the large-scale and small-scale data is summarized for both configurations over the range of headwind speeds tested.

Equal buoyancy conditions. - The curves in figure 31 were used to determine small-scale ITR at the same V_∞ and buoyancy parameter as the large-scale data. The required extrapolation was aided by the known end point that ITR = 0 when the buoyancy parameter = 0, and the additional test data measured for the top inlets configuration. A comparison of large and small-scale ITR at equal buoyancy parameter values is presented in figure 40 over the range of V_∞ tested for both model configurations. Although the general large-scale trends of ITR vs V_∞ are reflected in the small-scale date, figure 41 indicates that the difference between the large and small-scale data is not consistent over the speed range, thus the comparison must be considered poor.

ITR Scale Factor

An important objective of reference 2 and the current program was to determine if a scale factor could be applied to the small-scale ITR data to reliably predict large-scale results. No consistent scale factor was apparent for the comparison methods attempted.

17

Possible explanations for the poor comparisons between the large and small-scale data include: (1) full-scale exhaust and free stream conditions should not be duplicated in model testing, (2) the effect of buoyant forces must be included to obtain dynamic similarity in the flow field, (3) the assumption implicit in maintaining equal exhaust conditions, that the recirculating path length varies as the linear scale factor is not valid, and (4) large to small-scale similarity in instrumentation, test techniques, operating conditions, and data reduction, were not maintained. The first two explanations are indicated by the data and infer the existence of an as yet unknown dynamic similarity parameter for use in hot gas ingestion studies. The third was examined in a preliminary manner as alluded to earlier using available data (reference 2, figure 8, and unpublished NASA smoke pattern photographs). It was found that the ratio of the large-scale to small-scale reinforced ground jet penetration distance into the free stream (normalized to equal V_j) varied from 2.7 at headwinds of 20 fps to 2.0 at 60 fps. This indicates that the recirculation path length not only does not scale as the linear scale factor (4 in this case), but also the relative lengths between model and large-scale varies with wind speed. Further experimental study of this observation is needed. The fourth explanation is qualitatively evaluated in the following.

Instrumentation: The inlet thermocouples were located at similar positions in both the large and small-scale models and temperature time histories were obtained on oscillograph for all channels. The large-scale tests employed specially constructed 36 gage chromel-alumel thermocouple probes while the small-scale tests used 30 gage bare bead iron-constantan. The differing response rates of these probes was of no consequence (see reference 1) since in both cases data was collected over a relatively long (approximately 12 seconds) time span and temperature data points were selected from the time histories only after steady state conditions had been reached.

Test Techniques: The major difference in test techniques was that the large-scale tests were conducted in a wind tunnel and the small-scale tests were conducted in an outdoor facility which featured a large free jet as a wind source. The effect of differences in the quality of the free stream air flow is not known.

Operating Conditions: Several apparently small differences existed. (1) The small-scale tests were subject to small (less than 5 fps) random winds. These random winds were measured and vectorially accounted for when defining V_∞. (2) The large-scale tests tended to heat the tunnel, however because of the short duration of each test and the large volume of the wind tunnel the ambient temperature rise was estimated to be no more than $2°F$. (3) The large-scale exhaust conditions were not absolutely controllable and varied with hot gas ingestion. Nominal values for exhaust pressure ratio (based on a constant barometric pressure of 14.7 psi) and exhaust gas temperature were used. The small-scale exhaust conditions were controlled and accurately measured. An attempt to account for these differences was made as shown in figure 32. (4) The boundary layer thickness along the ground plane was not measured for either test series. It was assumed that geometric scaling of the ground planes would result in scaled boundary layer thicknesses.

18

Data reduction: The large-scale ITR was calculated by manually determining the average steady state temperature of each probe from oscillograph records and then computing the arithmetic average of all thermocouples in each inlet. The ambient temperature at the time of nozzle deflection was subtracted from this result to yield ITR. The small-scale ITR was calculated as shown in figure 6. Since the basic concept of the data reduction methods were similar, the ITR accuracies are assumed compatable.

CONCLUDING REMARKS

Data from small-scale hot gas ingestion studies conducted at the Bell Aerospace Company's Jet Impingement Test Facility along with comparisons with large-scale NASA data have indicated the following conclusions:

1.   ITR is proportional to exhaust gas temperature minus ambient temperature, and the constant of proportionality is a function of exit pressure ratio and relative wind speed.

2.   Small random winds (less than 5 fps) do not appear to effect ITR at exhaust pressure ratios greater than approximately 1.6, however are influential for pressure ratios less than approximately 1.6.

3.   The ratio of surface wind velocity to jet exit velocity does not appear to be a valid normalizing parameter for hot gas ingestion data.

4.   No ITR scale factor was apparent for the similarity parameters examined in this report. The negative result may be due to small differences between the large and small scale test techniques and operating conditions.

5.   A more comprehensive evaluation of potential dynamic similarity parameters is required to determine that parameter which best correlates the large and small-scale data.

REFERENCES

1. McLemore, H. Clyde; Smith, Charles C. Jr.; and Hemeter, Patricia G.:
    Generalized Hot-Gas Ingestion Investigation of Large-Scale Jet VTOL Fighter-
    Type Models. NASA TN D-5581, 1969

2. Ryan, Patrick E.; and Cosgrove, Wayne J.: Empirically Determined Wind and
    Scale Effects On Hot Gas Recirculation Characteristics of Jet V/STOL Aircraft.
    NASA CR-1445, October 1969.

3. McLemore, H. Clyde; and Smith, Charles C., Jr.: Hot Gas Ingestion Investi-
    gation of Large-Scale Jet VTOL Fighter-Type Models , NASA TN D-4609,
    June 1968.

4. Tolhurst, William H., Jr.; and Kelly, Mark W.: Characteristics of Two Large-
    Scale Jet-Lift Propulsion Systems. Conference on V/STOL and STOL Aircraft,
    NASA SP-116, 1966, pp. 205-228.

5. Hall, Gordon R.: Recirculation and Ingestion Characteristics of a Large-Scale
    VTOL Lift Engine Pod. Northrop Norair, NASA CR-72410, August 1968.

6. Hall, Gordon R. and Rogers, Kenneth H.: Recirculation Effects Produced by a
    pair of Heated Jets Impinging on a Ground Plane. NASA CR-1307, 1969.

7. Cox, M.; and Abbott, W.: Studies of the Flow Fields Created by Single
    Vertical Jets Directed Downwards Upon a Horizontal Surface . National Gas
    Turbine Establishment, Memo No. 390, October 1964.

8. Speth, Robert F.; and Ryan, Patrick E.: A Generalized Experimental Study
    of Inlet Temperature Rise of Jet V/STOL Aircraft in Ground Effect. Bell
    Aerosystems Co. Report 2099-928003 (Contract No. N600(19)63320, April 1966.
    Available from DDC as AD641610.

9. Ryan, Patrick E.; Heim, Richard J.; and Cosgrove, Wayne J.: A Generalized
    Experimental Investigation of Hot Gas Recirculation and Ingestion for Jet VTOL
    Aircraft , Bell Aerosystems Co., NASA CR-1147, September 1968.

10. Langfelder, Bodeneffekte bei Senkrechtstart-Flugzeugen: (Ground Effects of
    VTOL Aircraft). EWR-Nr. 37/62, Entwick lungsring Sud (Munchen), March
    1963.

11. Harris, A. E.; Marbert, J. A.; and Tatom, J. W.: VTOL Transport Exhaust Gas Ingestion Model Tests. Paper 67 - ENV-17, Seventh Annual National Conference on Environmental Effects on Aircraft & Propulsion Systems, September 1967, Princeton, New Jersey.

12. Lavi, Rahim: Parametric Investigation of VTOL Hot Gas Ingestion and Induced Jet Effects in Ground Proximity. Report NOR 67-32 (Contract NOw 66-0316-f), Northrop Corp., February 1967. Available from DDC as AD 809224.

13. Kemp, E. D. G.: Studies of Exhaust Gas Recirculation for VTOL Aircraft. AIAA Paper No. 67-439, July 1967.

14. Kirk, Jerry V.; and Barrack, Jerry P.: Reingestion Characteristics and Inlet Flow Distortion of V/STOL Lift Engine Fighter Configurations. AIAA Paper No. 68-78, Jan. 1968.

15. Abbott, W. A.: Studies of Flow Fields Created by Vertical and Inclined Jets When Stationary or Moving Over a Horizontal Surface. C.P. No. 911, Brit. A.R.C., 1967.

16. Lavi, Rahim; Hall, Gordon R.; and Stark, Wilbur W.: Full-Scale Ground Proximity Investigation of a VTOL Fighter Model Aircraft. NASA CR-1098, 1968.

17. Skifstad, J. G.: Aerodynamics of Jets Pertinent to VTOL Aircraft, AFAPL-TR-69-28, March 1969.

18. Cox, M.; and Abbott, W.: Jet Recirculation Effects In V/STOL Aircraft. F. Sound Vib., 1965.

19. Knudsen, James G.; and Katz, Donald L.: Fluid Dynamics and Heat Transfer, McGraw-Hill, New York, 1958, p 130.

20. Hall, Gordon R.: Scaling of VTOL Recirculation Effects. Northrop Corp, Proposed low-number NASA CR Resulting from NASA Contract NAS3-10498, 1970.

21. General Electric Company; Model Specification E1075 (Engine, Aircraft, Turbojet J85-GE-13), June 1963.

Table I. – Test Summary

Configuration	T_j °F	ψ (Deg)	V_∞ (fps)	Exit Pressure Ratio $P_{T,j}/P_{bar}$	Number of Tests
Side Inlets at h/D_e = 1.2 S/S_j = 43	900	0	0, 15, 25, 40, 50	1.4, 1.6, 1.8, 2.0	35
	1200	0	0, 15, 25, 40, 50	1.3, 1.4, 1.5, 1.6, 1.7, 1.8, 1.9, 2.0	61
	1200	-45	15, 25	1.3, 1.4, 1.5, 1.6, 1.7, 1.8, 1.9, 2.0	21
	1200	-90	15, 25	1.3, 1.4, 1.5, 1.6, 1.7, 1.8, 1.9, 2.0	18
	1400	0	0, 15, 25, 40, 50	1.4, 1.6, 1.8, 2.0	24
Top Inlets at h/D_e = 3.0 S/S_j = 43	900	0	0,7,15,25,40,50	1.1, 1.3, 1.4, 1.6, 1.8, 2.0	28
	1200	0	0,7,15,25,40,50	1.1, 1.3, 1.4, 1.5, 1.6, 1.7,1.8,1.9,2.0	60
	1200	0	7,20,30,40,50	1.1, 1.8	11
	1200	-45	15, 25	1.3, 1.4, 1.5, 1.6, 1.7, 1.8, 1.9, 2.0	16
	1200	-90	15, 25	1.3, 1.4, 1.5, 1.6, 1.7, 1.8, 1.9, 2.0	21
	1400	0	0,7,15,25,40,50	1.1, 1.3, 1.4, 1.6, 1.8, 2.0	25
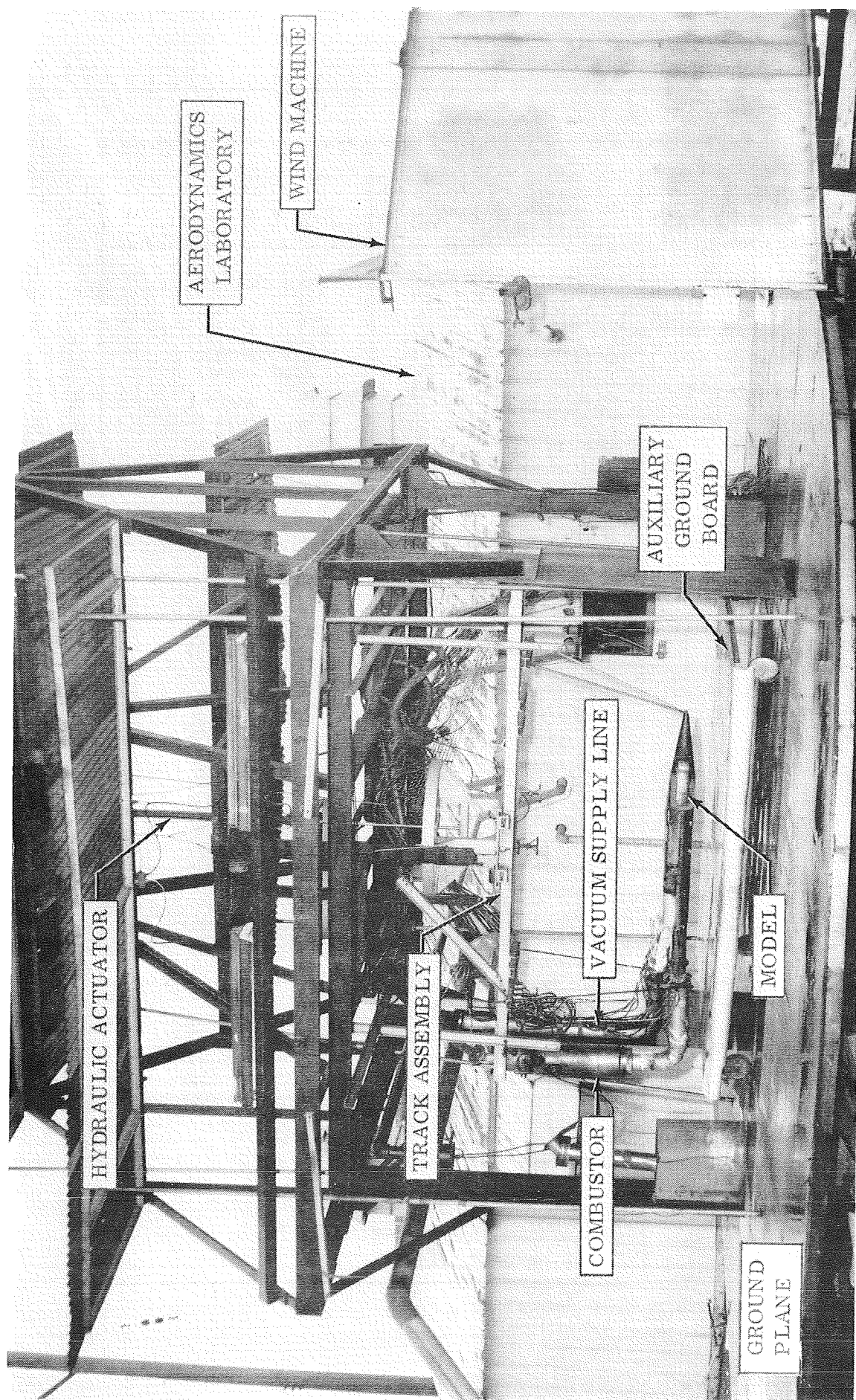
Figure 1. – Jet Impingement Test Facility
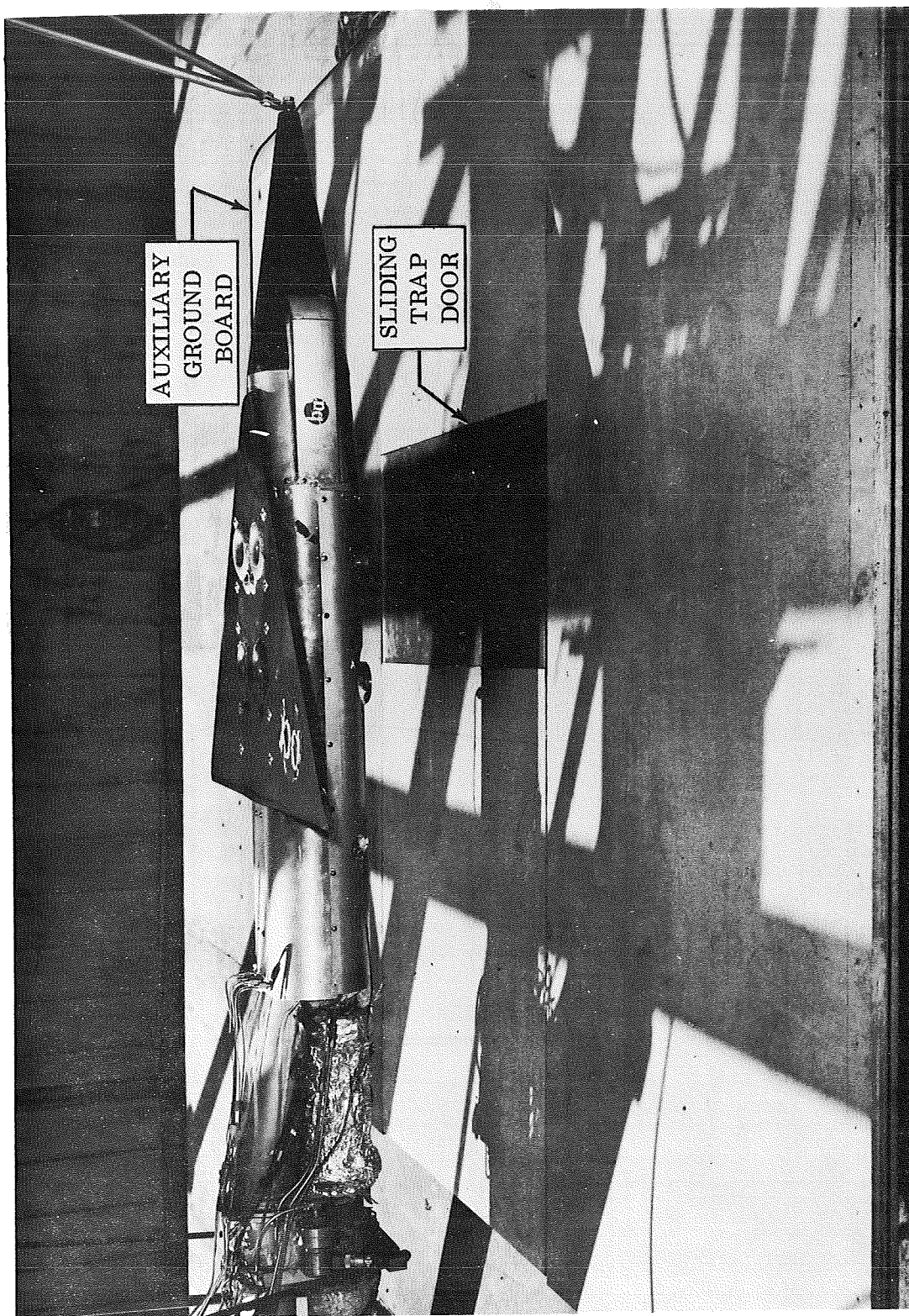
Figure 2. – Top Inlets Configuration, 0.24 Scale Model
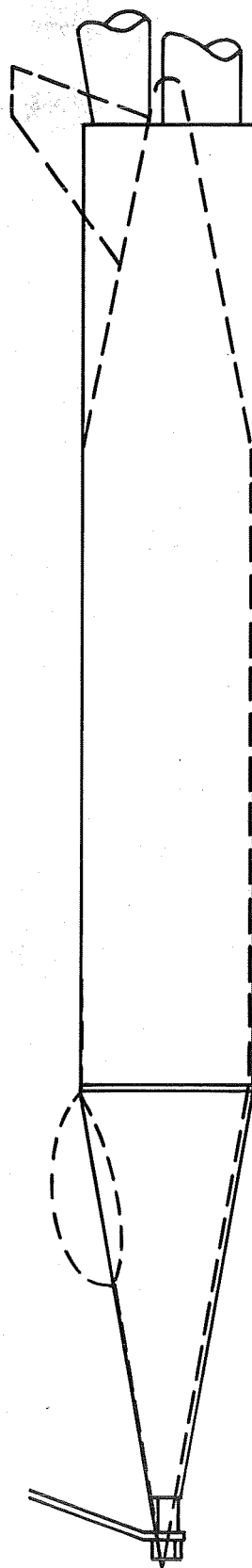
SMALL SCALE MODEL, 4 TIMES SIZE

LARGE SCALE MODEL

Figure 3. – Geometric Similarity Of Model

VIEW LOOKING AFT INTO LEFT INLET
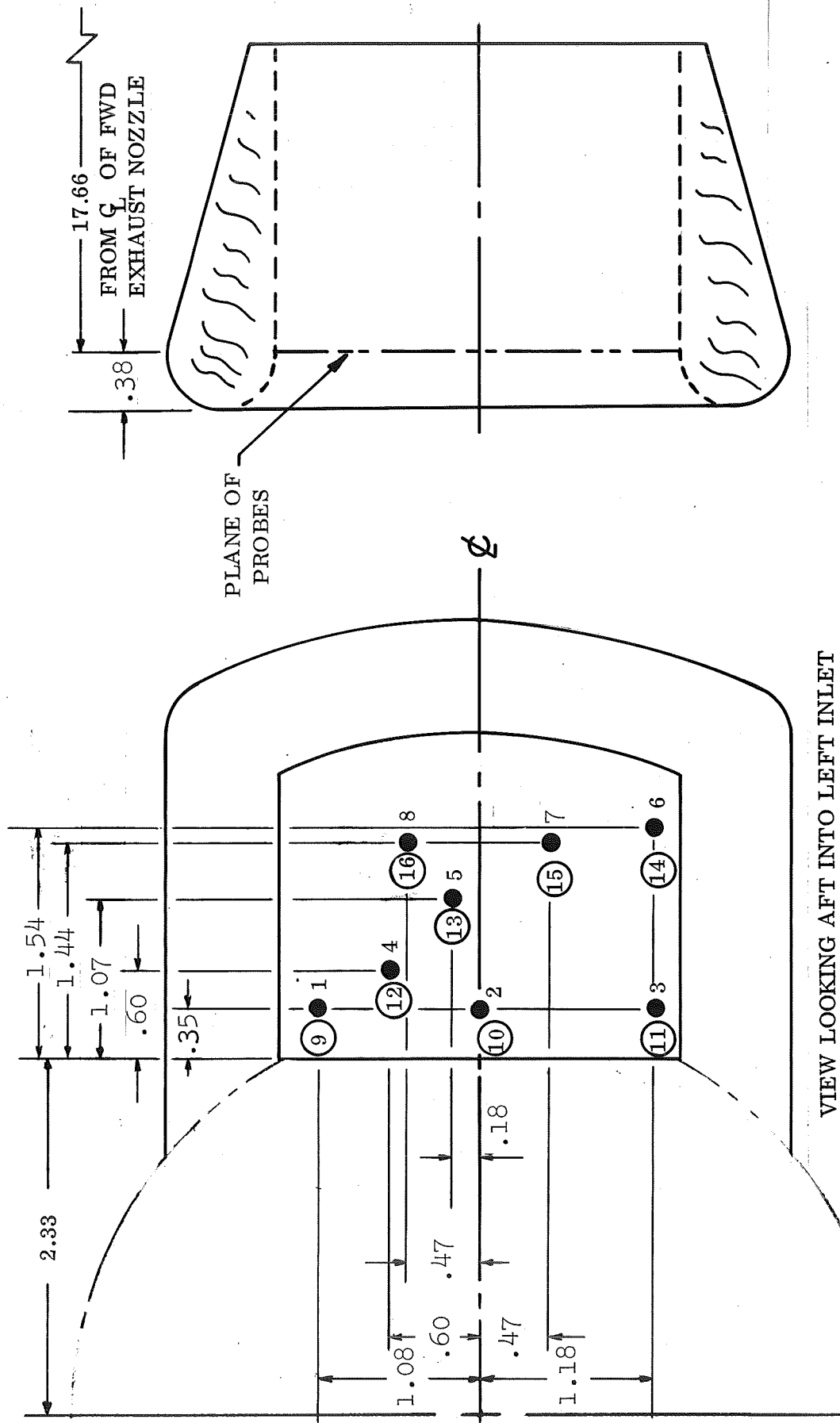
NOTES: (1) Thermocouple Identification Numbers Indicate Inlet 1 (Uncircled)
And Inlet 2 (Circled).

(2) All Dimensions In Inches.

Figure 4. - Location Of Inlet Thermocouples

(a) Side Inlets Configuration

27

INLET NO. 1

INLET NO. 2

INLET NO. 4

INLET NO. 3

4.65 IN.

8.55 IN.

$-\psi$ V_∞

$S/S_j = 43$

● - THERMOCOUPLE LOCATION

FORWARD

INLET DETAIL, TYPICAL

0.79 IN.
RADIUS

0.96 IN.
RADIUS

0.24 IN.
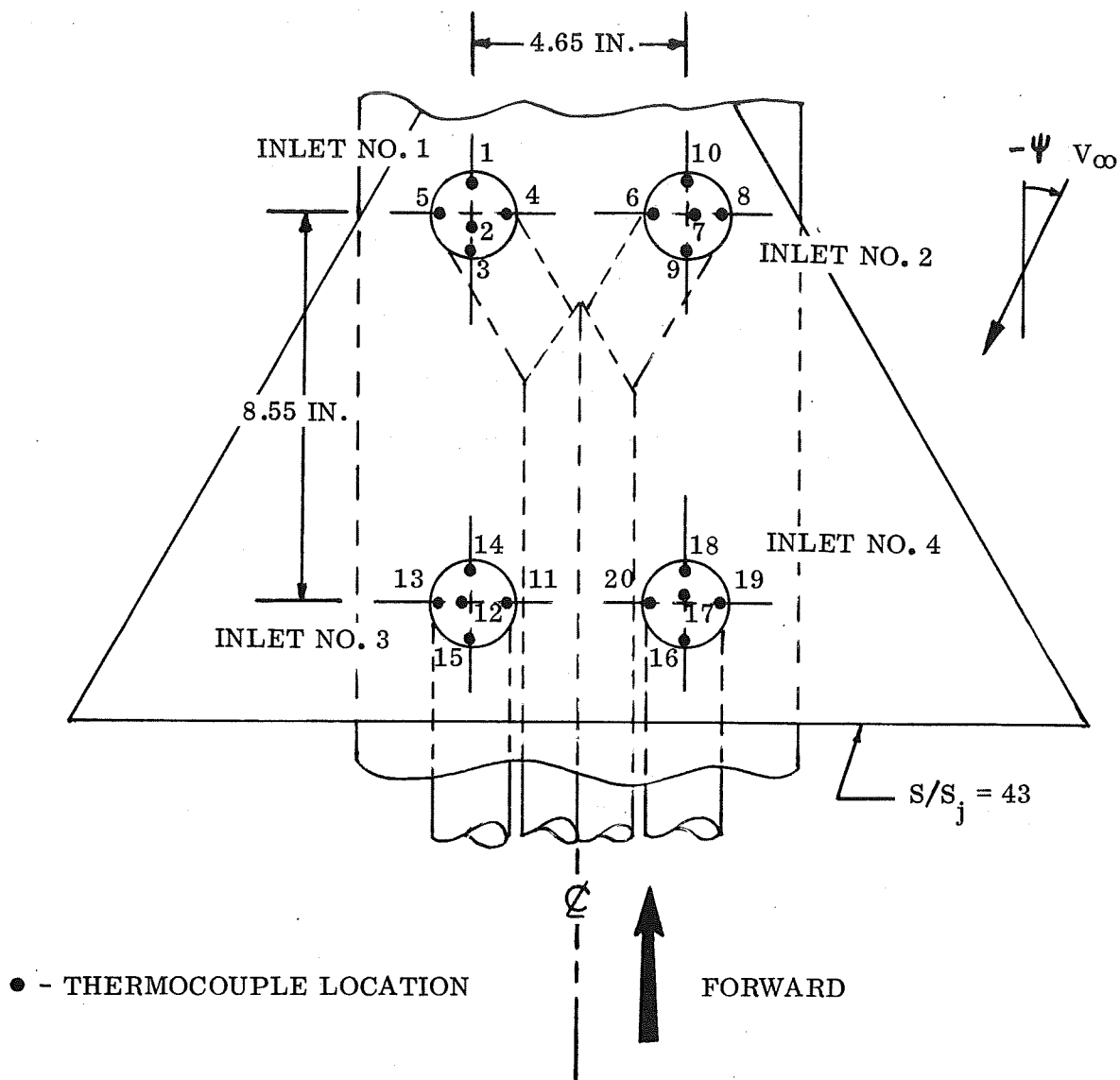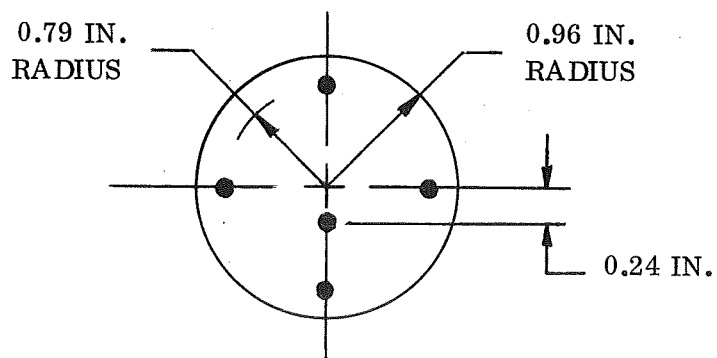
(b) Top Inlets Configuration

Figure 4. - Concluded.

INLET NO. 2

TOP VIEW OF INLET SYSTEM

INLET NO. 1

32 IN.

TRANSITION SECTIONS

FLANGED ATTACHMENT TO TEST FACILITY

13 IN.

⊗ TOTAL TEMPERATURE; TOTAL AND STATIC PRESSURE

○ TOTAL AND STATIC PRESSURE

63 IN.

8.55 IN.

4.65 IN.

3

4

1

2

BOTTOM VIEW OF EXHAUST SYSTEM

(a) Side Inlets Configuration
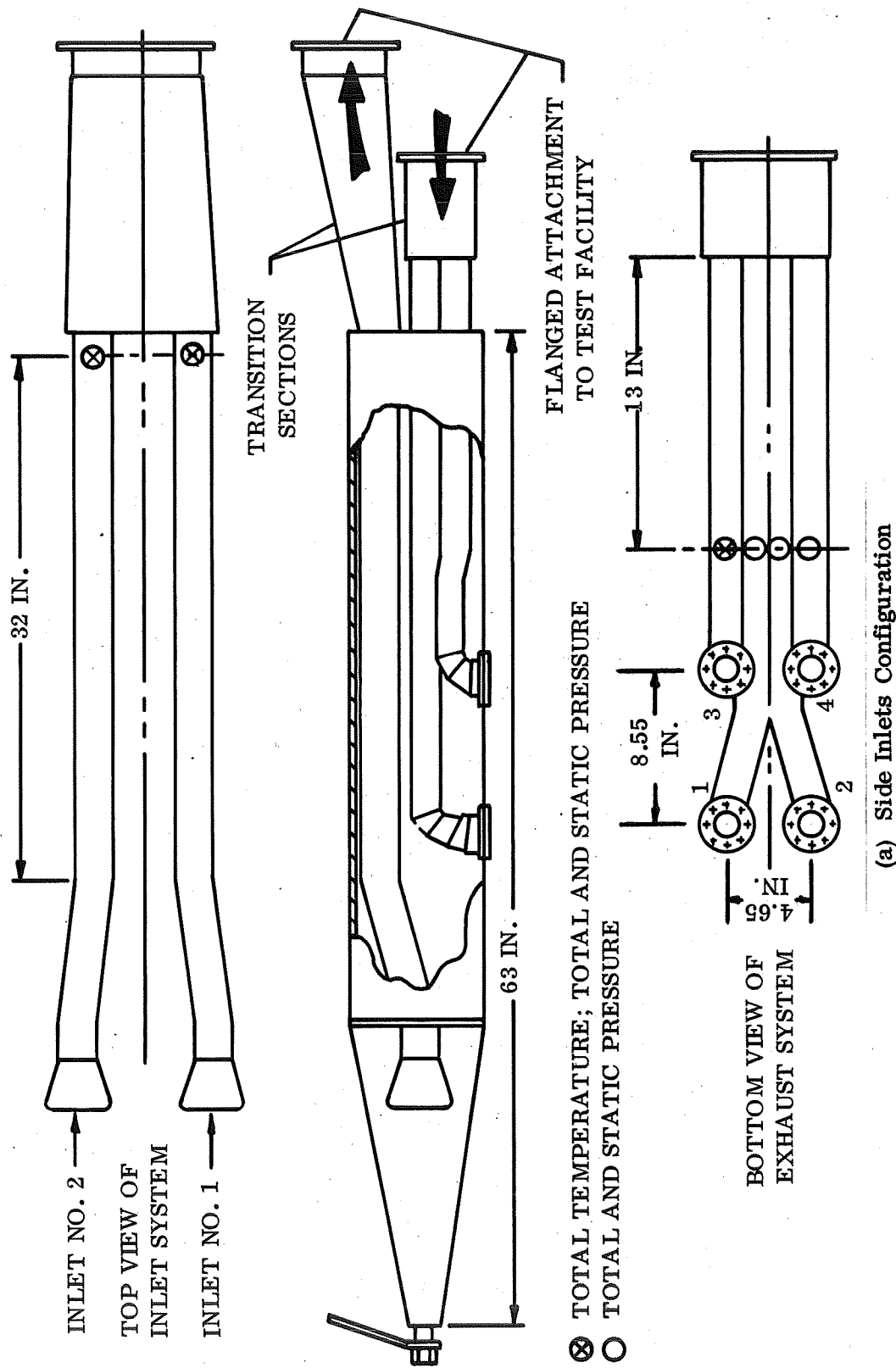
Figure 5. – Model Internal Flow Instrumentation

29

TOP VIEW OF INLET SYSTEM

21 IN.

TRANSITION SECTIONS

FLANGED ATTACHMENT TO TEST FACILITY

63 IN.

13 IN.

8.55 IN.

4.65 IN.

BOTTOM VIEW OF EXHAUST SYSTEM

⊗ TOTAL TEMPERATURE; TOTAL AND STATIC PRESSURE
○ TOTAL AND STATIC PRESSURE
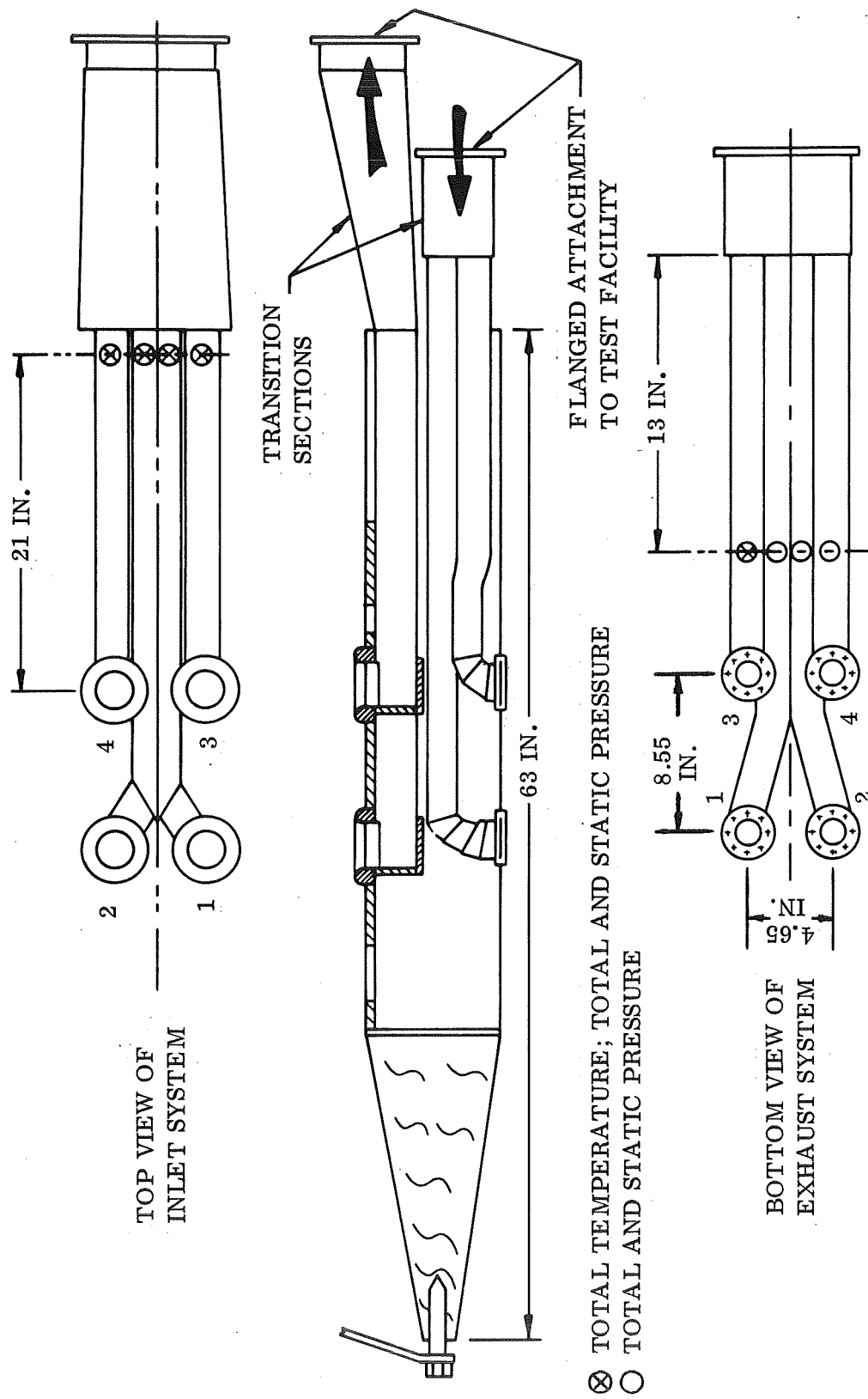
(b) Top Inlets Configuration

Figure 5. – Concluded.

TIME INTERVAL OF INTEREST

ACHIEVED
STEADY STATE

APPROX
1 TO 6
SECONDS

TIME = 0

GALVONOMETER ZERO
(REFERENCE LEVEL FOR
DECIMAL CONVERTER)

TEST START

TEMP = T_{ref}

CALIBRATE
SIGNAL

$T_{input} = 300°F$

x

c
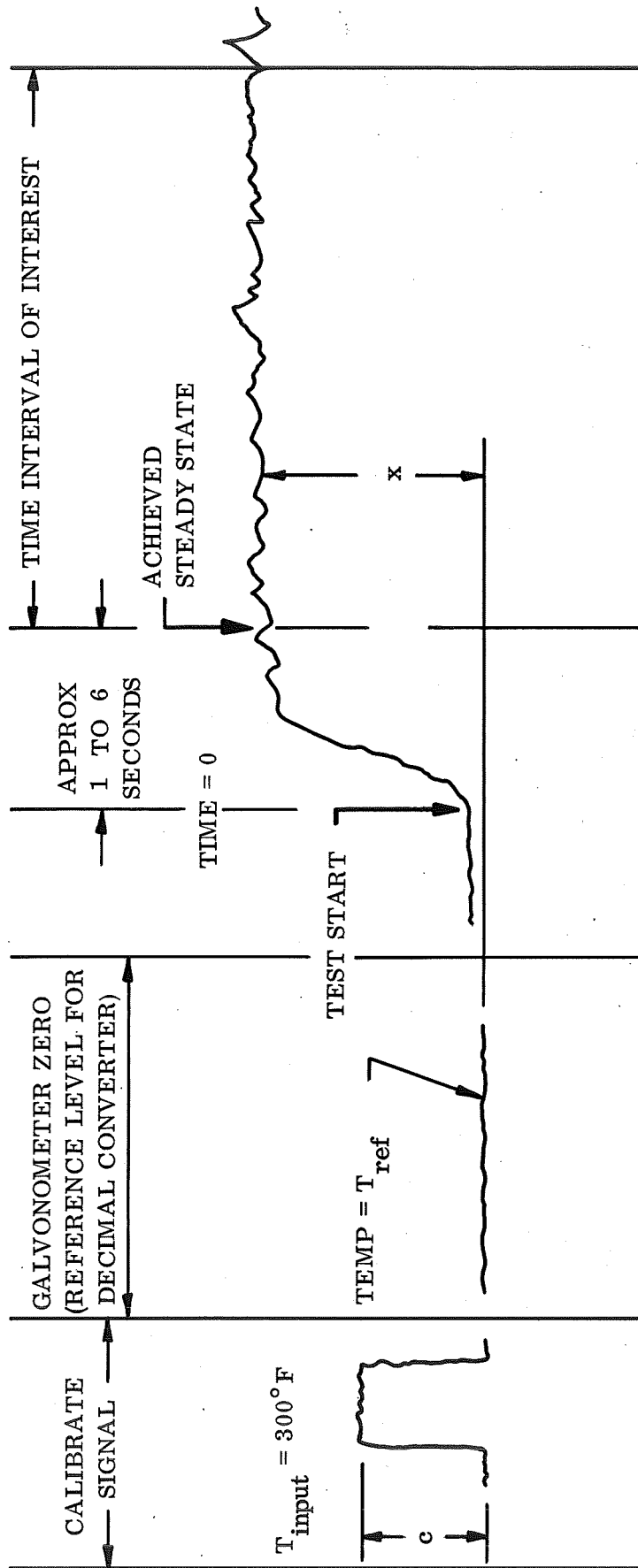
$$\text{ITR} = K \; \frac{1}{n} \left[\left\{ \sum_1^n x \right\} \frac{300}{c} + T_{ref} - T_{amb} \right]$$

WHERE: K = CONVERSION FROM DECIMAL CONVERTER COUNTS TO INCHES, IN/COUNT

n = NUMBER OF DATA POINTS DURING THE TIME INTERVAL OF INTEREST

x = DECIMAL CONVERTER COUNTS

c = CALIBRATION SIGNAL IN INCHES

Figure 6. – Definition Of ITR

31

PEELING LINE

(a) PEELING POINT EDDY
(b) EDDY TRAPPED UNDER WING
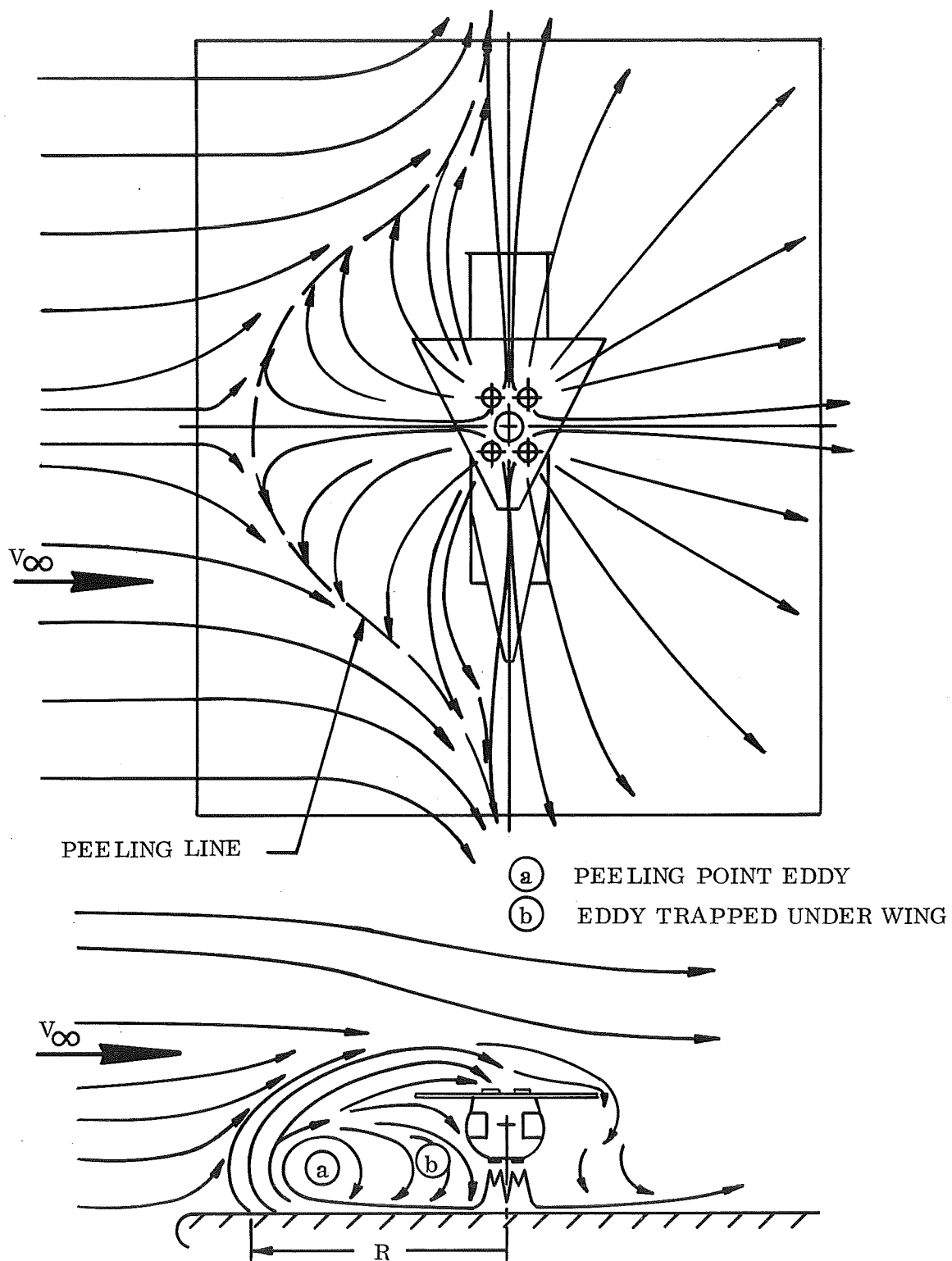
Figure 7. - Effect Of Wind On Recirculation
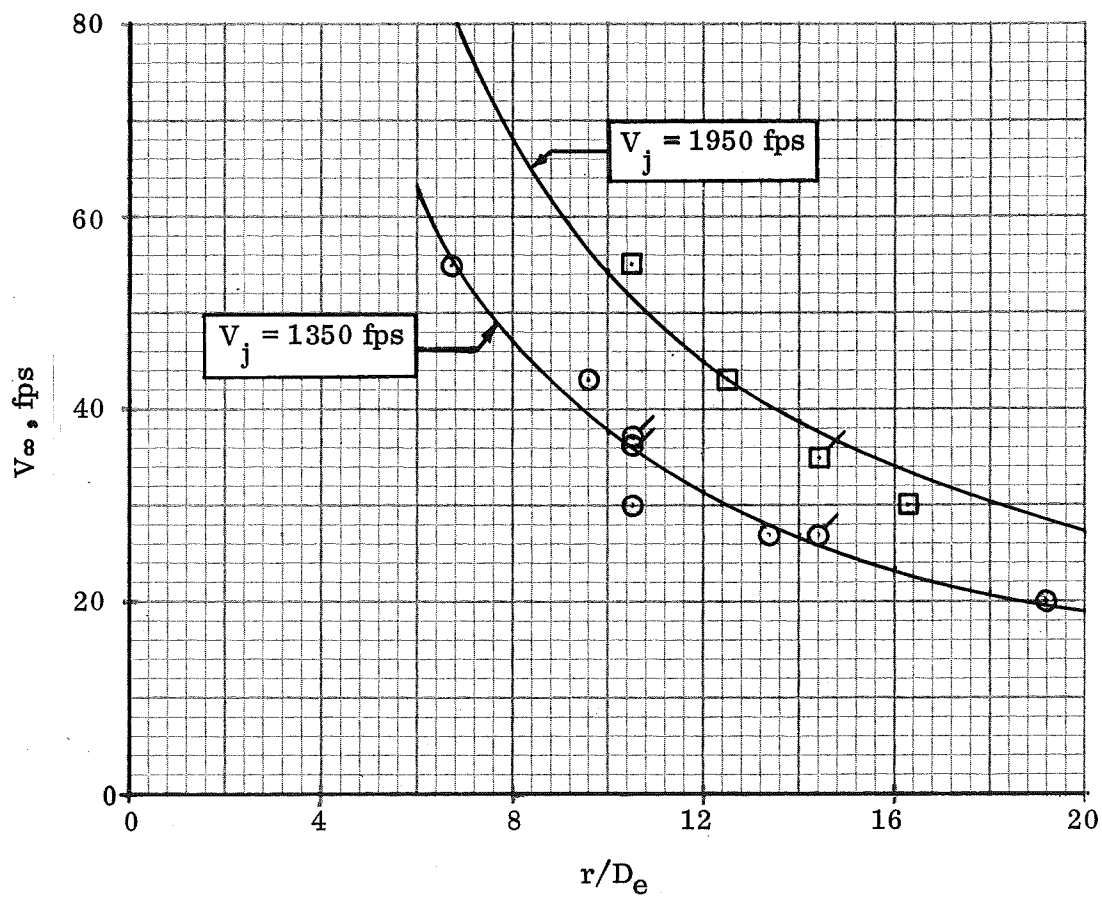
Figure 8. – Reinforced Ground Jet Peeling, $T_j = 1200°F$

SYM	Inlet
○	1
□	2
◇	3
△	4
◁	Av 1 & 2
◺	Av 3 & 4

Shaded $= V_\infty = 0$
Flagged $=$ Top Inlets, $h/D_e = 3.0$
Unflagged $=$ Side Inlets, $h/D_e = 1.2$

Accuracy
$\pm 5°$F

First Test ITR $-°$F Above Ambient

Repeat Test ITR $-°$F Above Ambient
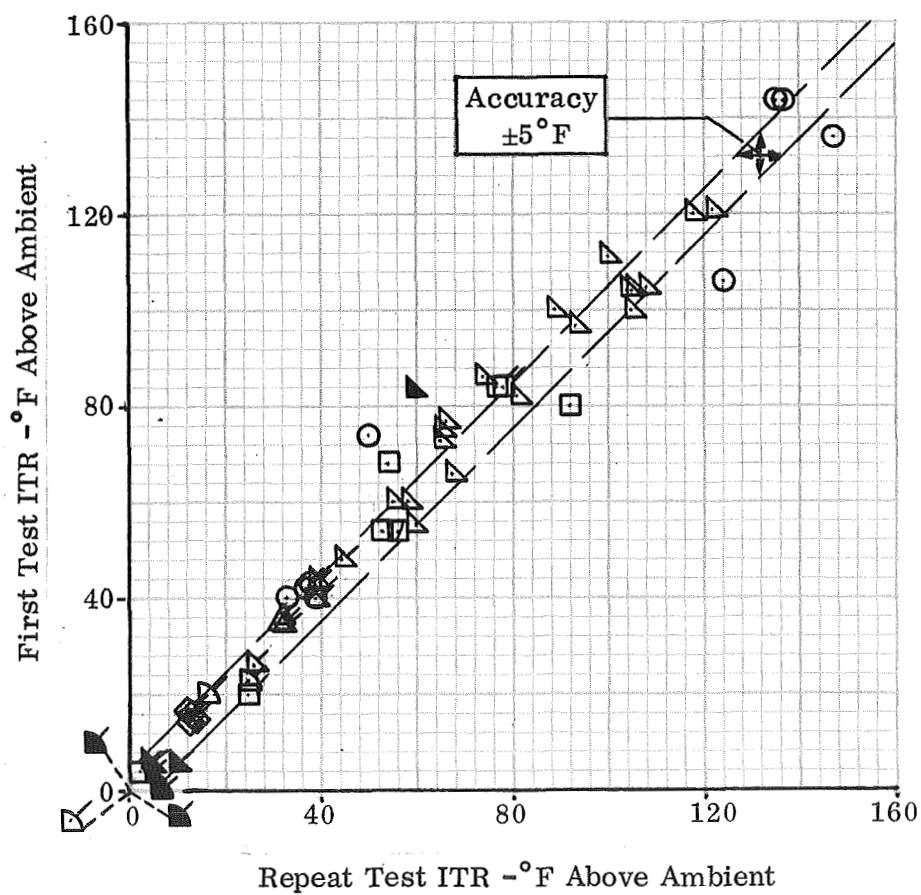
Figure 9. – Repeatability of ITR Measurements

34
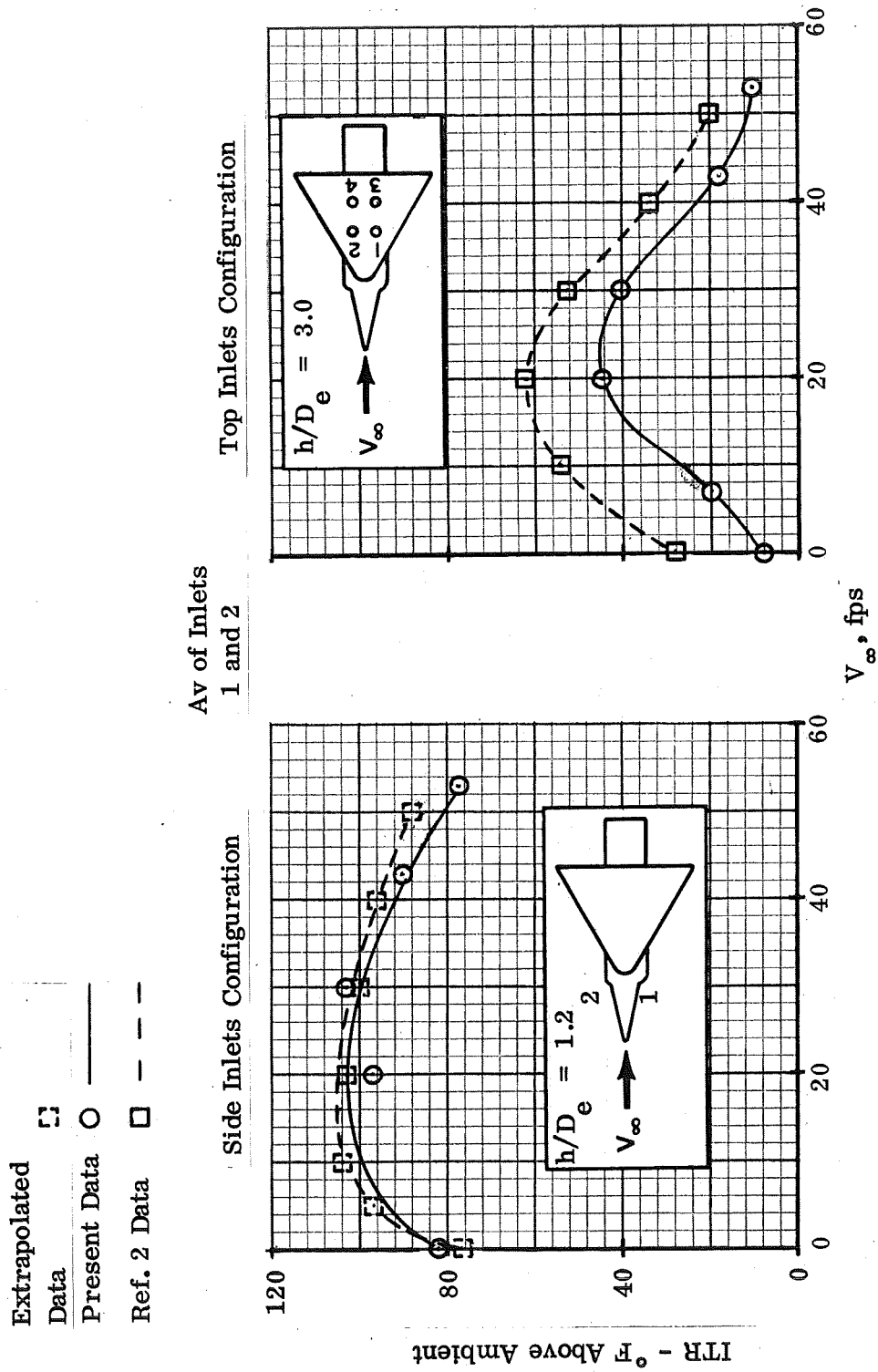
Figure 10. – Comparison of Present and Previous Data, $T_j = 1200°F$, $\psi = 0°$, $P_{T,j}/P_{bar} = 1.7$
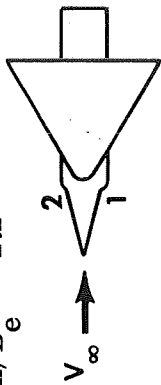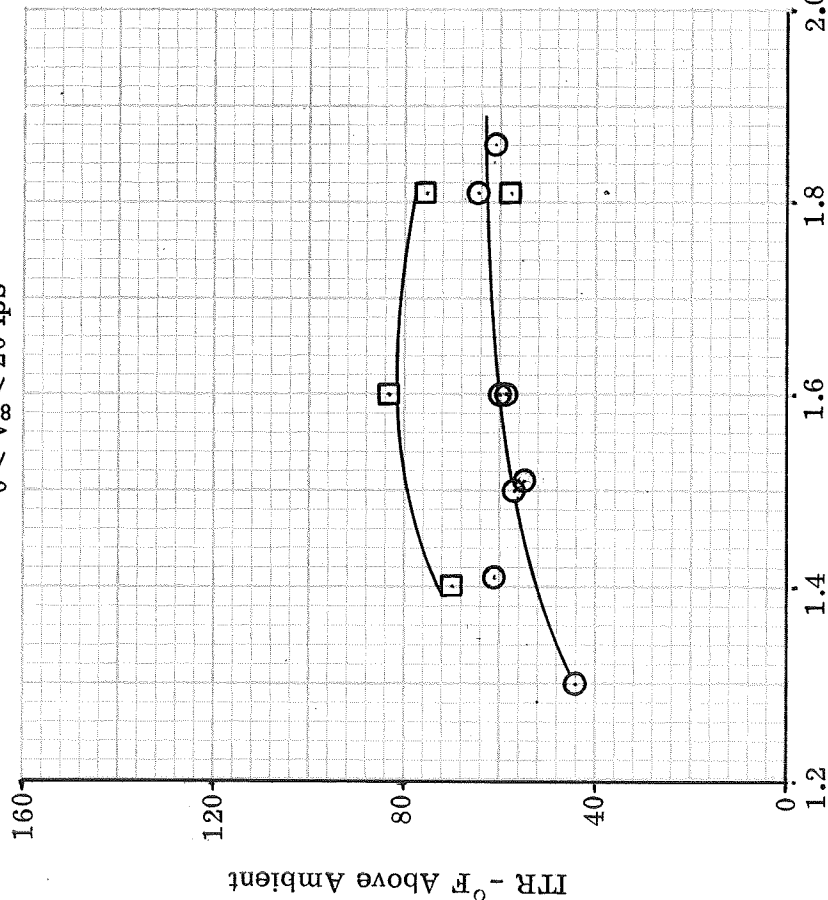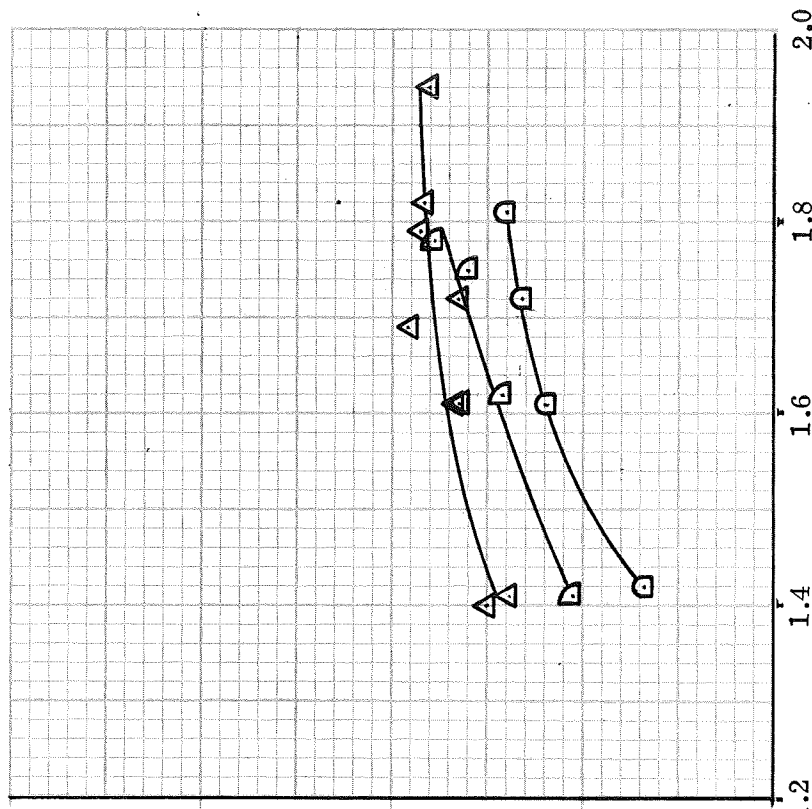
Figure 11. – Variation of ITR With Exhaust Pressure Ratio for Various Wind Speeds, Side Inlets Configuration, $\psi = 0$
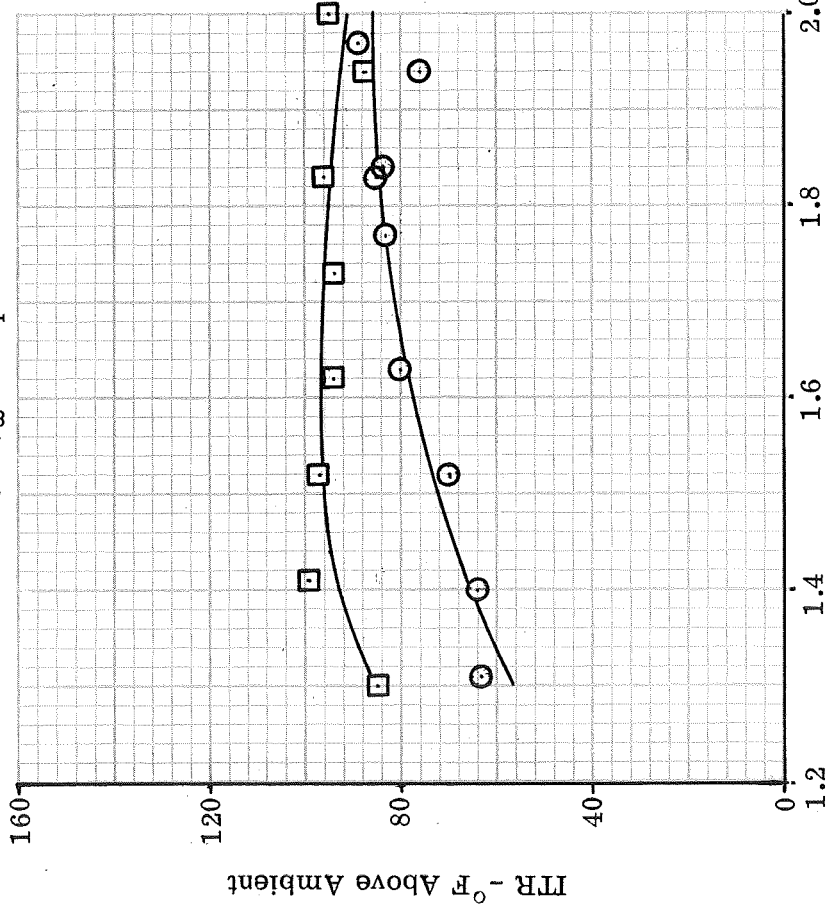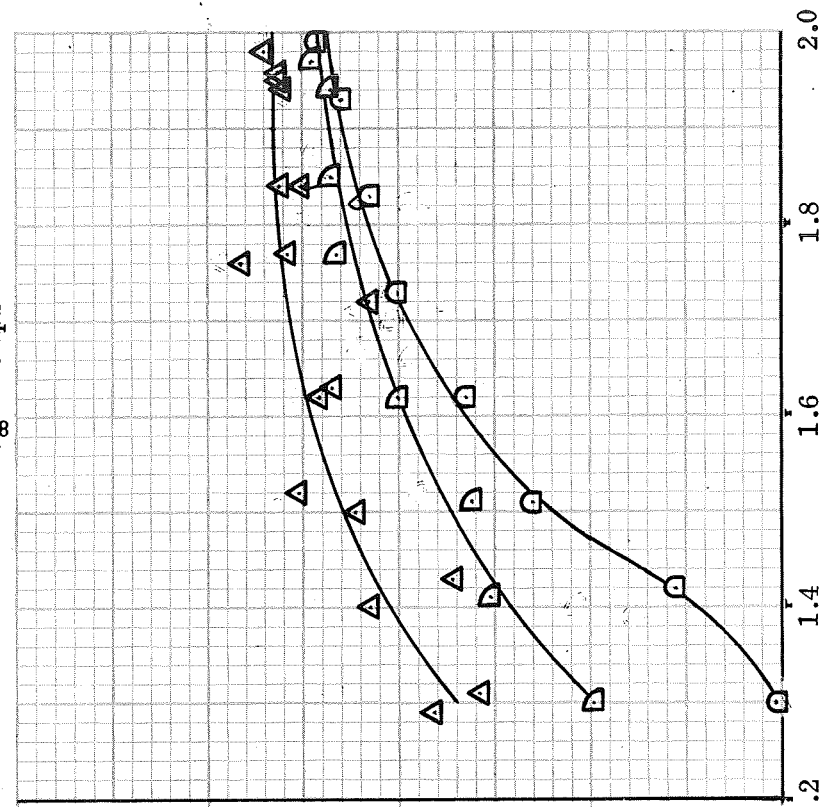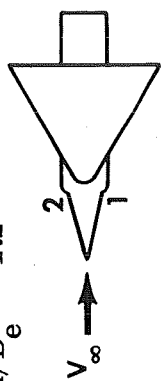
(a) Average of Inlets 1 and 2, $T_j = 900°F$

(b) Average of Inlets 1 and 2, $T_j = 1200°F$

Figure 11. – Continued.

37

$30 < V_\infty < 53$ fps

$0 < V_\infty < 20$ fps

$h/D_e = 1.2$

SYM	V_∞, fps
○	0
□	20
△	30
◁	43
◖	53

Exhaust Pressure Ratio, $P_{T,j}/P_{bar}$

ITR – °F Above Ambient
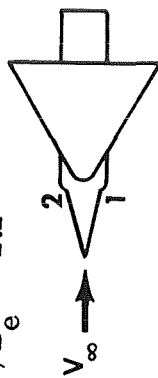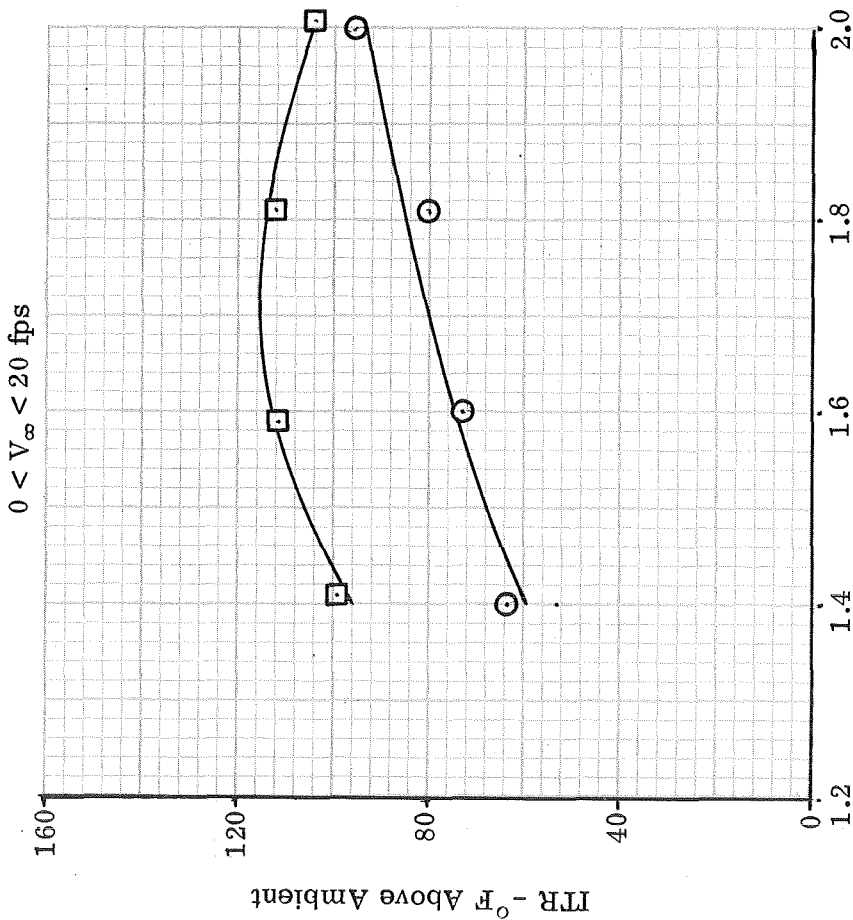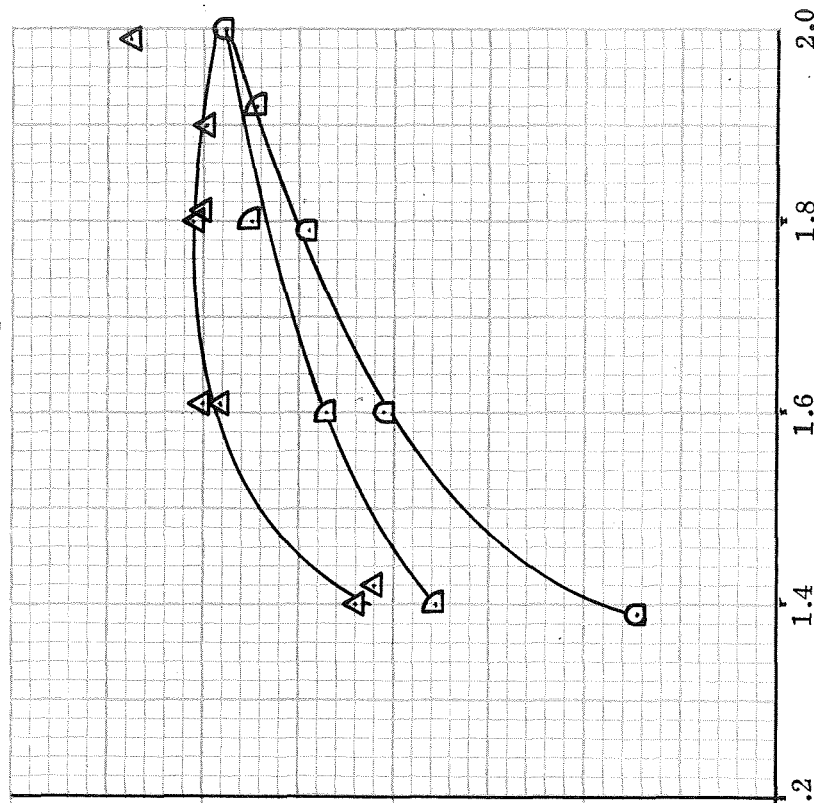
(c) Average of Inlets 1 and 2, $T_j = 1400°$F

Figure 11. – Concluded.
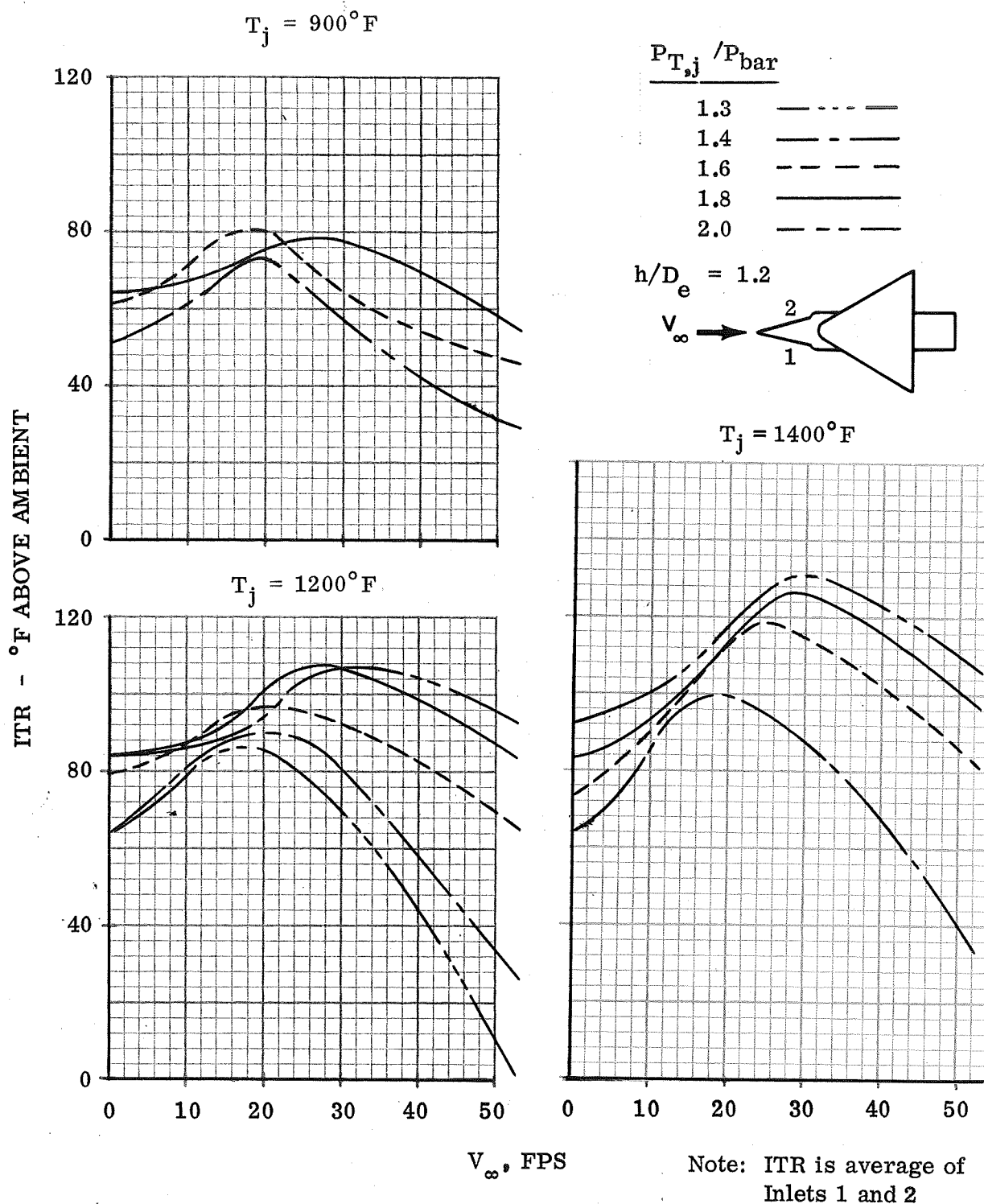
Figure 12. - Variation of ITR With Head Winds, Side Inlets Configuration
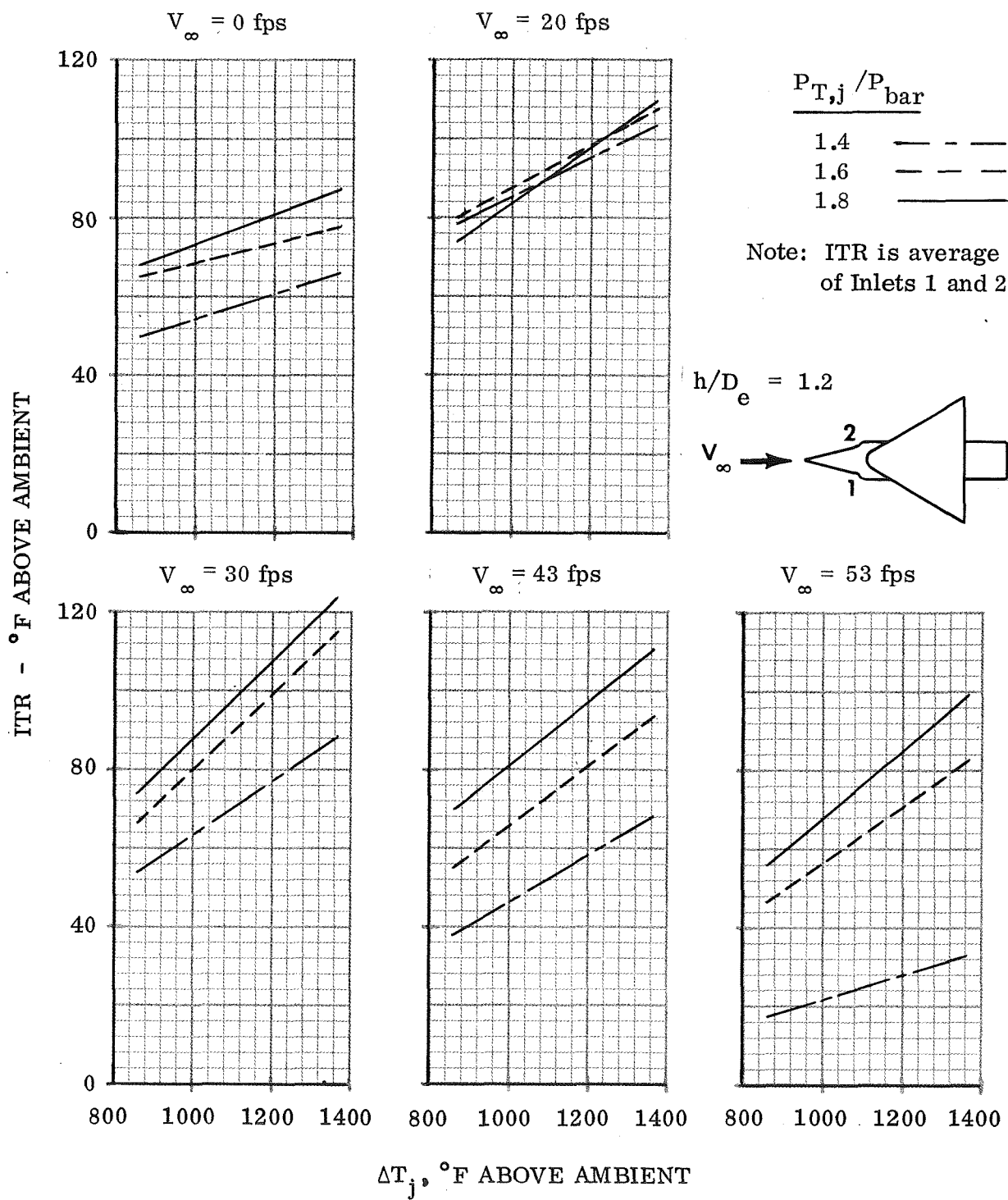
Figure 13. – Variation of ITR With Excess Exhaust Gas Temperature, Side Inlets Configuration
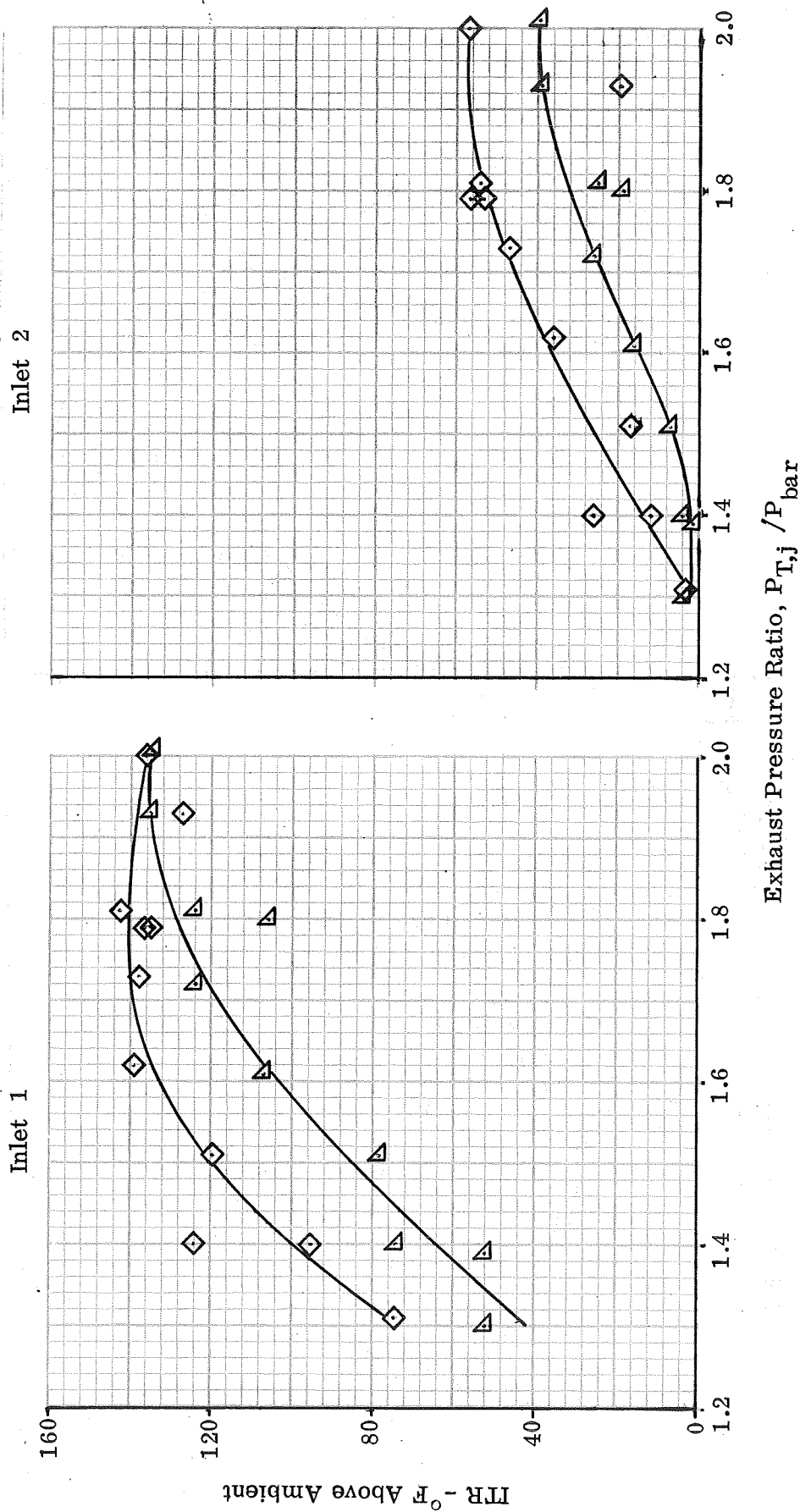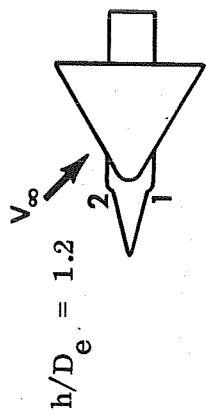
Figure 14. – Variation of ITR With Exhaust Pressure Ratio For Two Wind Speeds, Side Inlets Configuration, $T_j = 1200°F$

(a) $\psi = -45°$

(b) $\psi = -90°$
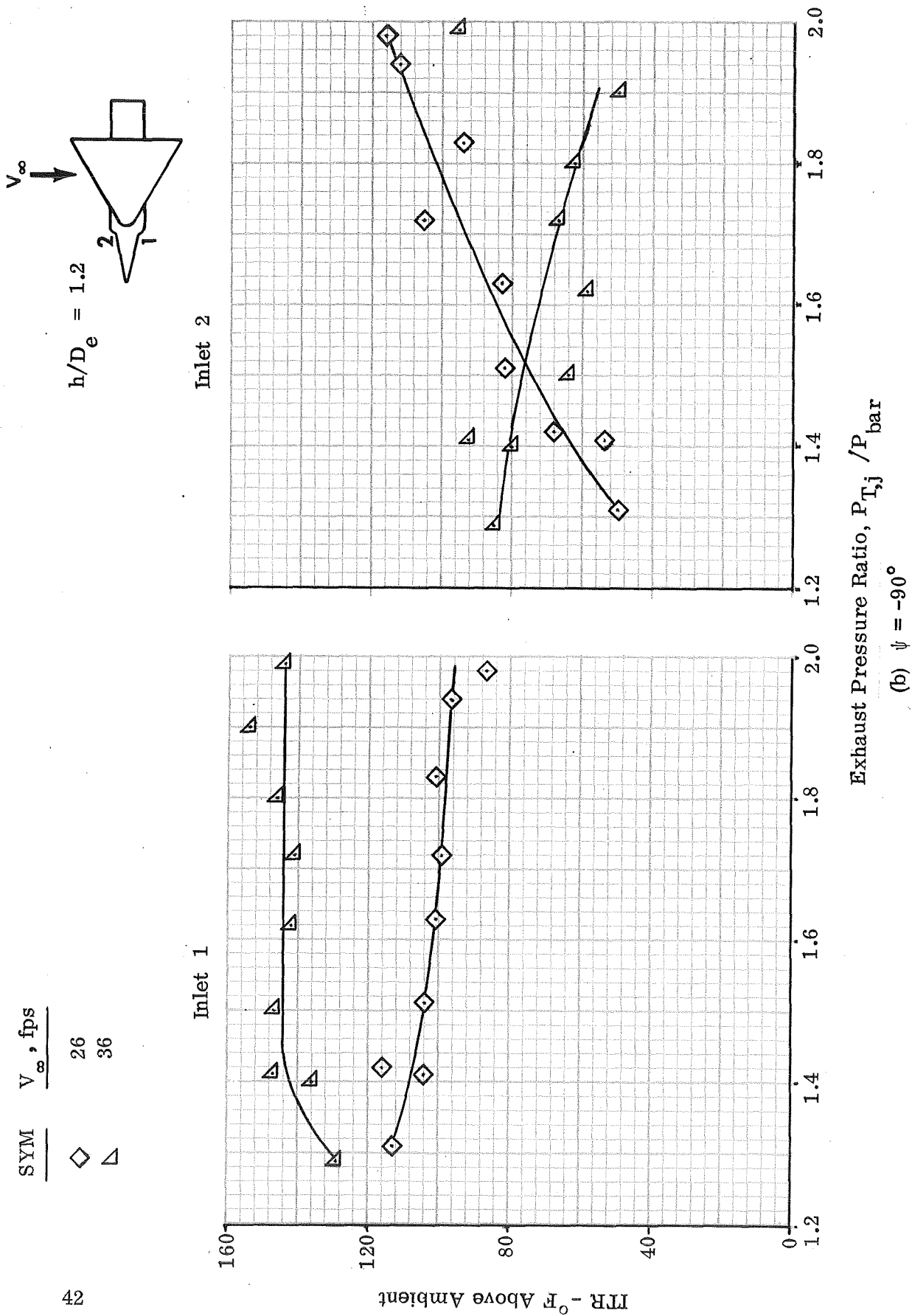
Figure 14. – Concluded.

42
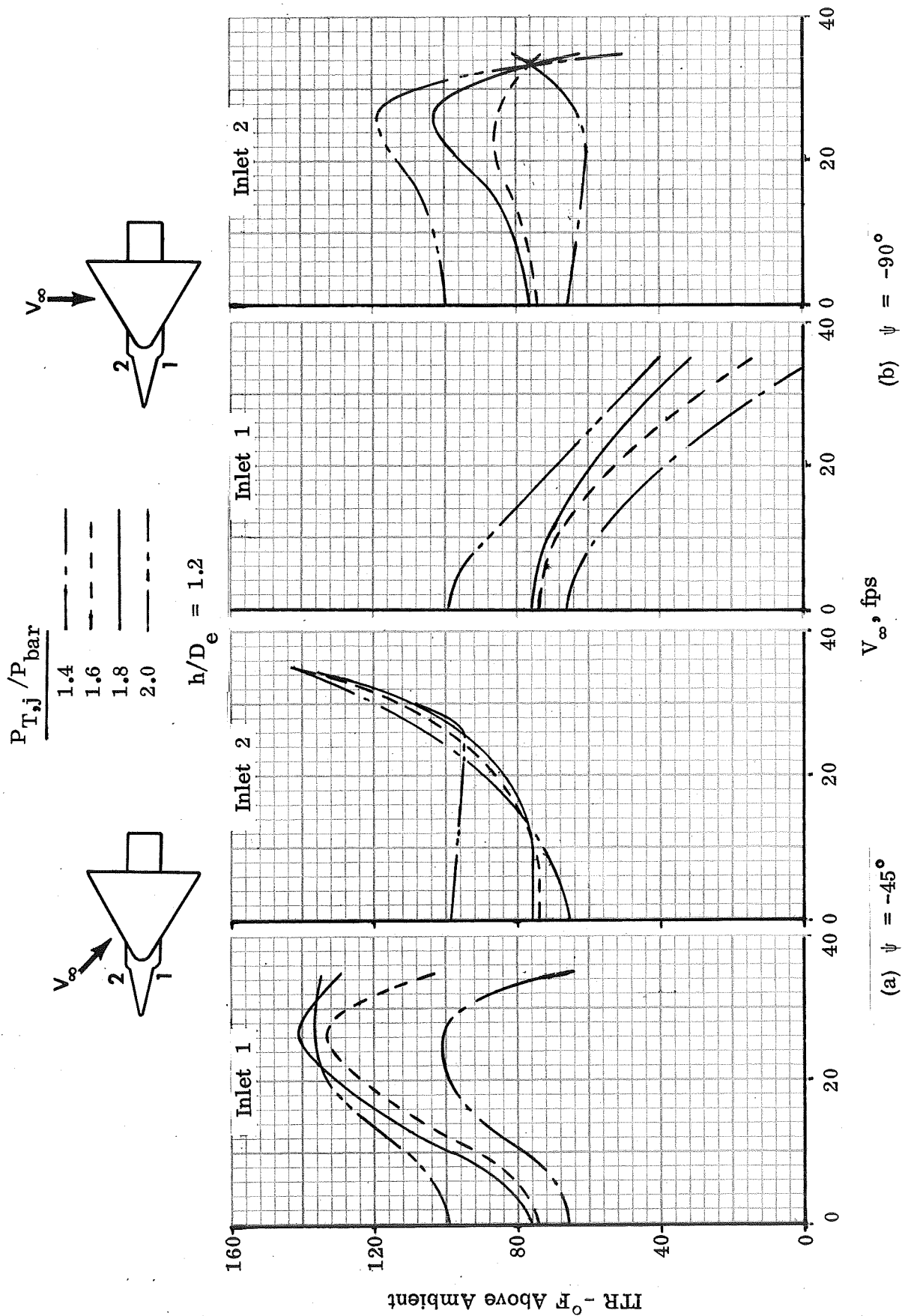
Figure 15. – Variation of ITR With V_∞ For Side Inlets Configuration at $\psi = -45°$ and $-90°$, $T_j = 1200°F$

(a) $\psi = -45°$ (b) $\psi = -90°$

$\dfrac{P_{T,j}}{P_{bar}}$

1.4
1.6
1.8
2.0

$h/D_e = 1.2$

43
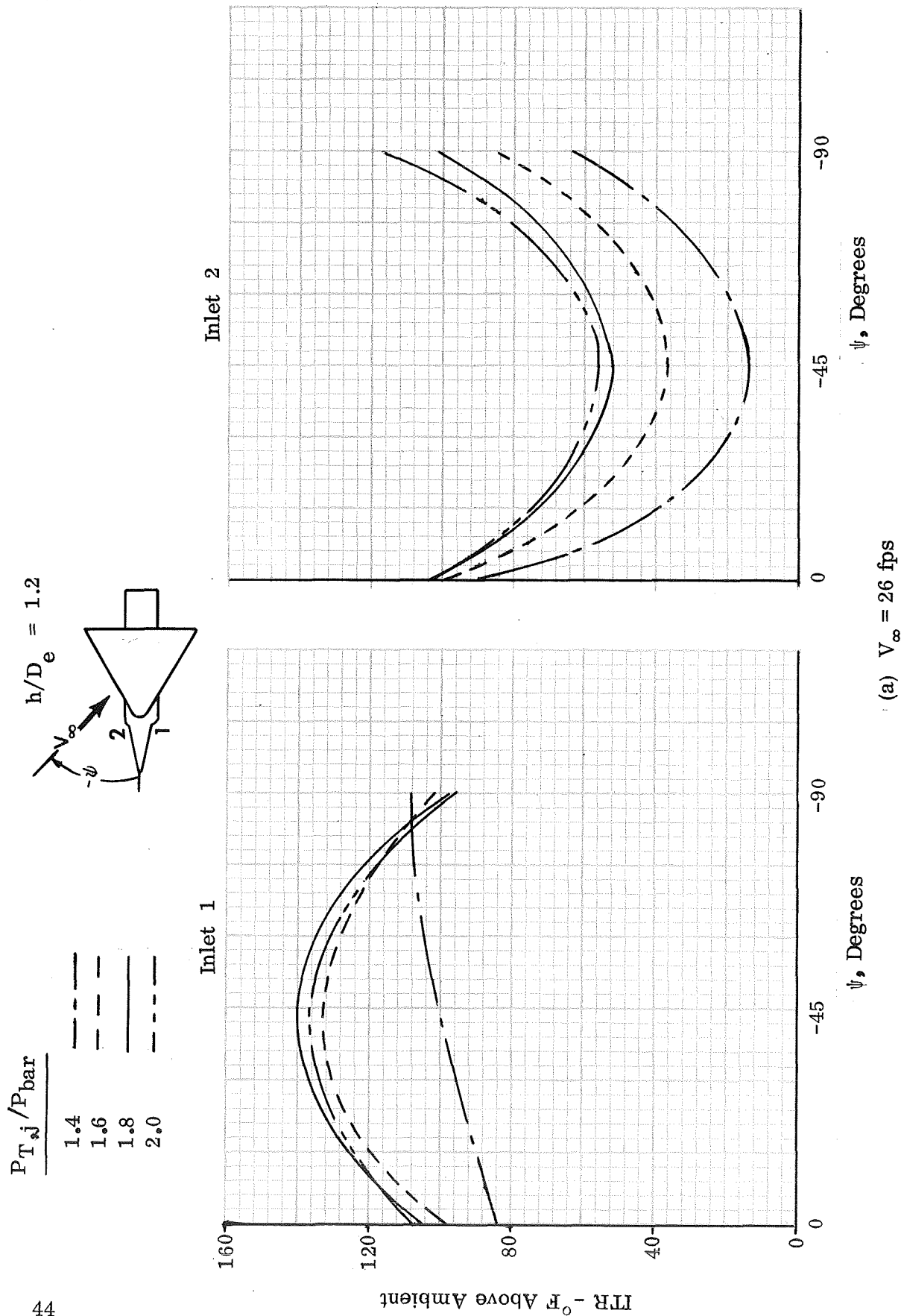
Figure 16. – Variation of ITR With ψ For Side Inlets Configuration, $T_j = 1200°F$

(a) $V_\infty = 26$ fps
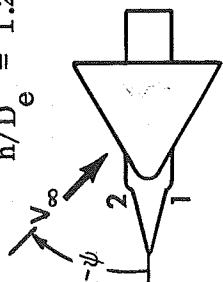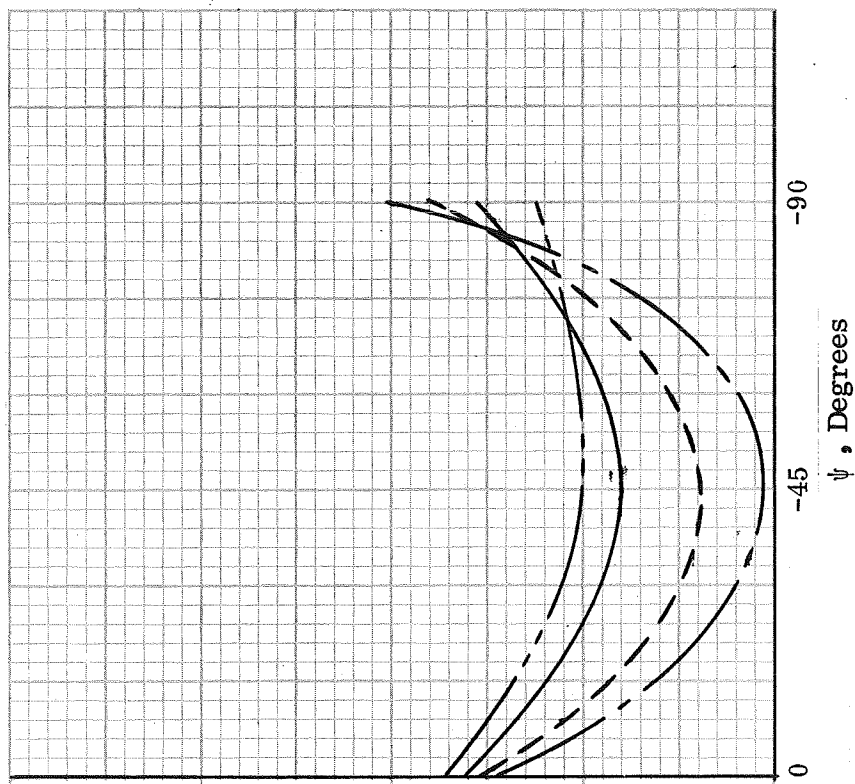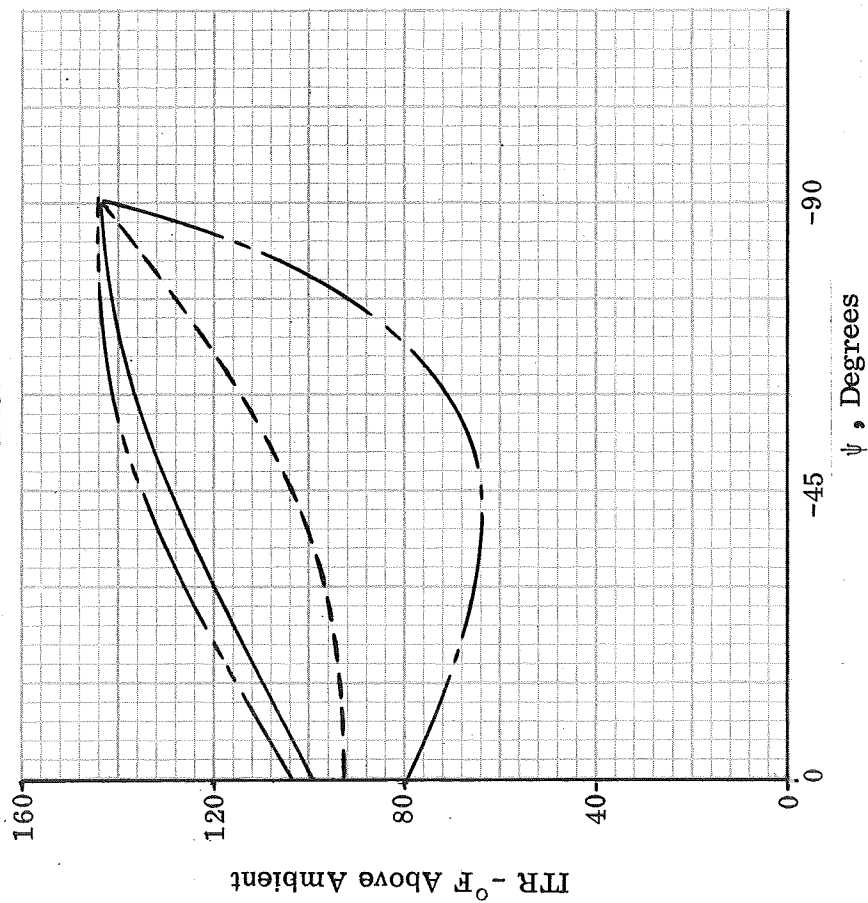
(b) $V_\infty = 36$ fps

Figure 16. - Concluded.

45
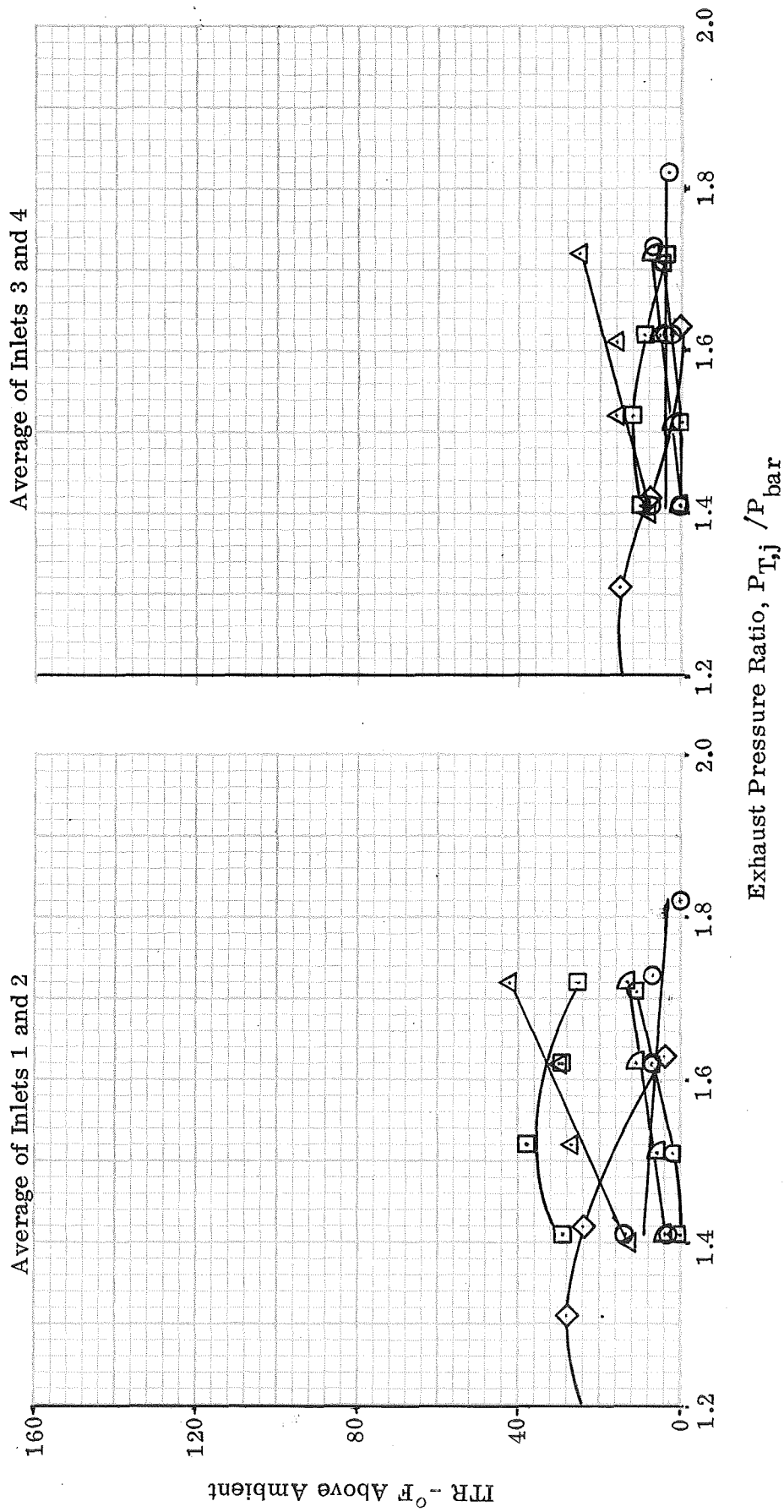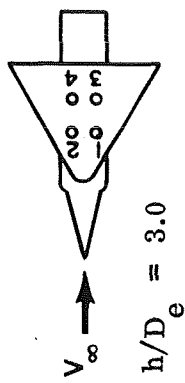
Figure 17. – Variation of ITR With Exhaust Pressure Ratio For Various Wind
Speeds, Top Inlets Configuration, $\psi = 0°$.

(a) $T_j = 900°F$.
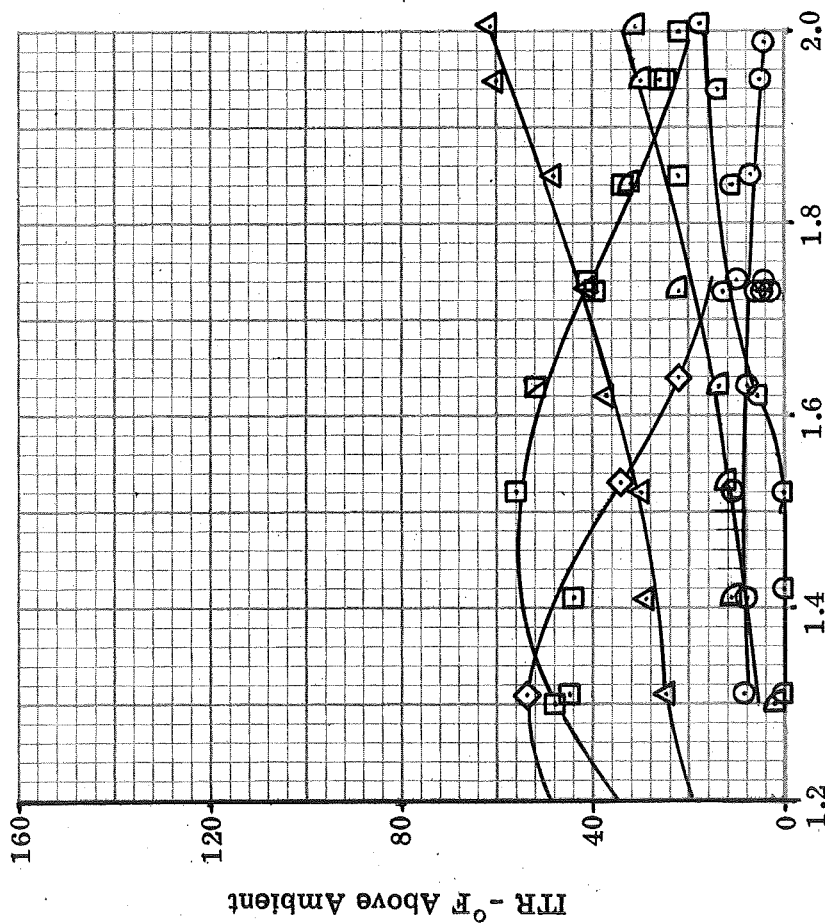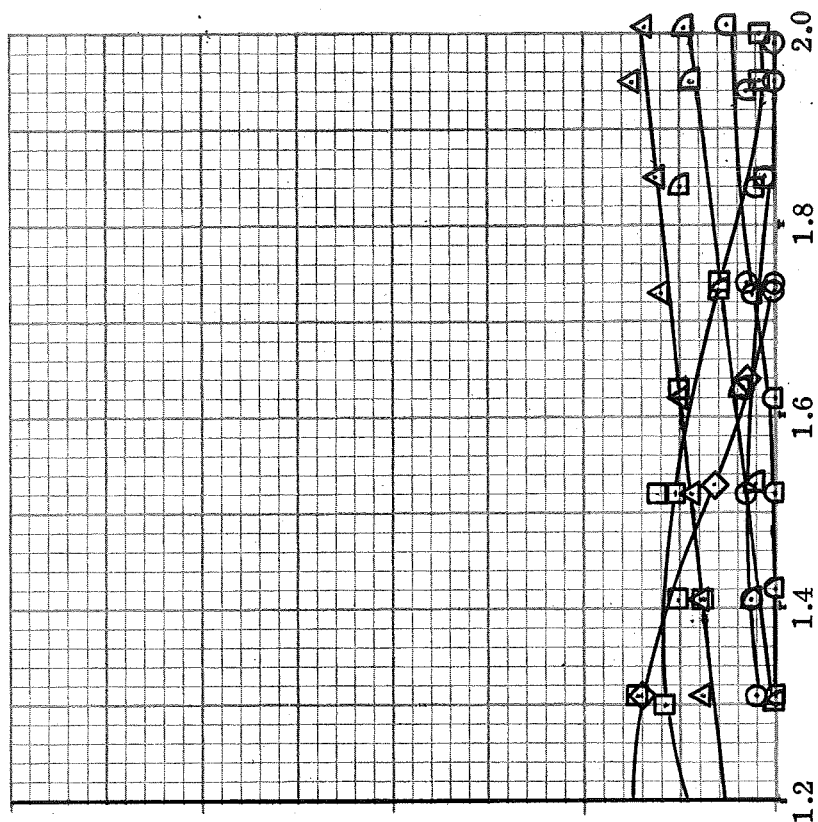
(b) $T_j = 1200°F$.

Figure 17. – Continued.
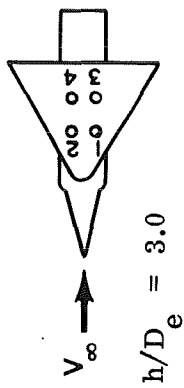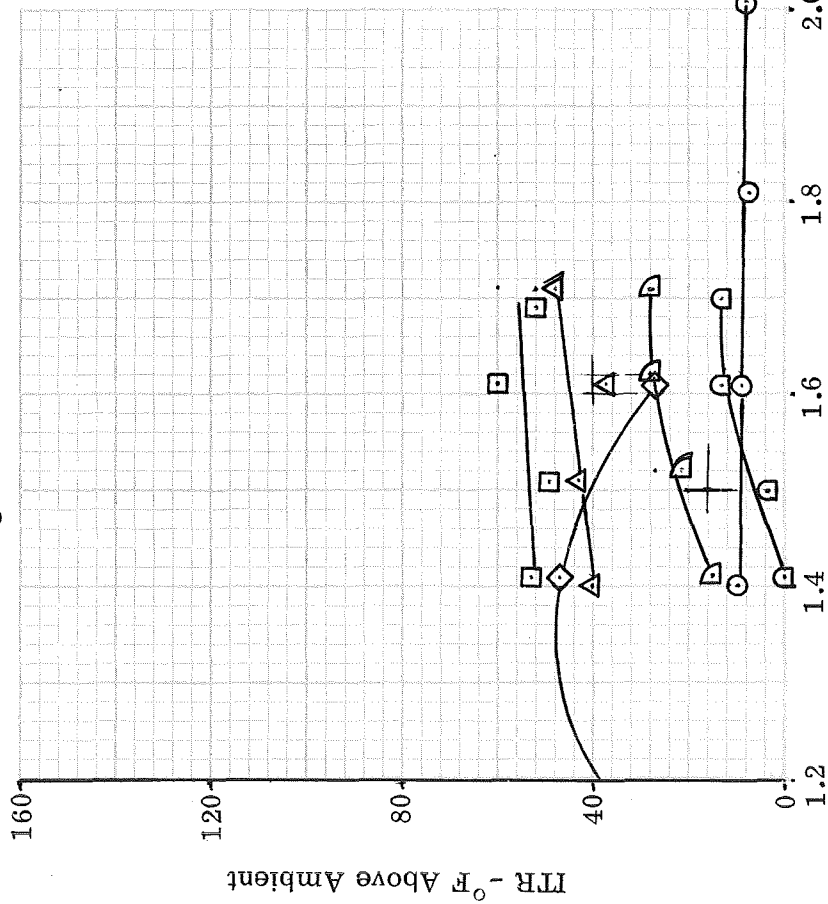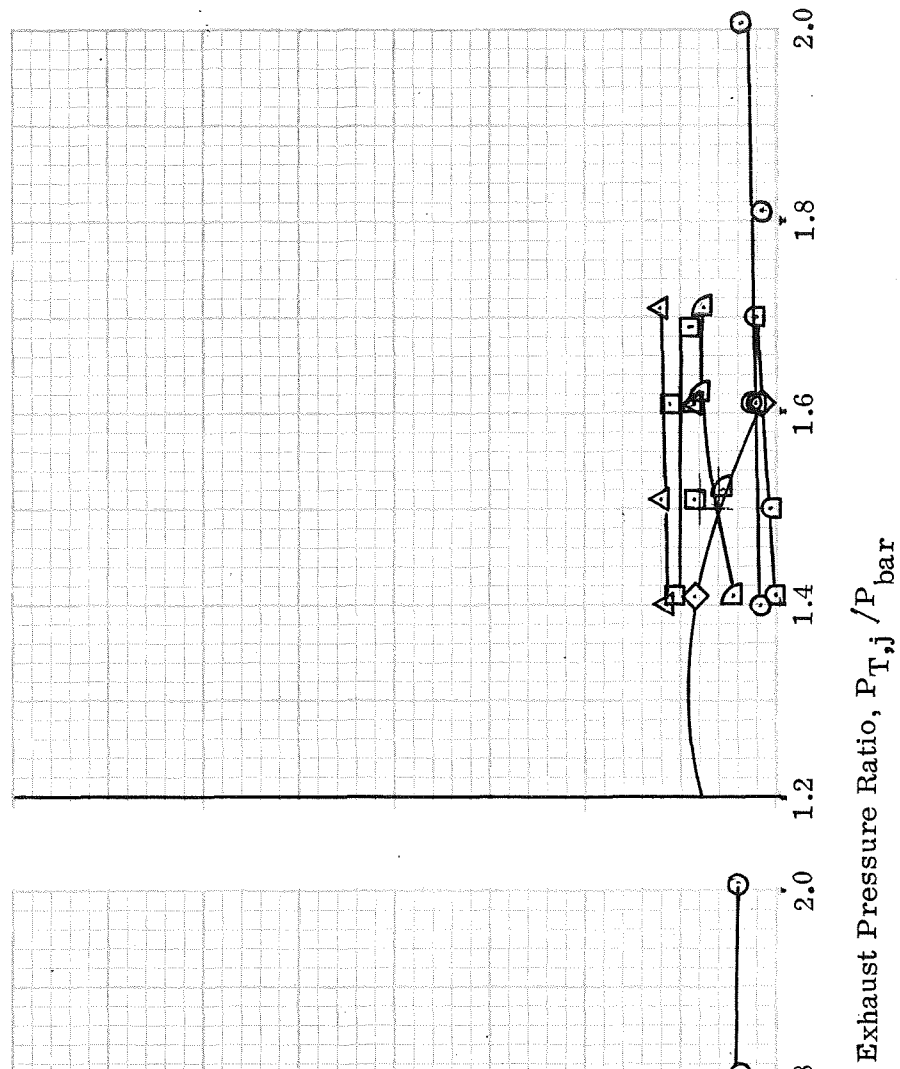
(c) $T_j = 1400°F.$

Figure 17. - Concluded.
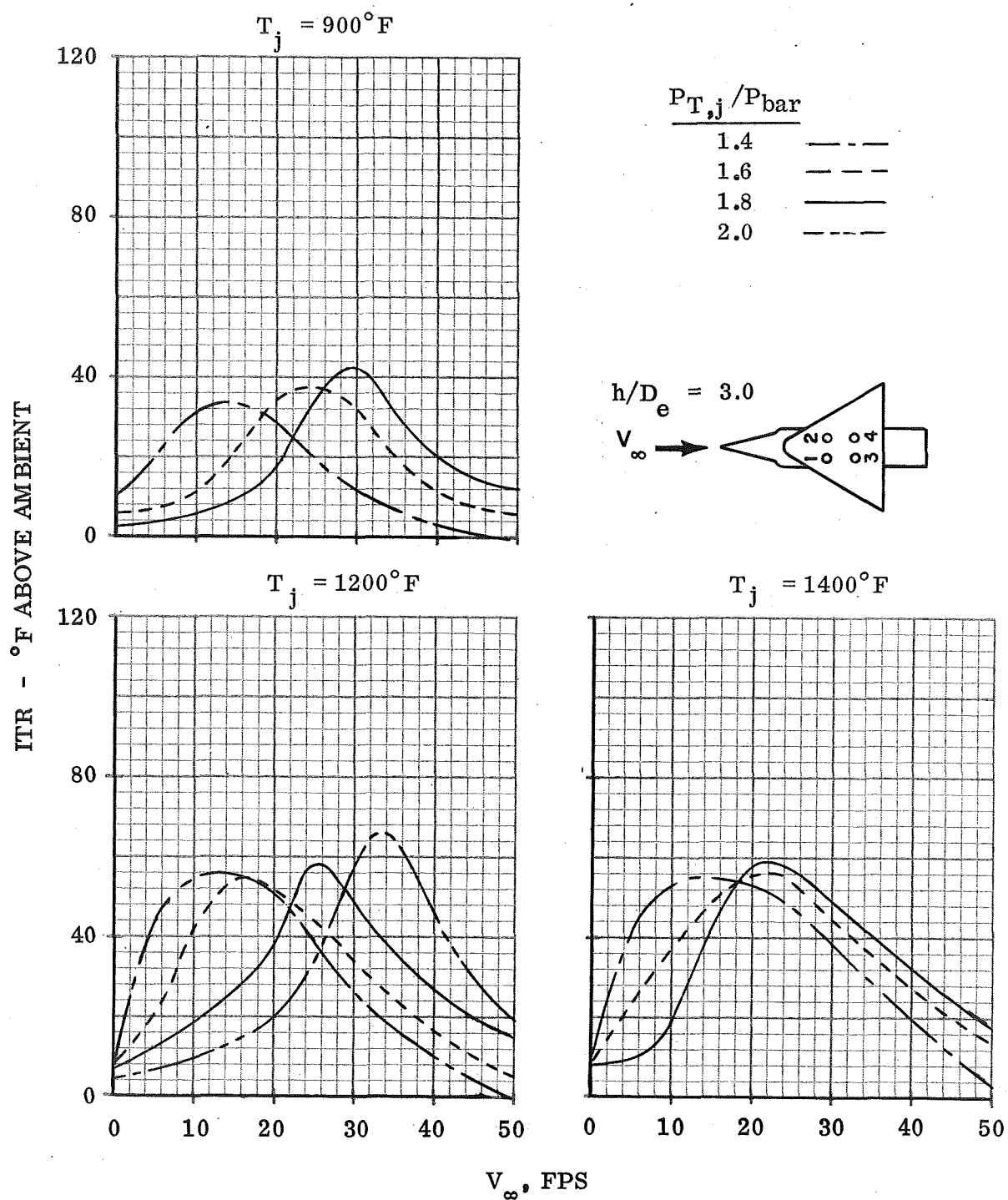
Figure 18. - Variation of ITR With Head Winds, Top Inlets Configuration
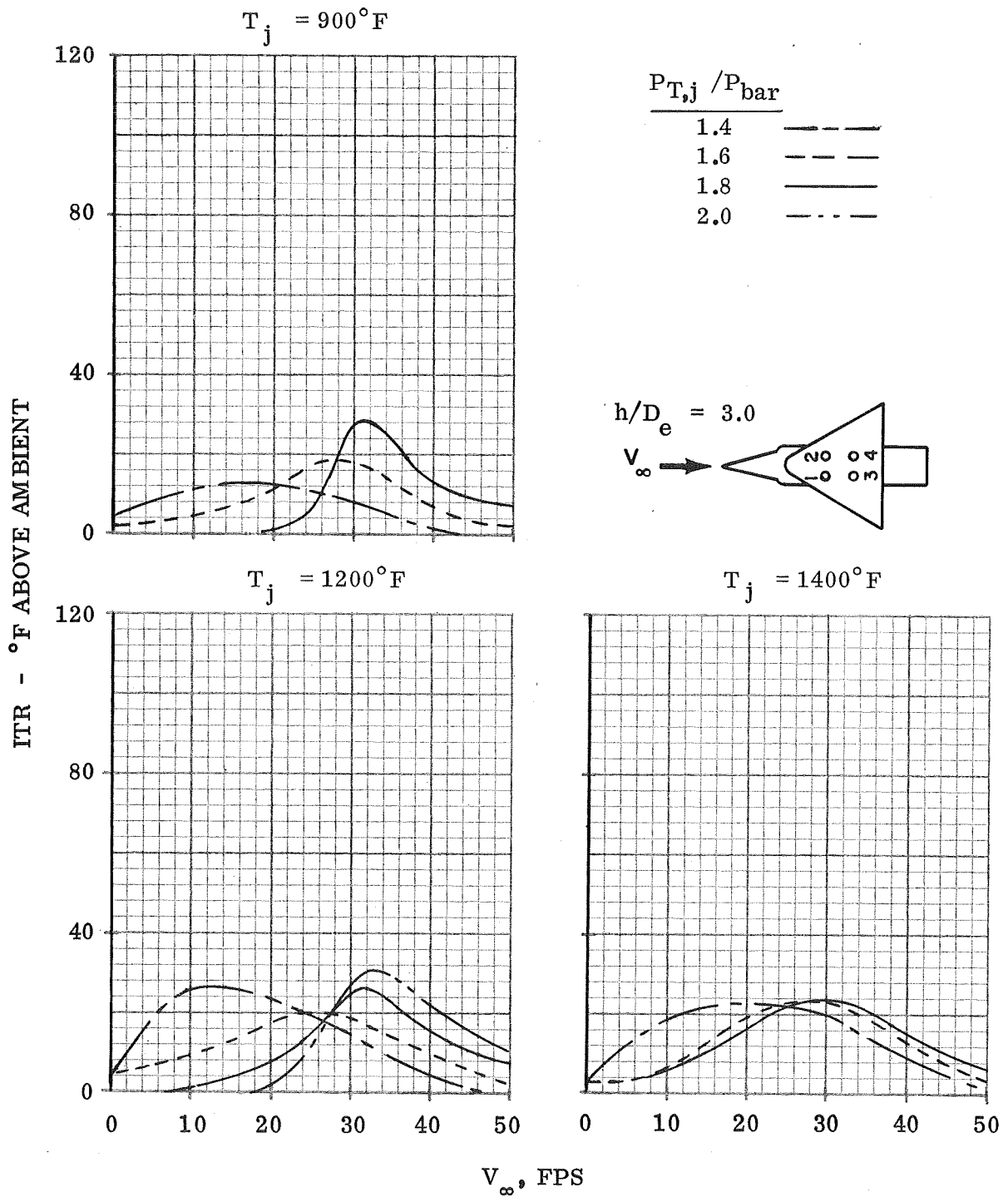
(b) Average of Inlets 3 and 4

Figure 18. - Concluded.

$h/D_e = 3.0$

$V_\infty \longrightarrow$

$P_{T,j}/P_{bar}$

1.4	—— — —
1.6	—— — —
1.8	——————

$V_\infty = 0$ fps

$V_\infty = 7$ fps

$V_\infty = 20$ fps

$V_\infty = 30$ fps

$V_\infty = 43$ fps

$V_\infty = 53$ fps

ITR – °F ABOVE AMBIENT

800   1000   1200   1400   800   1000   1200   1400   800   1000   1200   1400
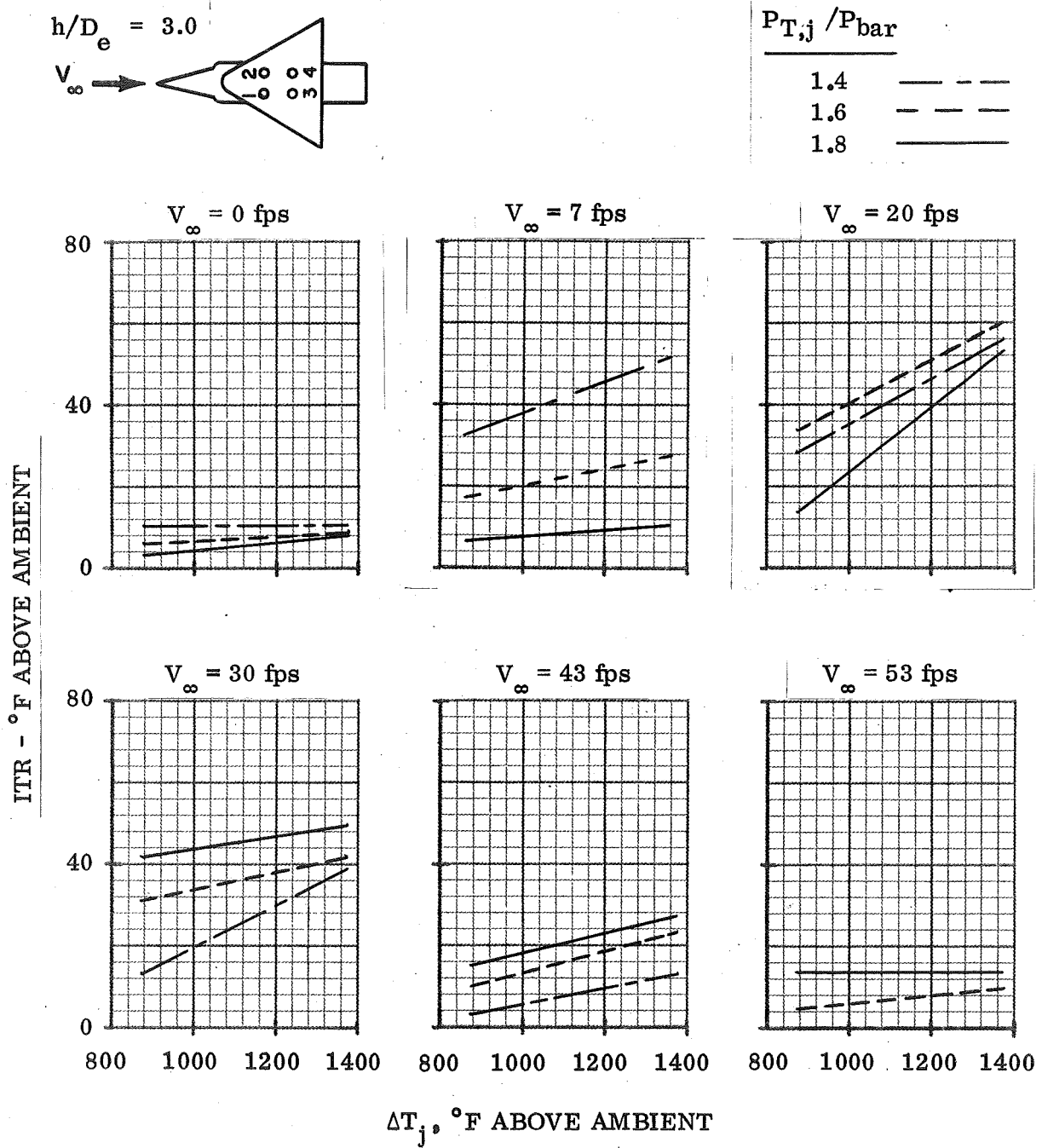
ΔT_j, °F ABOVE AMBIENT

(a) Average of Inlets 1 and 2

Figure 19. – Variation of ITR With Excess Exhaust Gas Temperature,
Top Inlets Configuration, $\psi = 0°$

h/D$_e$ = 3.0

V$_\infty$

$P_{T,j}/P_{bar}$

1.4	— — —
1.6	— — —
1.8	———

V$_\infty$ = 0 fps

V$_\infty$ = 7 fps

V$_\infty$ = 20 fps

V$_\infty$ = 30 fps

V$_\infty$ = 43 fps

V$_\infty$ = 53 fps

ITR - °F ABOVE AMBIENT
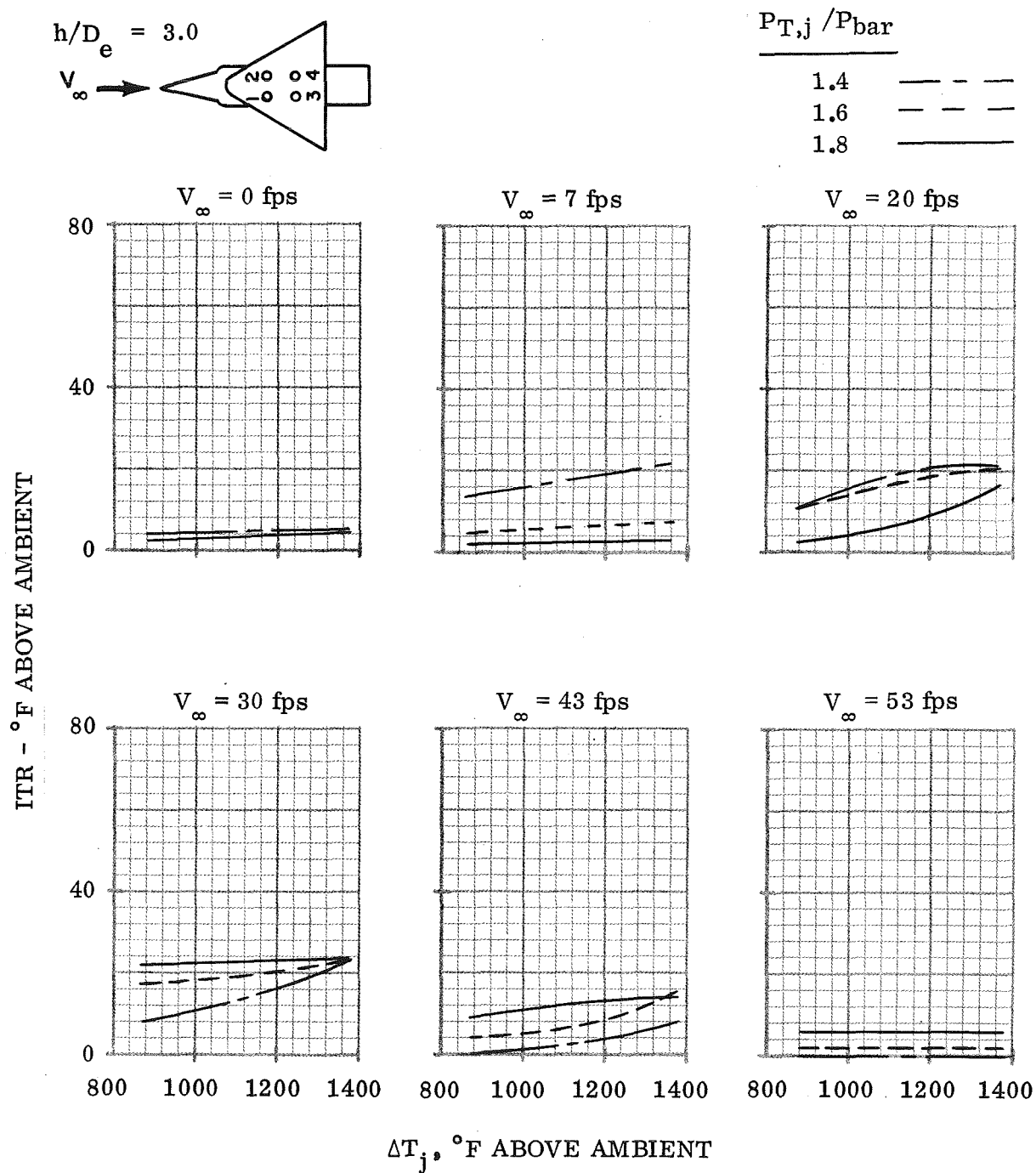
ΔT_j, °F ABOVE AMBIENT

(b) Average of Inlets 3 and 4

Figure 19. - Concluded.
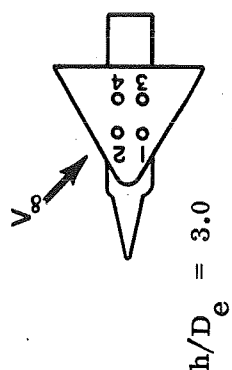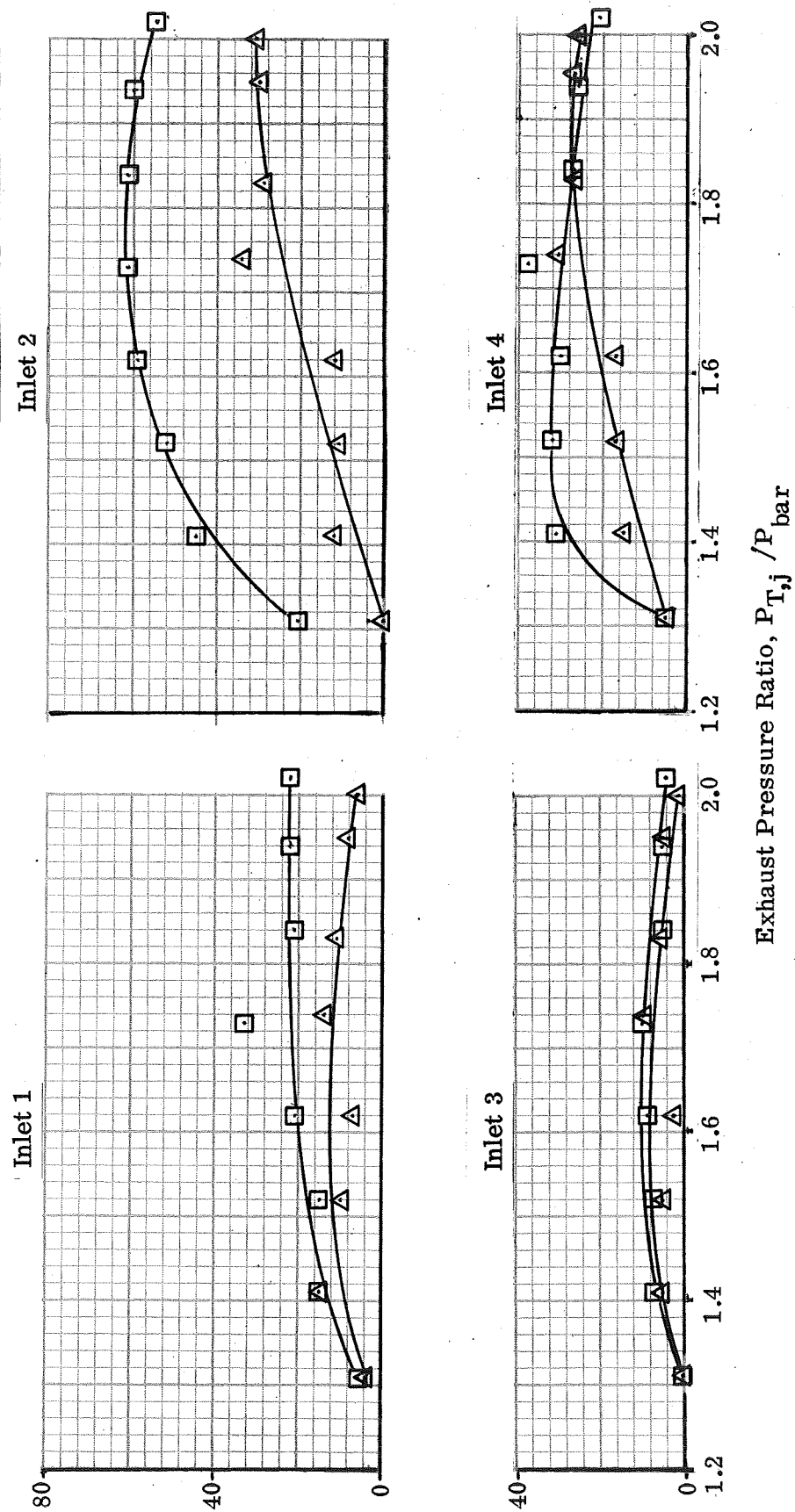
Figure 20. – Variation of ITR at Each Inlet With Exhaust Pressure Ratio for Two Wind Speeds, Top Inlets Configuration, $T_j = 1200°F$

(a) $\psi = -45°$
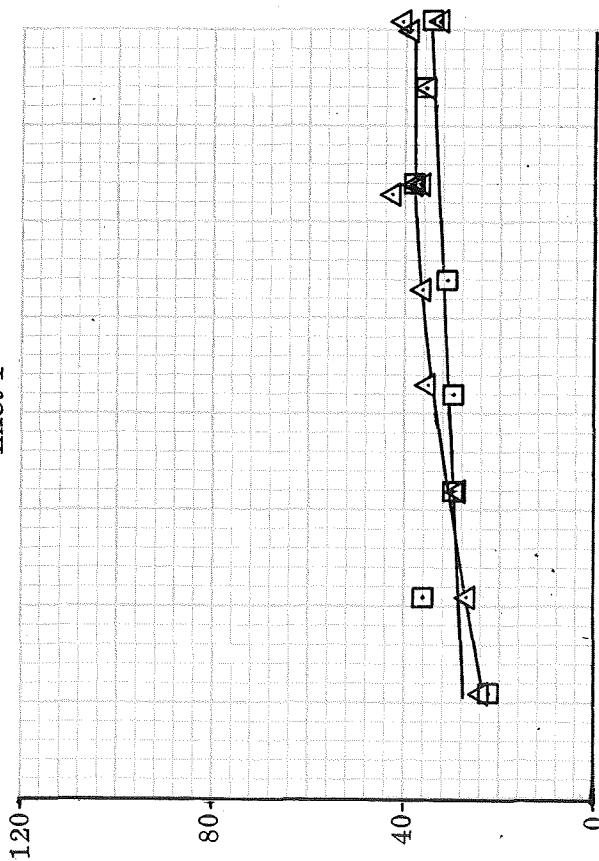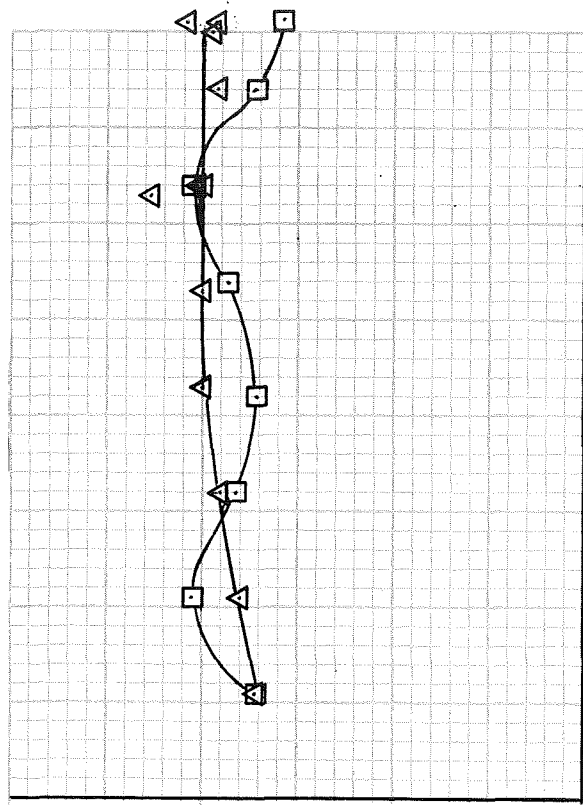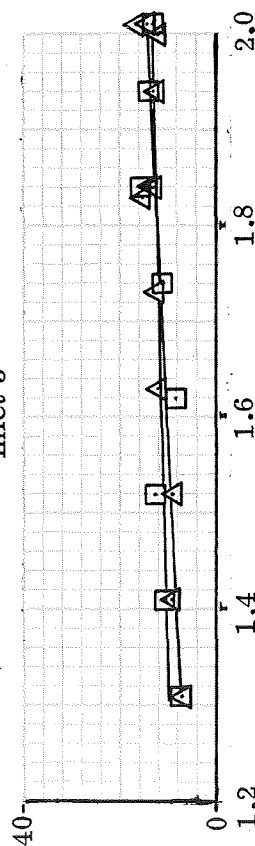
(b) $\psi = -90°$

Figure 20. – Concluded.

Figure 21. – Variation of ITR With V_∞ for Top Inlets Configuration at Various ψ, $T_j = 1200°$F

(a) $\psi = 0$

ITR – °F ABOVE AMBIENT

Inlet 1

Inlet 2

$h/D_e = 3.0$

V_∞

P_{T_j}/P_{bar}

1.4	– – –
1.6	– –
1.8	——
2.0	–•–

Inlet 3

Inlet 4

V_∞, fps

(b) $\psi = -45°$

Figure 21. – Continued.

Inlet 1 Inlet 2

Inlet 3 Inlet 4

ITR - °F ABOVE AMBIENT

$h/D_e = 3.0$

V_∞
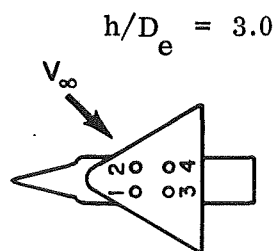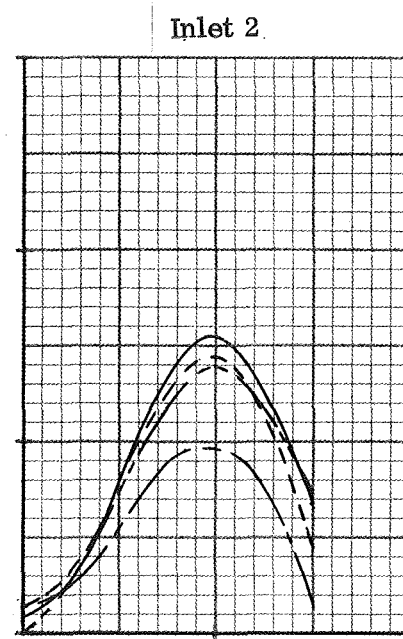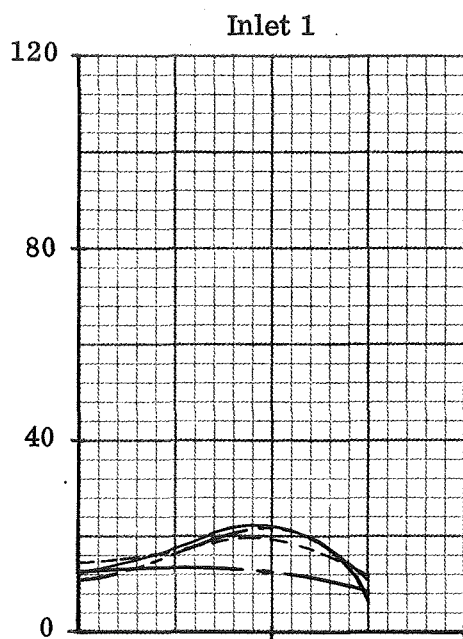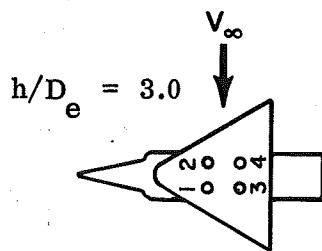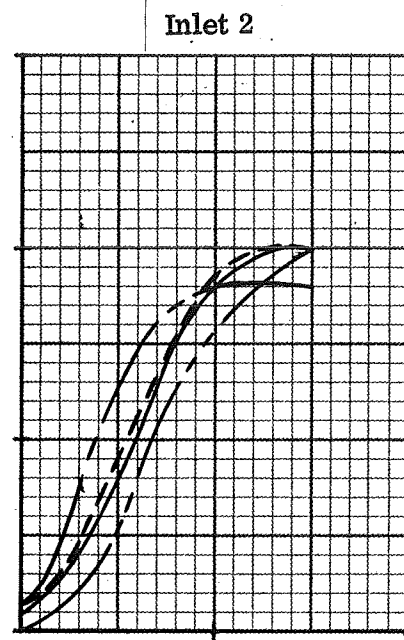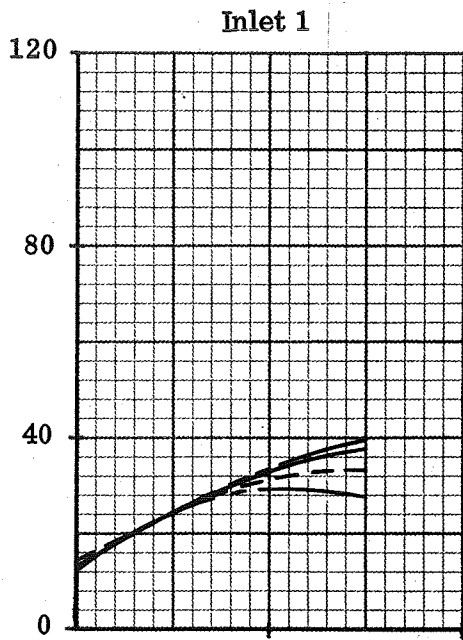
$P_{T,j}/P_{bar}$

1.4	— - - —
1.6	— — —
1.8	———
2.0	— - - -
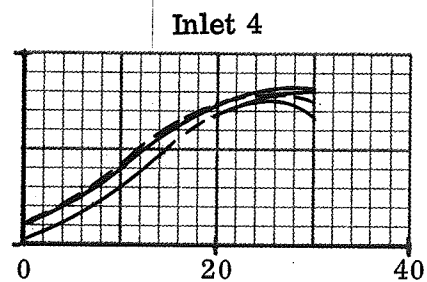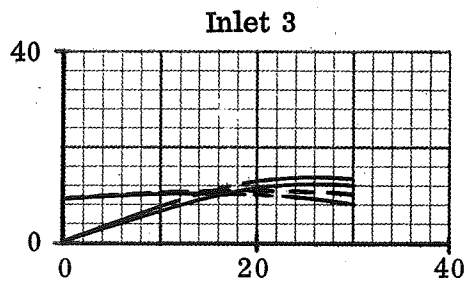
V_∞, fps

(c) $\psi = -90°$

Figure 21. - Concluded.
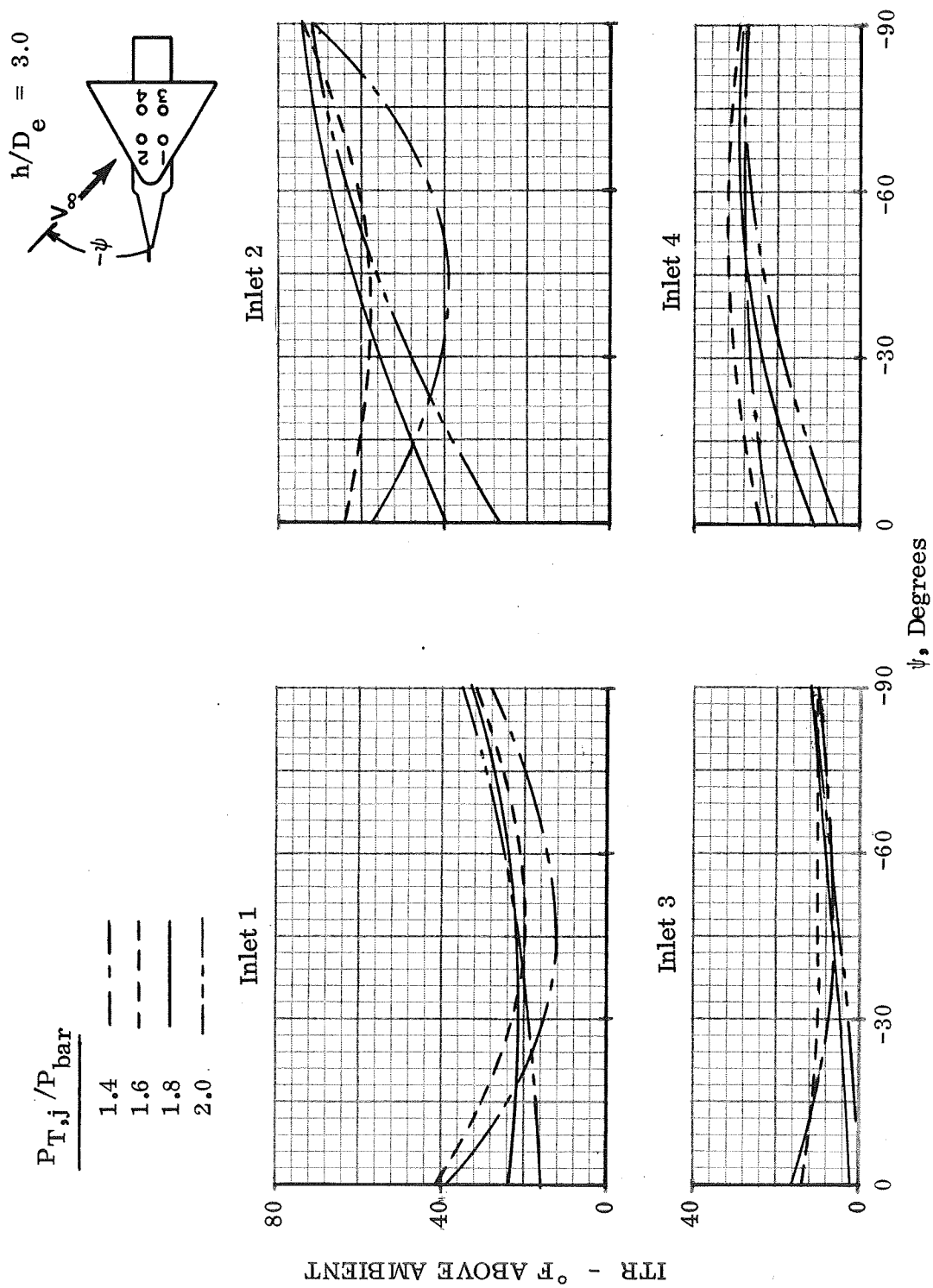
Figure 22. – Variation of ITR With ψ for Top Inlets Configuration; $T_j = 1200°F$

(a) $V_\infty = 20$ fps

(b) $V_\infty = 30$ fps

Figure 22. – Concluded.

Note: ITR is average of Inlets 1 and 2

(a) $T_j = 900°F$
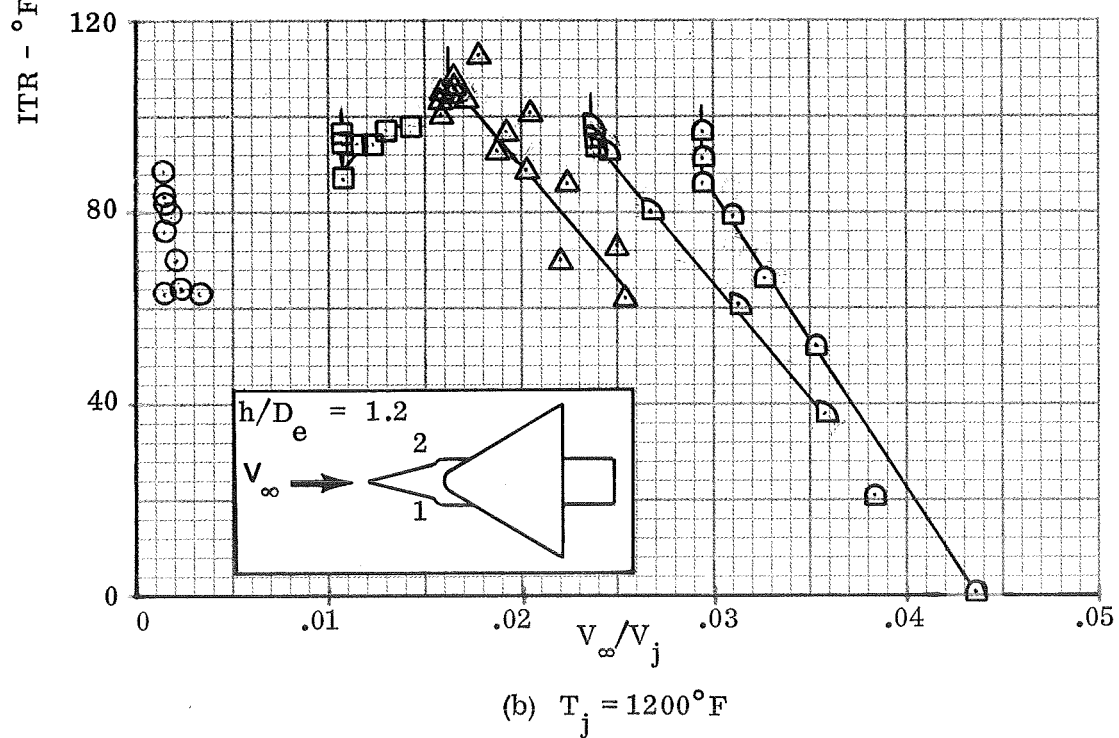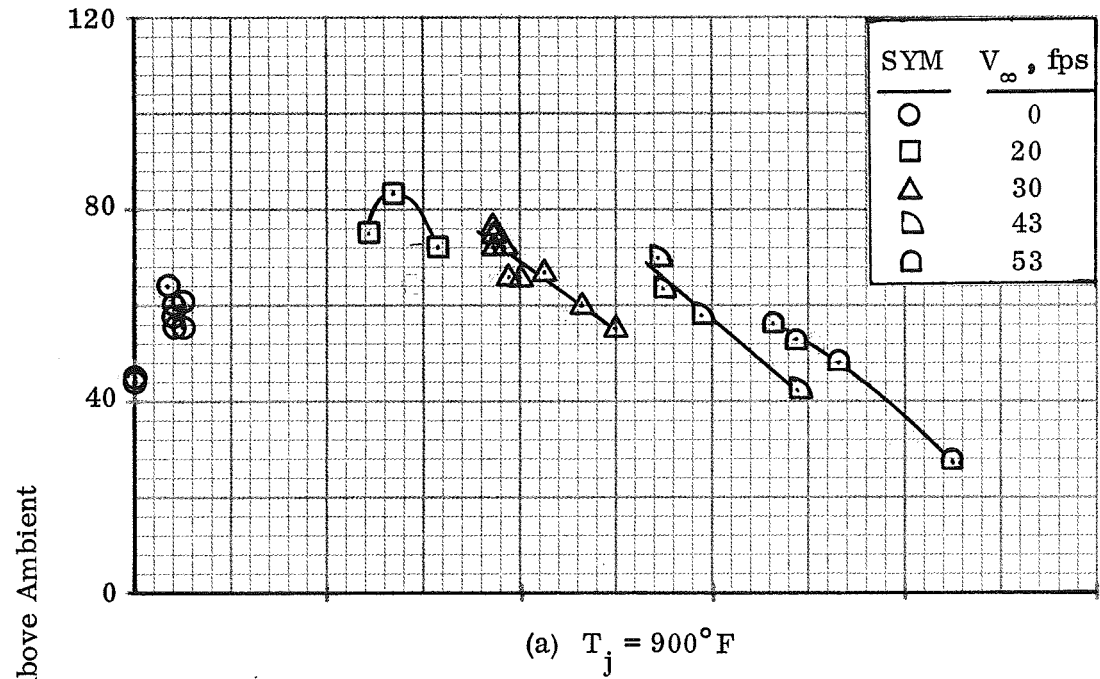
(b) $T_j = 1200°F$

Figure 23. – Variation of ITR With V_∞/V_j for Side Inlets Configuration, $\psi = 0°$
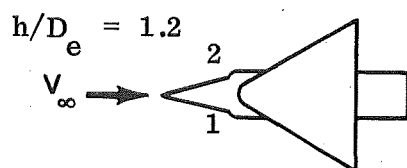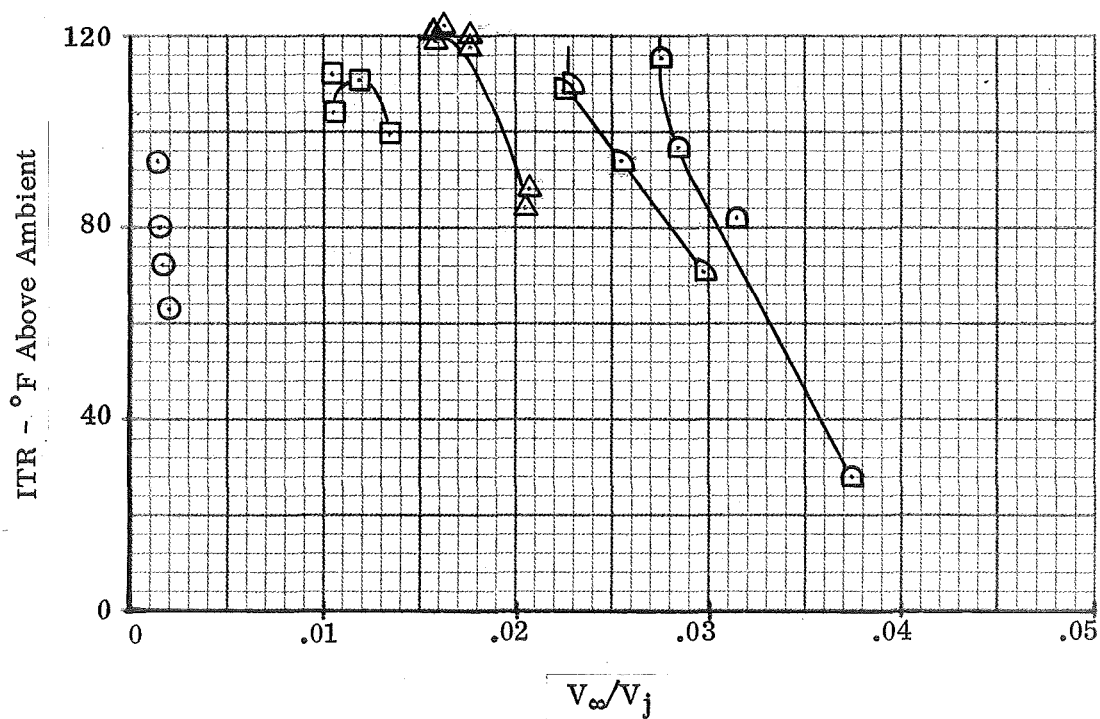
(c) $T_j = 1400°F$

Figure 23. – Concluded.

(a) $\psi = -45°$
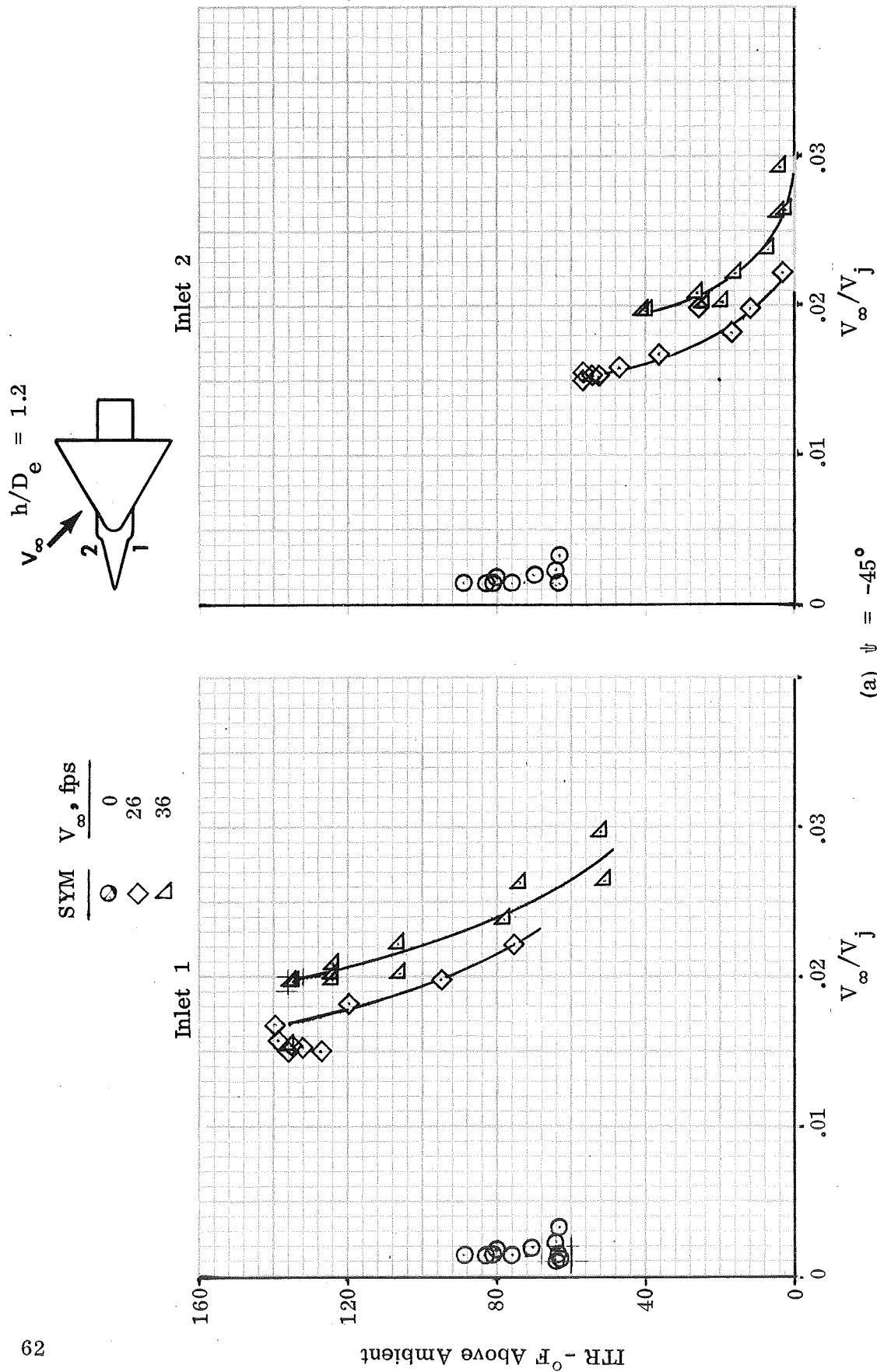
Figure 24. – Variation of ITR With V_∞/V_j for Side Inlets Configuration; $T_j = 1200°$ F
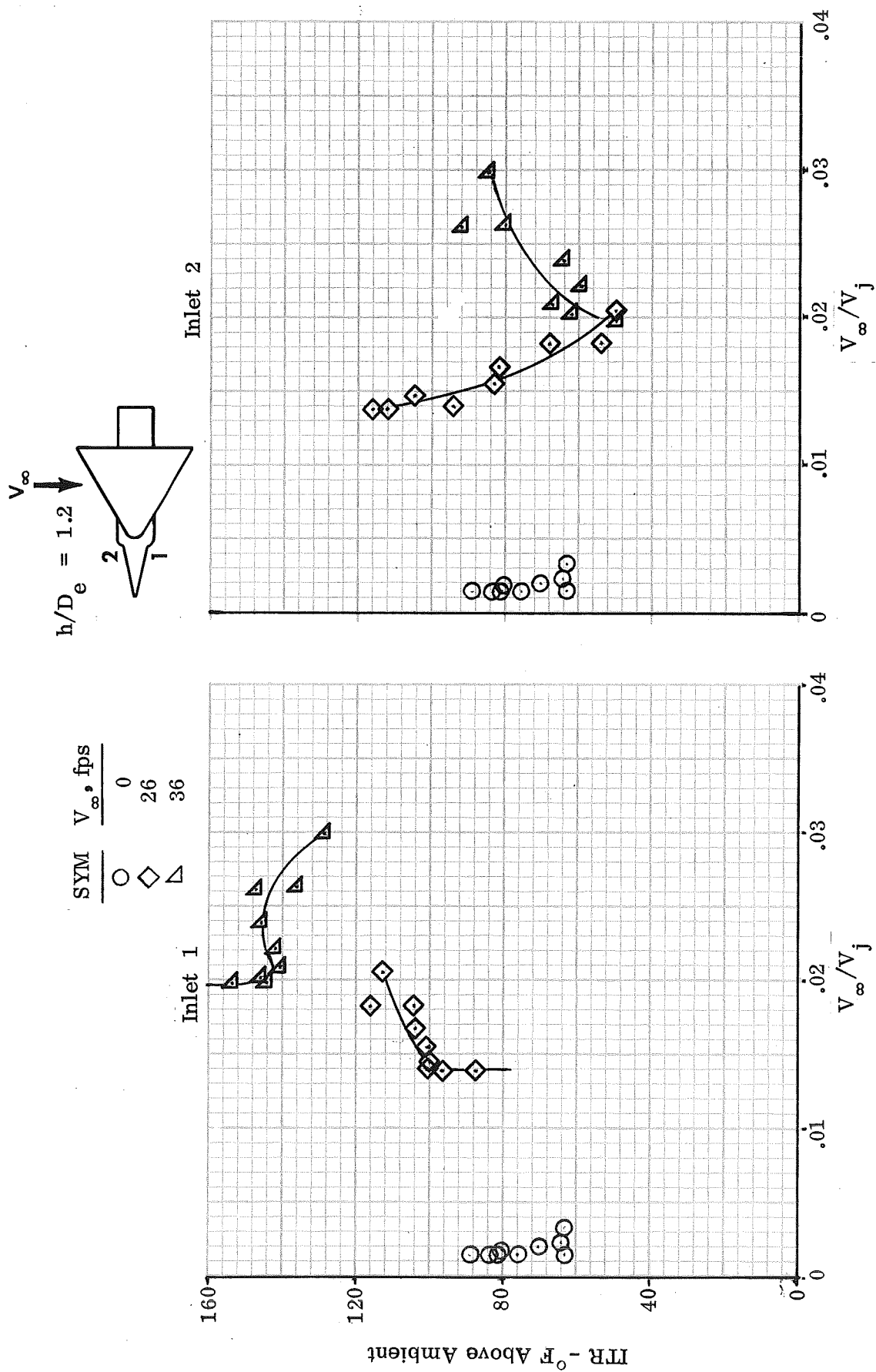
(b) $\psi = -90$

Figure 24. - Concluded.
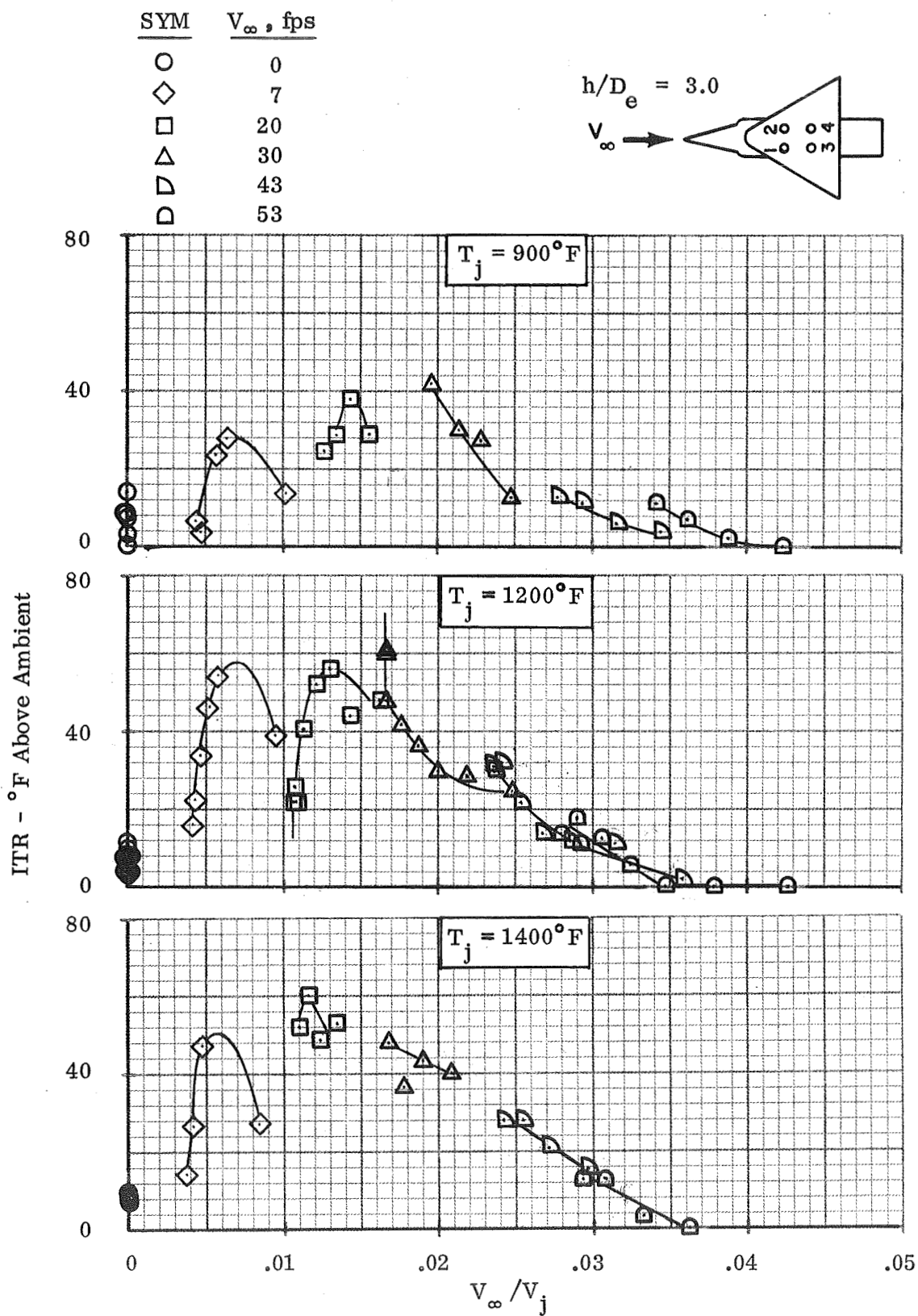
(a) Average of Inlets 1 and 2

Figure 25. – Variation of ITR With V_∞/V_j for Top Inlets Configuration, $\psi = 0°$
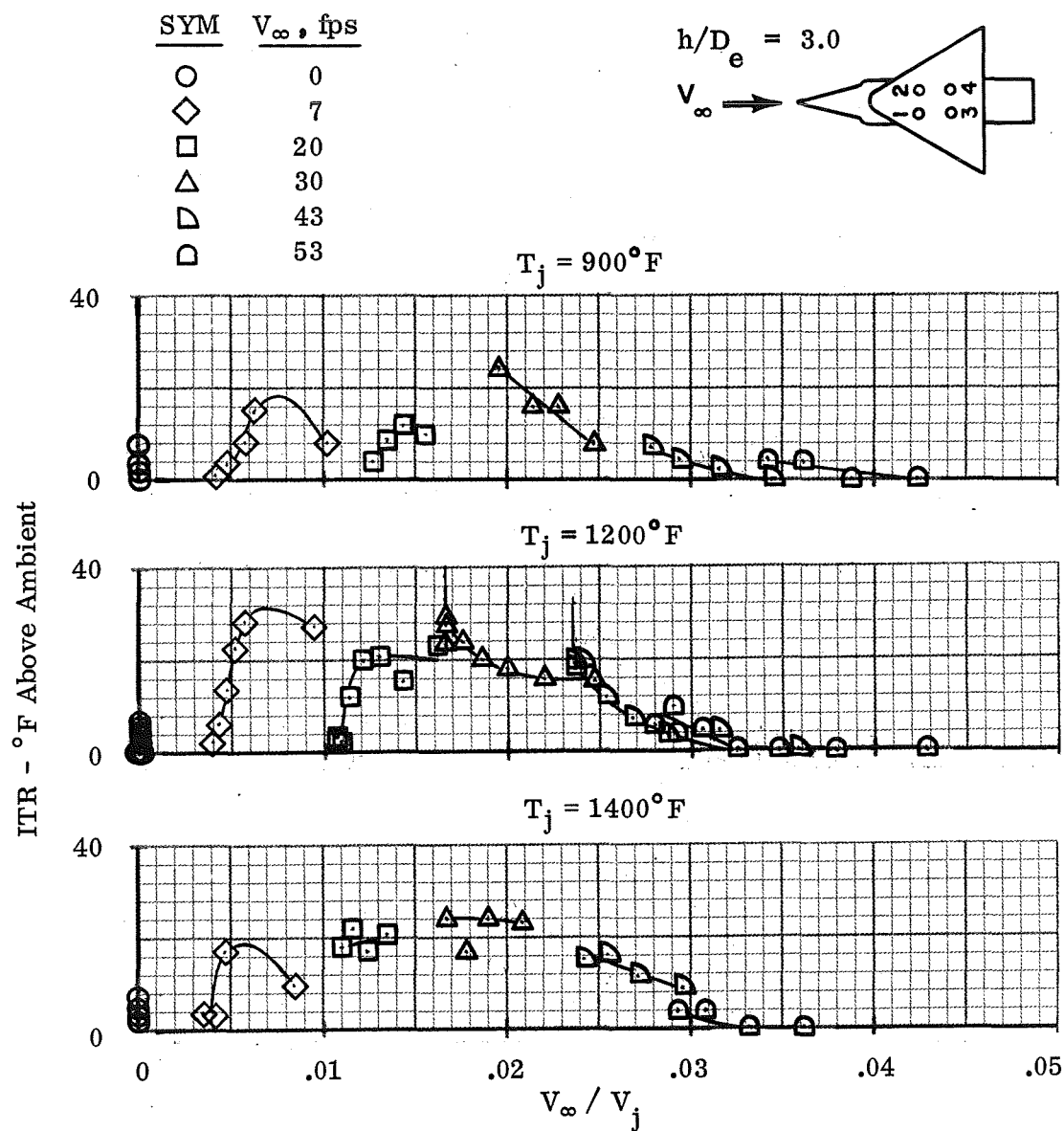
(b) Average of Inlets 3 and 4

Figure 25. – Concluded.

65

Figure 26. – Variation of ITR With V_∞/V_j for Top Inlets Configuration, $T_j = 1200°$F

(a) $\psi = -45°$

$h/D_e = 3.0$
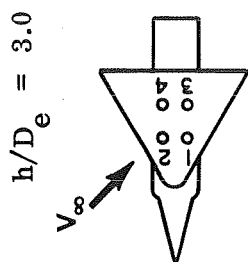
Figure 26. – Concluded.

(b) $\psi = -90°$

NOTE: INDICATES 3 DATA POINTS DEFINED BY ONE SYMBOL

67
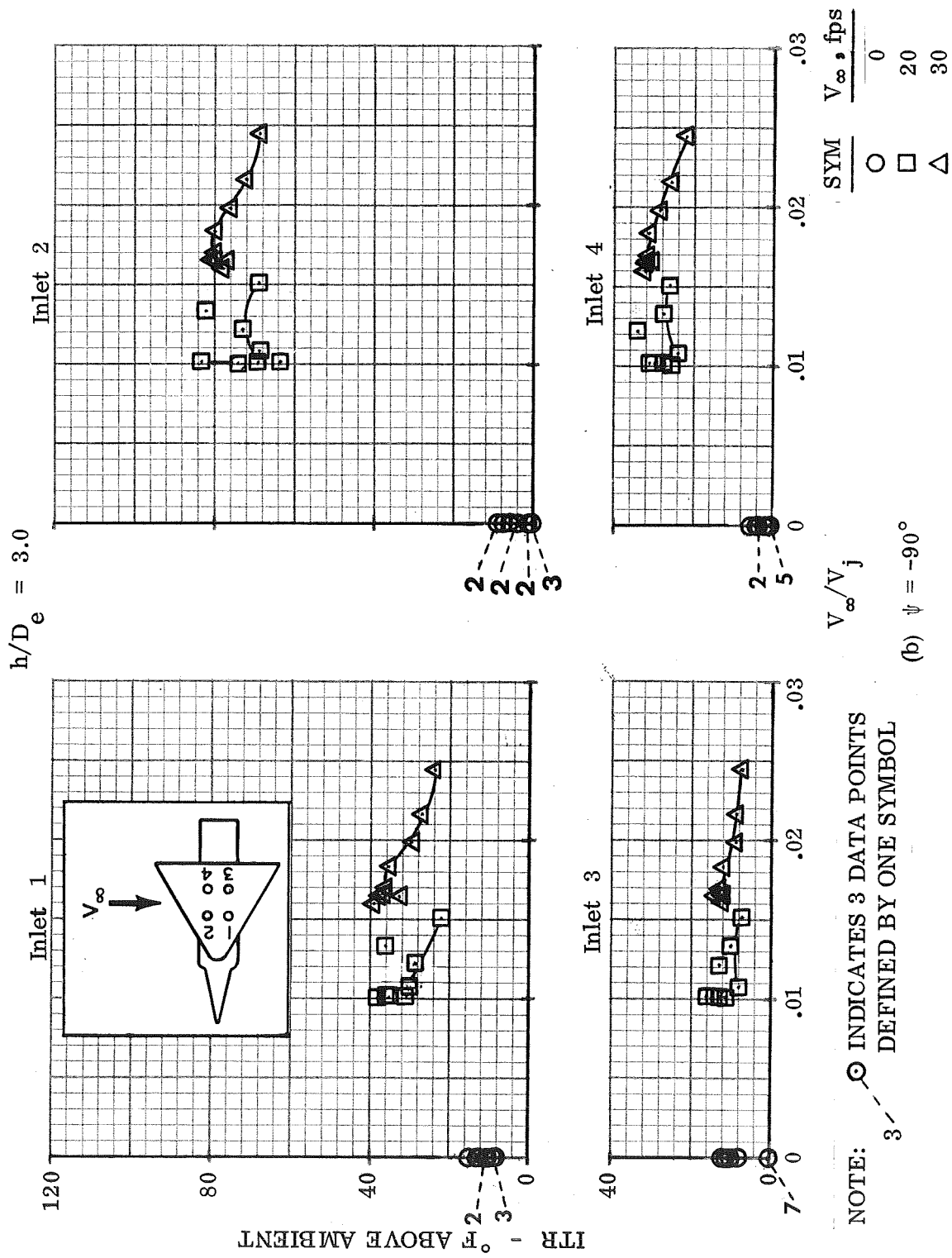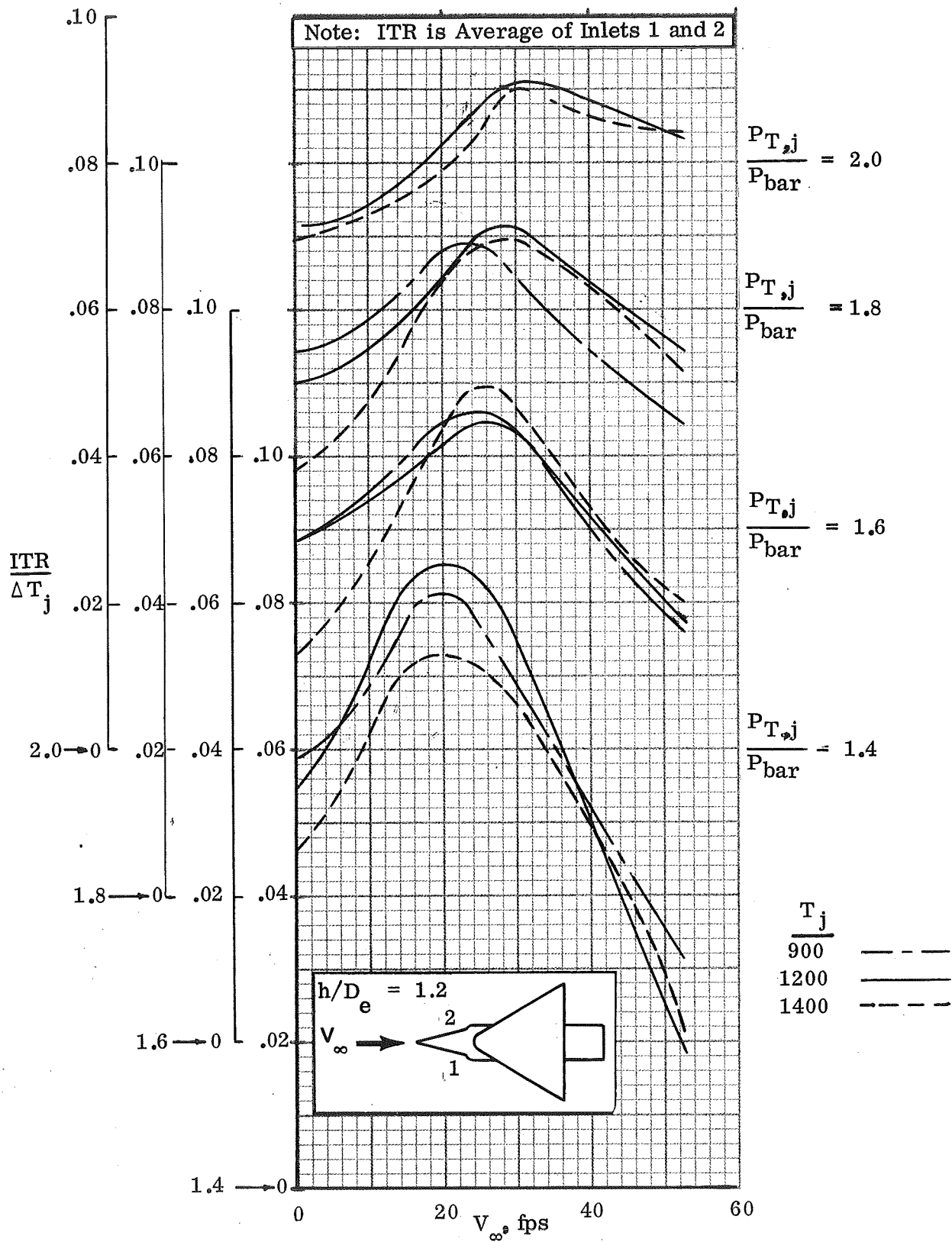
Figure 27. – Effect of Normalizing ITR to ΔT_j,
Side Inlets Configuration
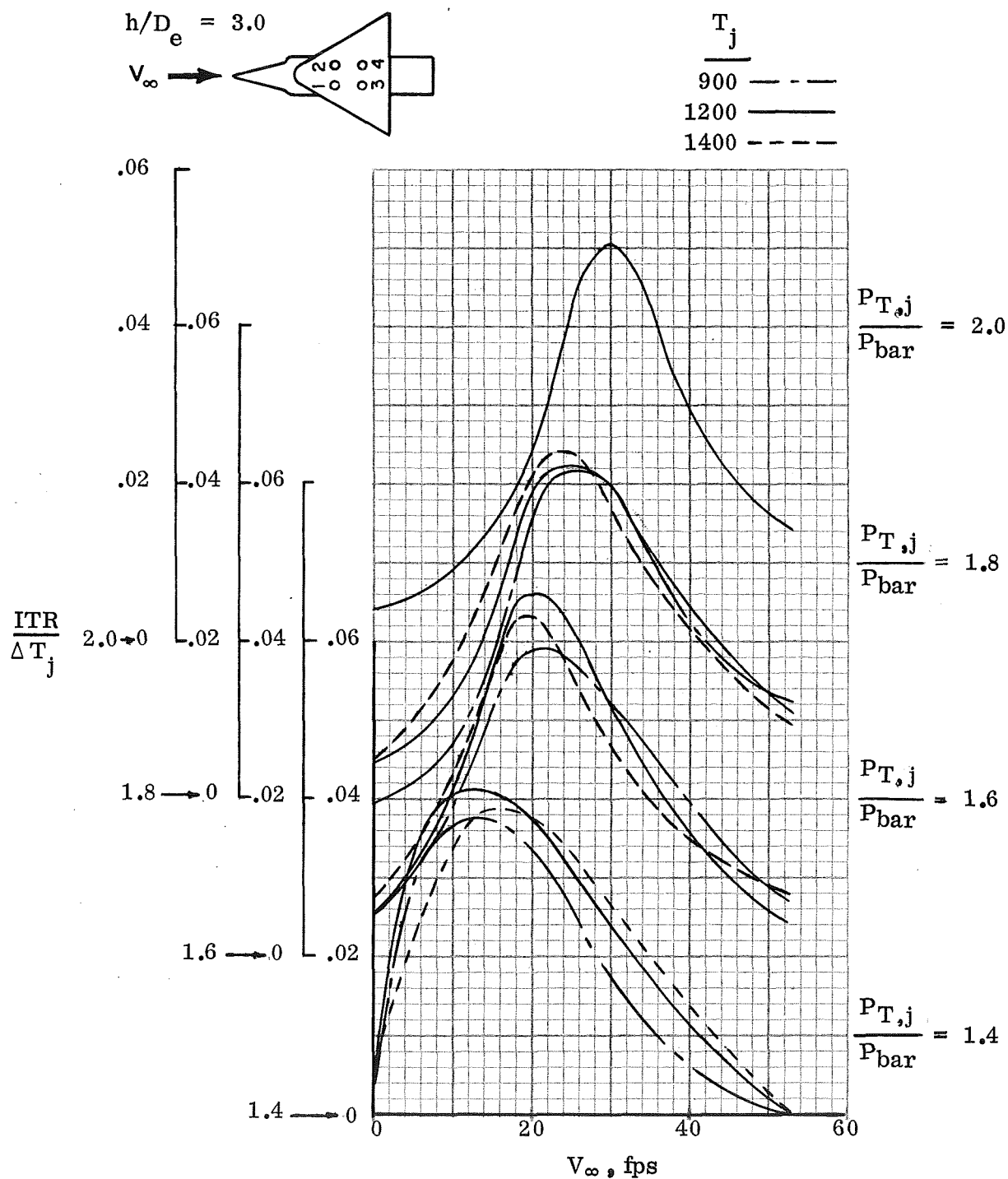
(a) Average of Inlets 1 and 2

Figure 28. – Effect of Normalizing ITR to ΔT_j, Top Inlets Configuration

69

(b) Average of Inlets 3 and 4
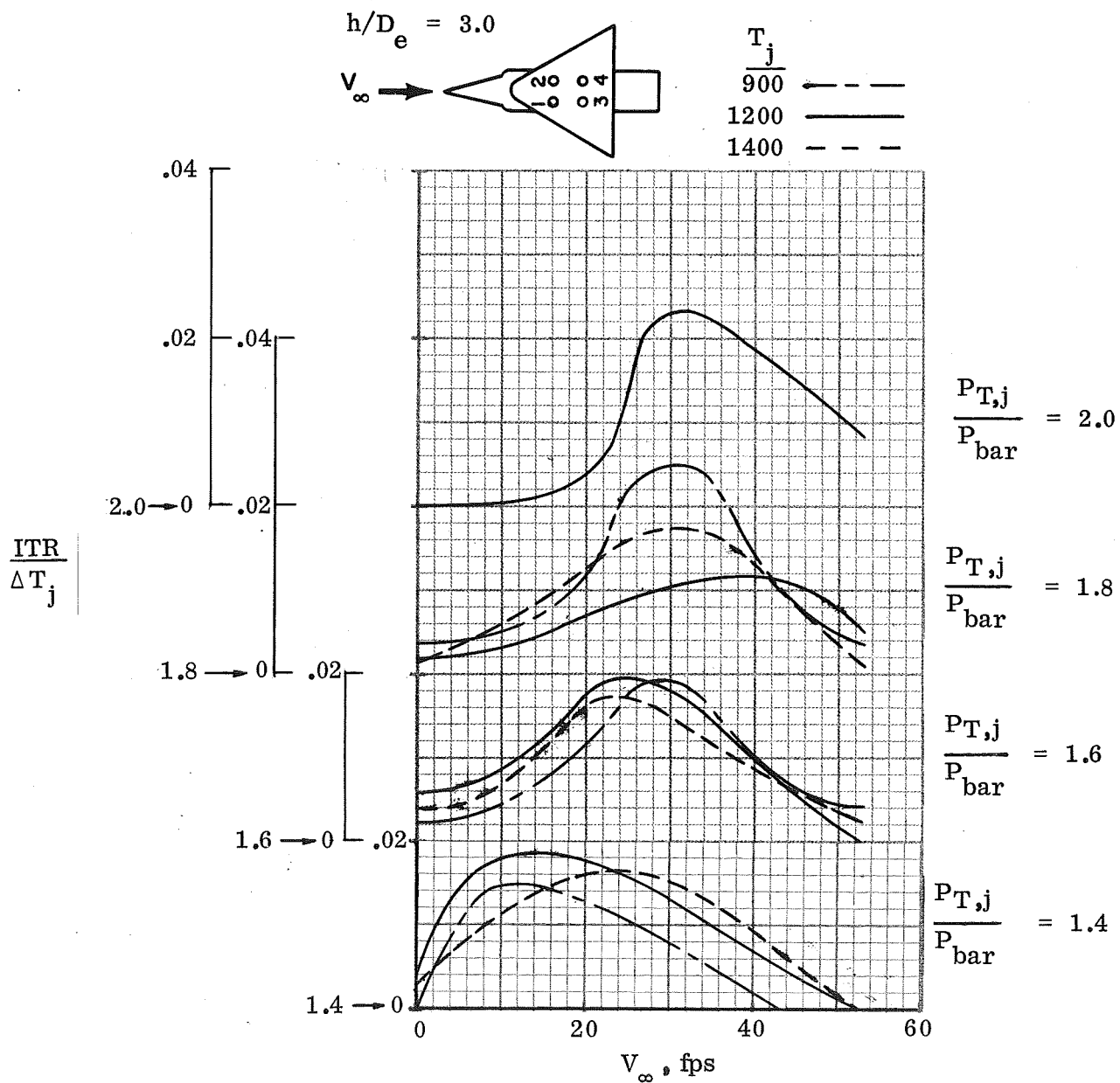
Figure 28 . – Concluded.

Note: ITR is average of
Inlets 1 and 2

$h/D_e = 1.2$

V_∞

2

1

$\dfrac{ITR}{\Delta T_j}$

.10

.08

.06

.04

.02

0

.004 .008 .012 .016 .020 .024 .028 .032

$\dfrac{P_{bar}\, V_\infty}{P_{T,j}\, V_j}$

$P_{T,j}/P_{bar}$	
△	1.3
○	1.4
☐	1.6
◇	1.8
△	2.0

Flagged, $T_j = 900°F$
Open, $T_j = 1200°F$
Shaded, $T_j = 1400°F$
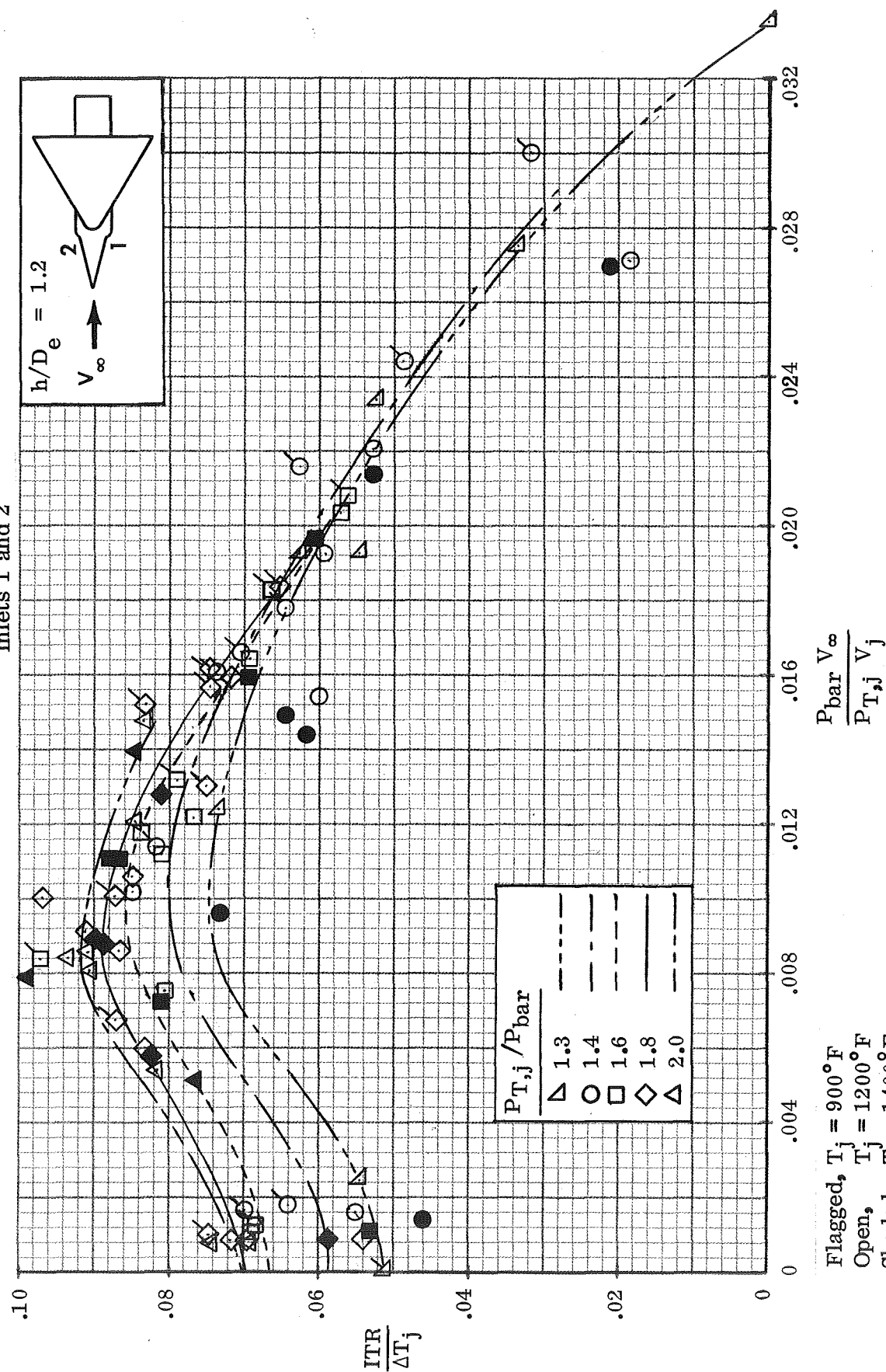
Figure 29. — Correlation of Side Inlets Configuration Data, $\psi = 0°$

71
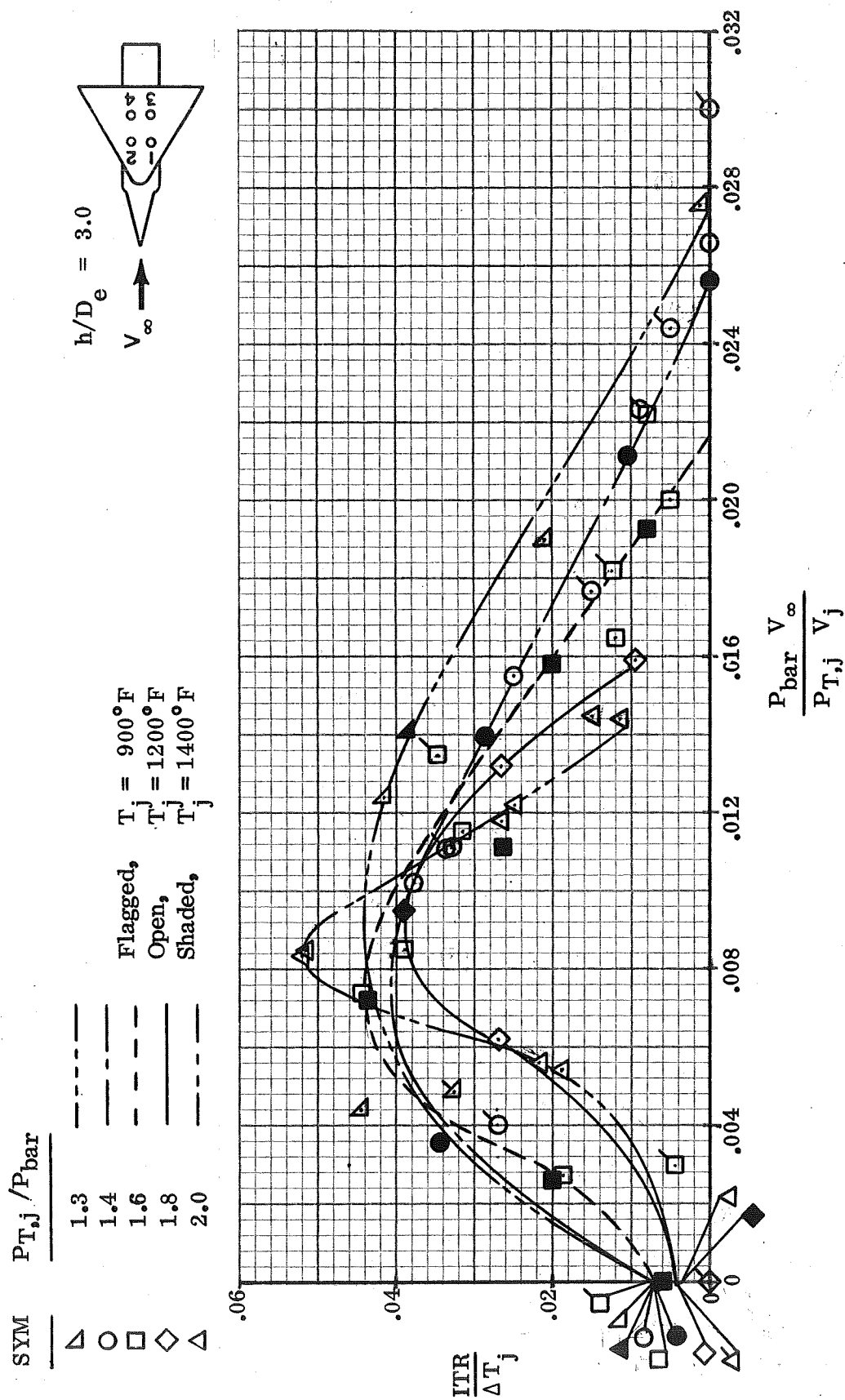
(a) Average of Inlets 1 and 2

Figure 30. – Correlation of Top Inlets Configuration Data, $\psi = 0°$

72
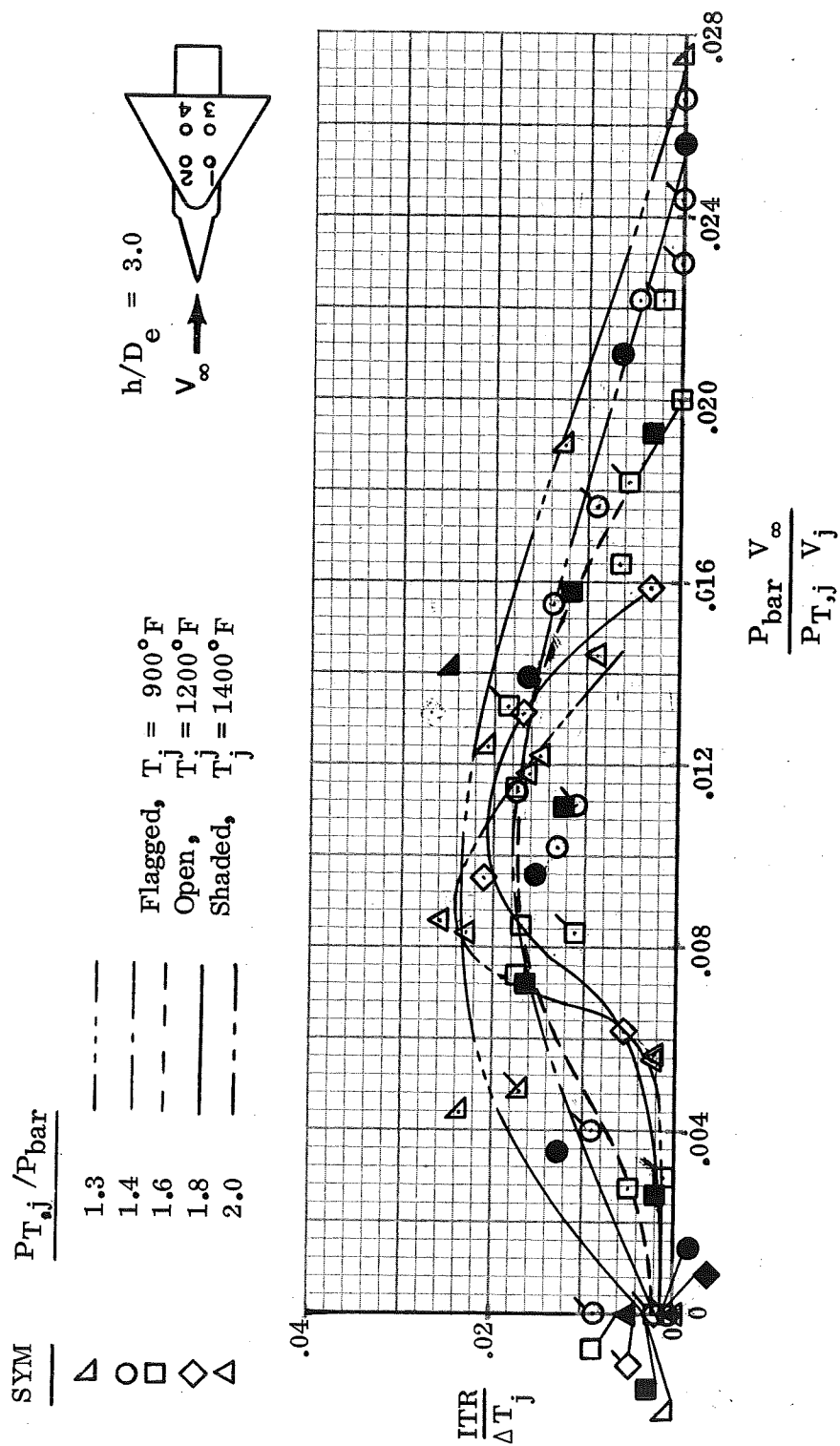
(b) Average of Inlets 3 and 4

Figure 30. – Concluded.
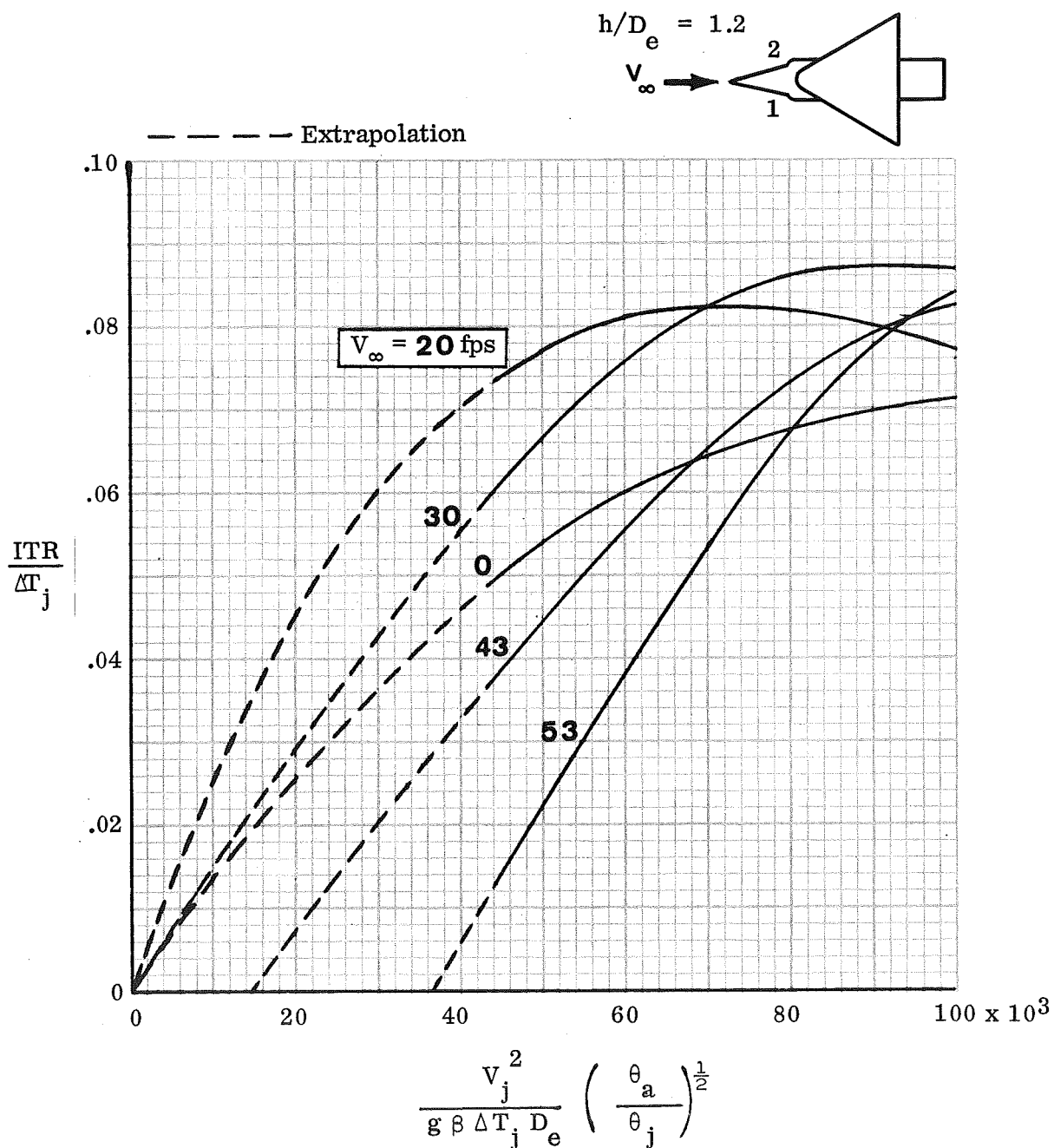
(a) Side Inlets, ITR Average of Inlets 1 and 2

Figure 31. – Variation of Normalized ITR With Buoyancy for Various V_∞ at $\psi = 0°$

(b) Top Inlets, Average of Inlets 1 and 2

$h/D_e = 3.0$

$V_\infty \longrightarrow$

$- - - -$ Extrapolation

$$\frac{V_j^2}{g \, \beta \, \Delta T_j \, D_e} \left(\frac{\theta_a}{\theta_j} \right)^{\frac{1}{2}}$$
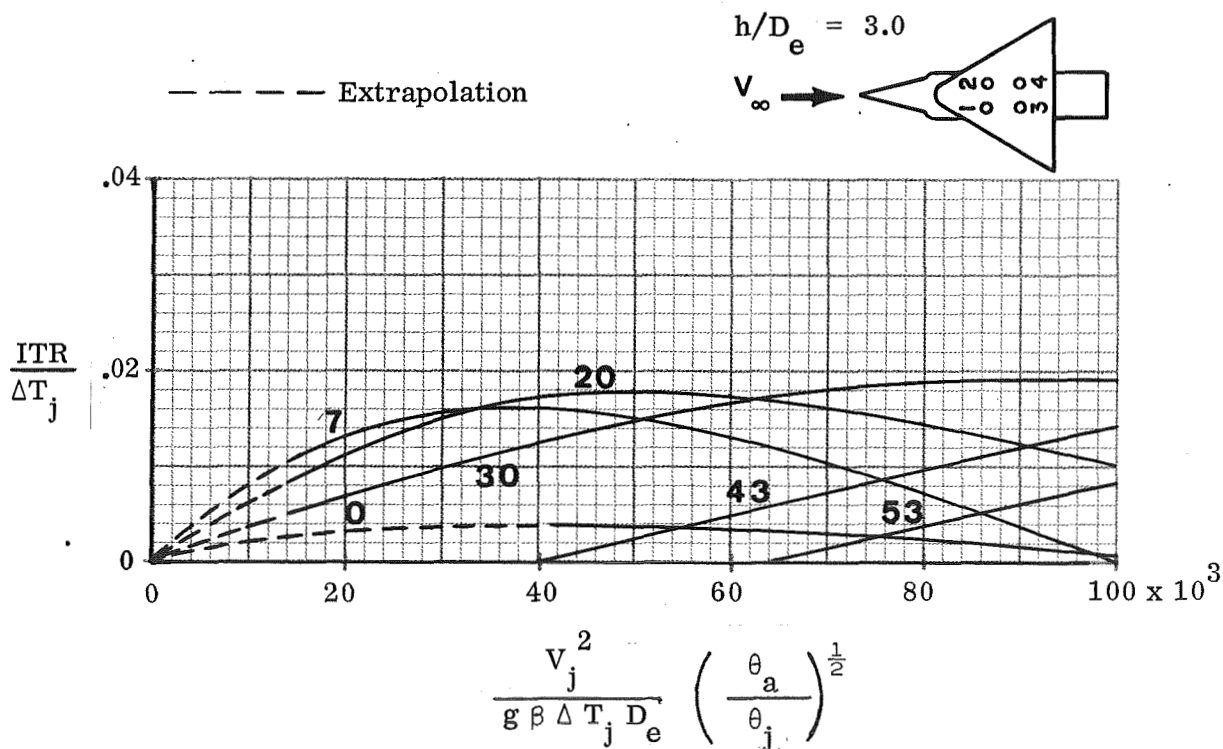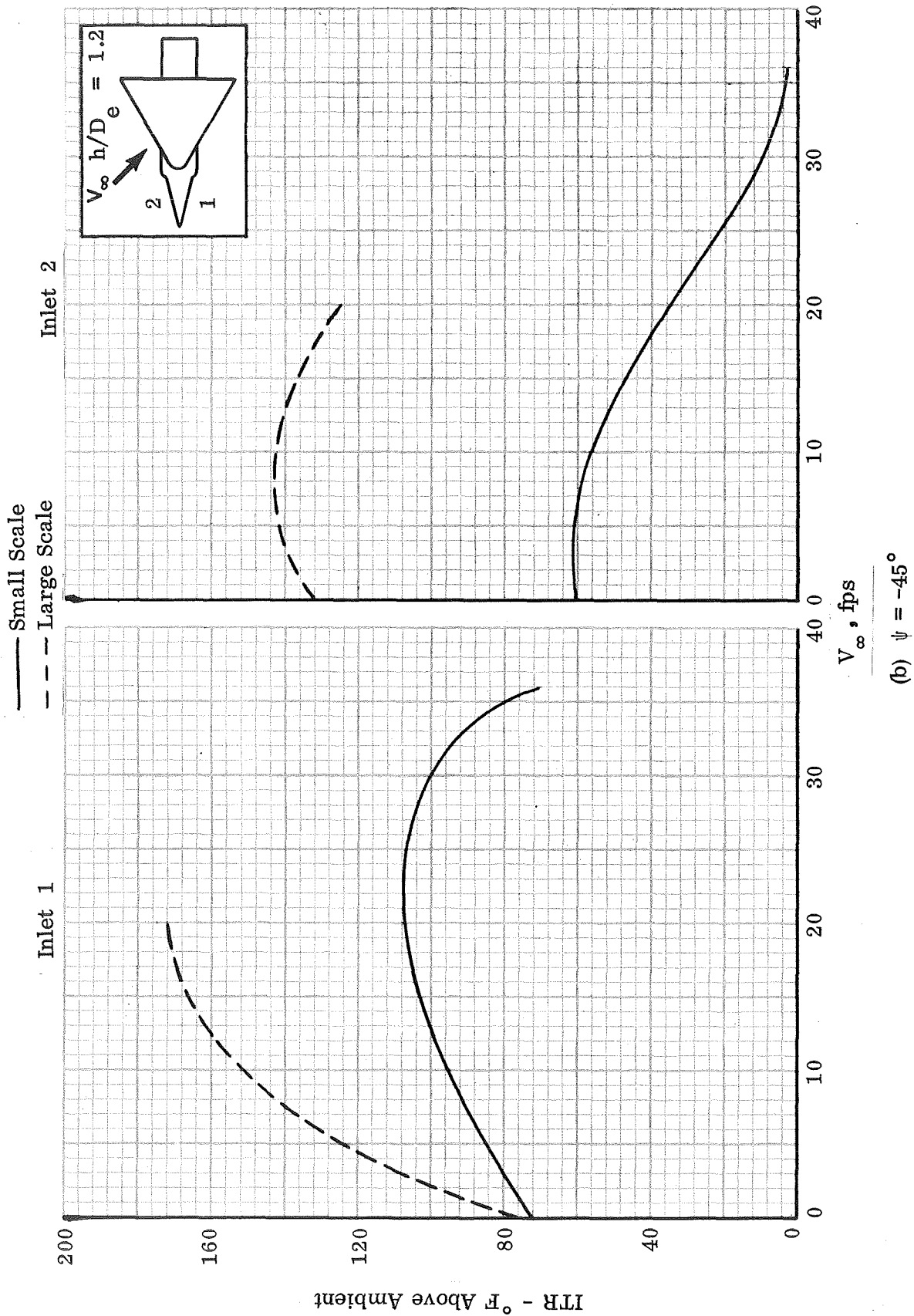
(c) Top Inlets, Average of Inlets 3 and 4

Figure 31. - Concluded.
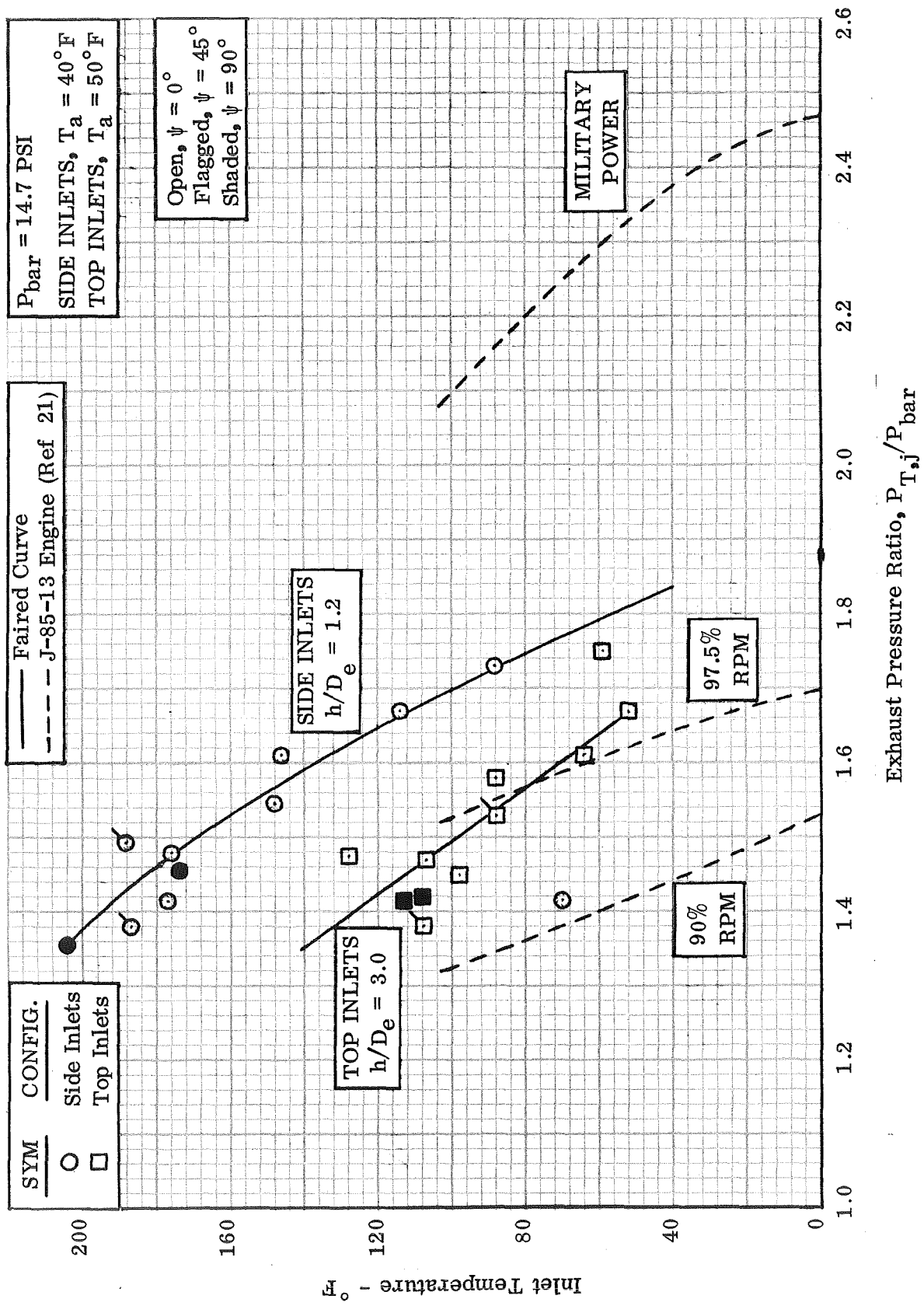
Figure 32. – Large-Scale Model Exhaust Pressure Ratio
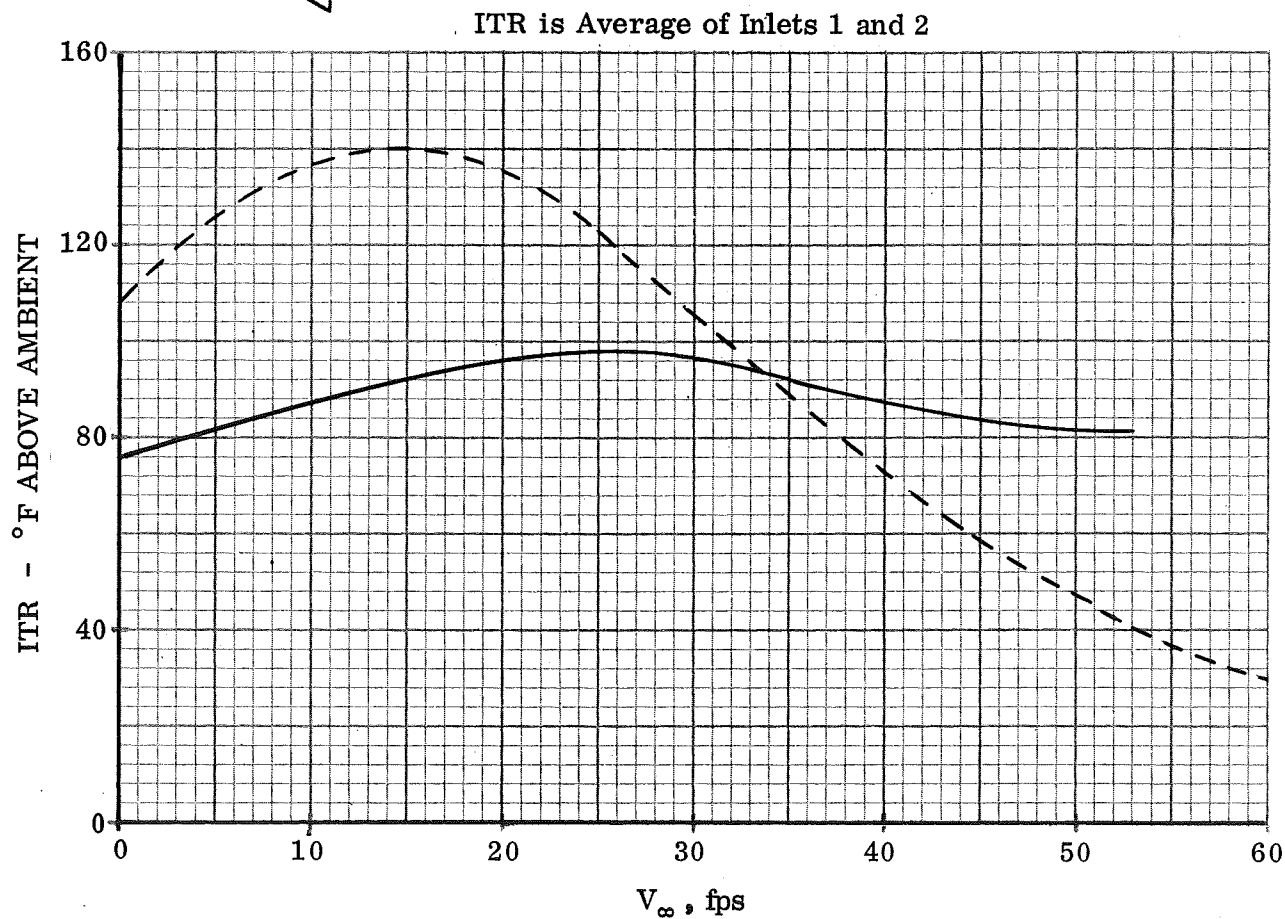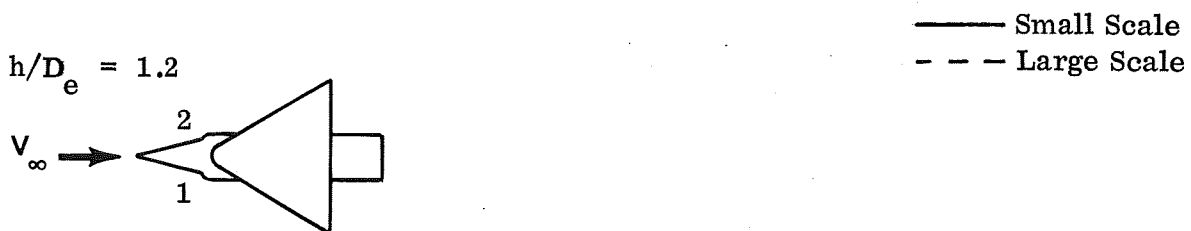
Figure 33. – Comparison of Large and Small Scale ITR vs V_∞ at Equal Exhaust Conditions, Side Inlets Configuration
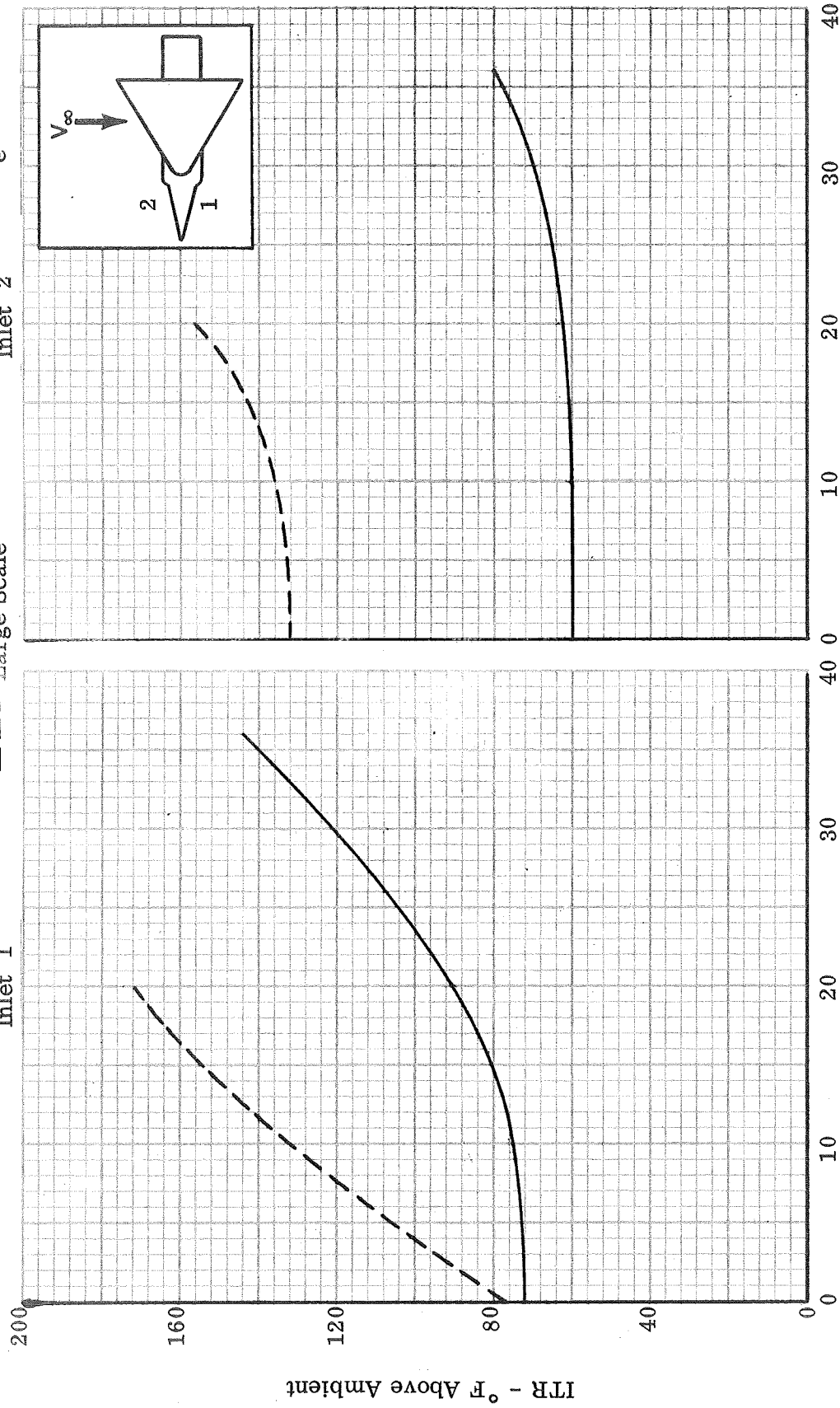
(b) $\psi = -45°$

Figure 33. – Continued.

(c) $\psi = -90°$

Figure 33. - Concluded.
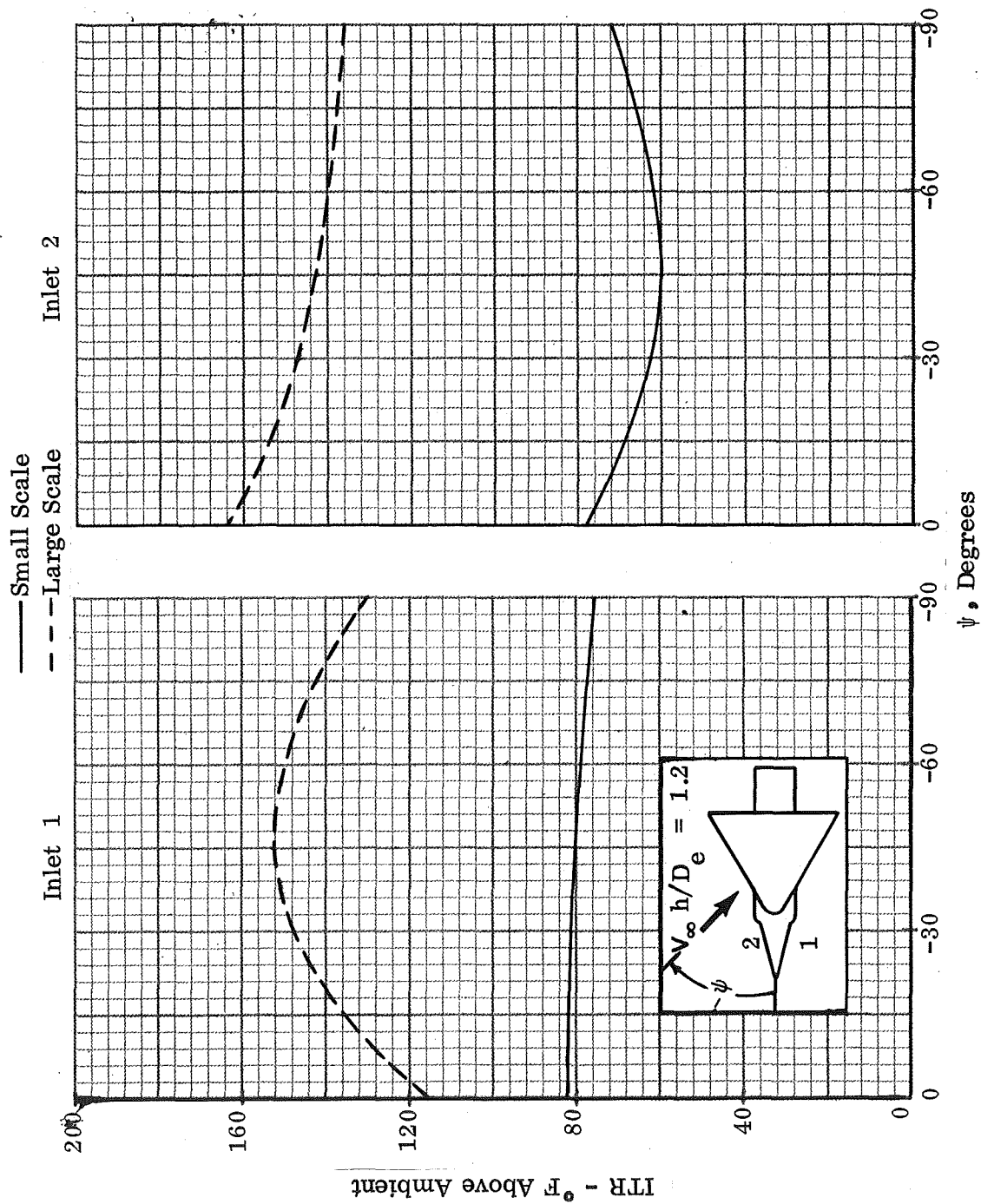
Figure 34. – Comparison of Large and Small Scale ITR vs ψ at Equal Exhaust Conditions, Side Inlets Configuration; $T_j = 1200°F$

(a) $V_\infty = 10$ fps
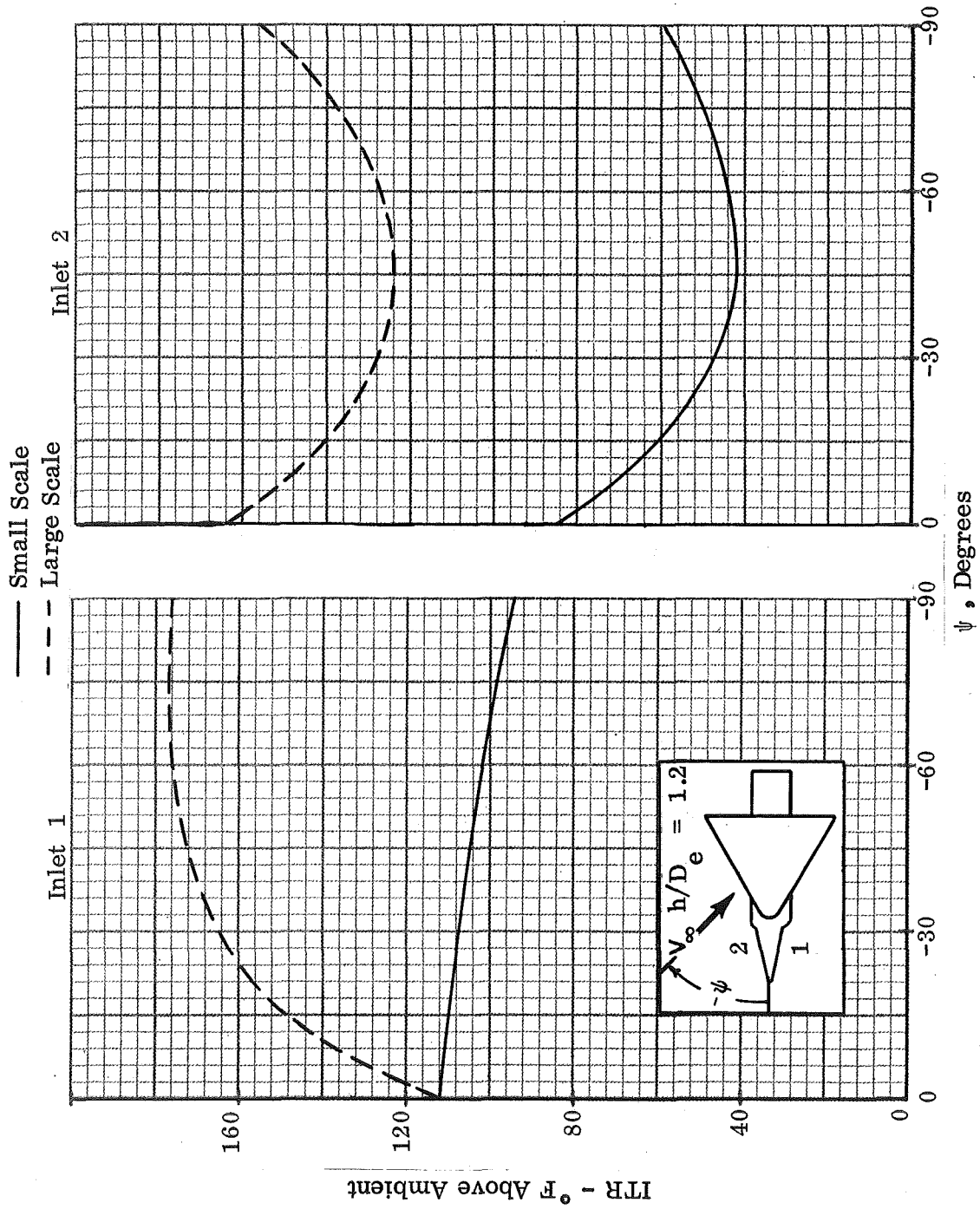
(b) $V_\infty = 20$ fps

Figure 34. – Concluded.

$h/D_e = 1.2$

$V_\infty \rightarrow$

2

1

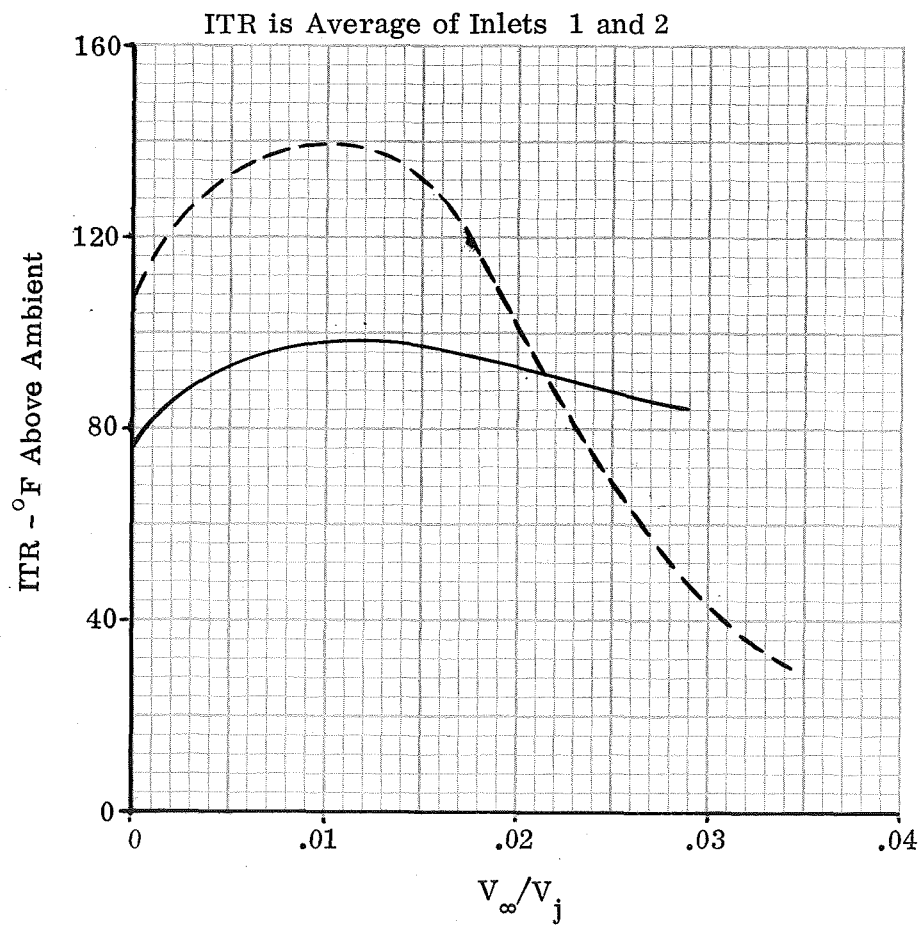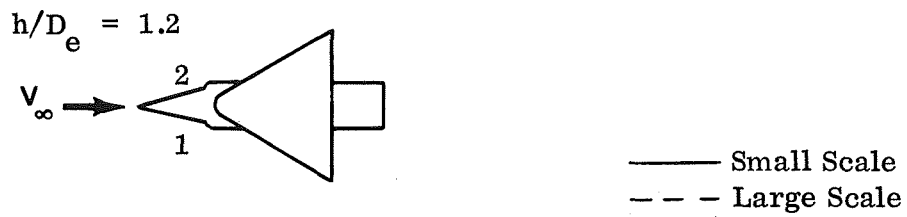—— Small Scale
— — — Large Scale

ITR is Average of Inlets 1 and 2

(a) $\psi = 0°$

Figure 35. – Comparison of Large and Small Scale ITR vs V_∞/V_j at Equal Exhaust Conditions, Side Inlets Configuration, $T_j = 1200°F$

(b) $\psi = -45°$

Figure 35. - Continued.

(c) $\psi = -90°$

Figure 35. – Concluded.
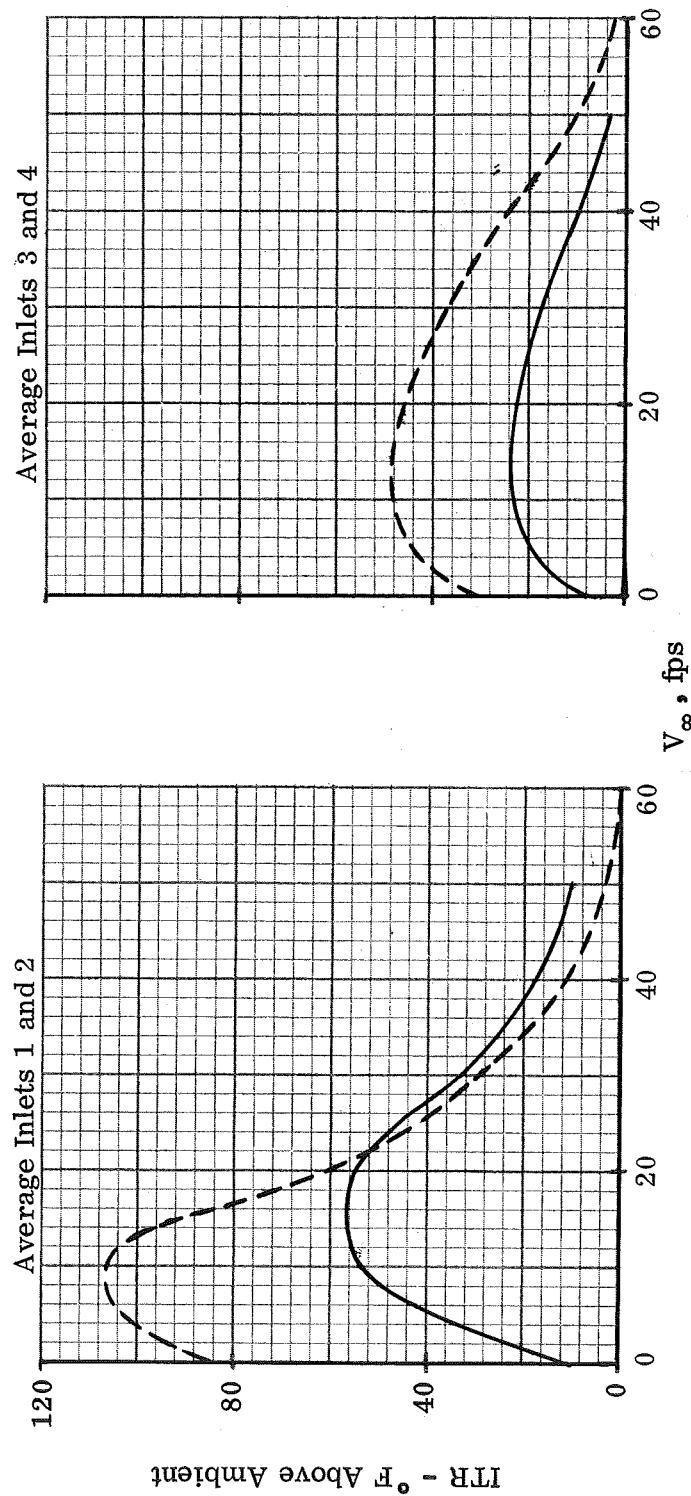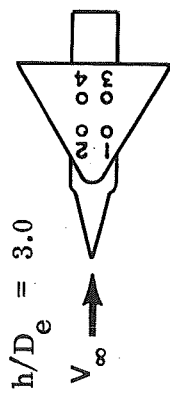
Figure 36. – Comparison of Large and Small Scale ITR vs V_∞ at Equal Exhaust Conditions, Top Inlets Configuration, $T_j = 1200°F$

(a) $\psi = 0°$
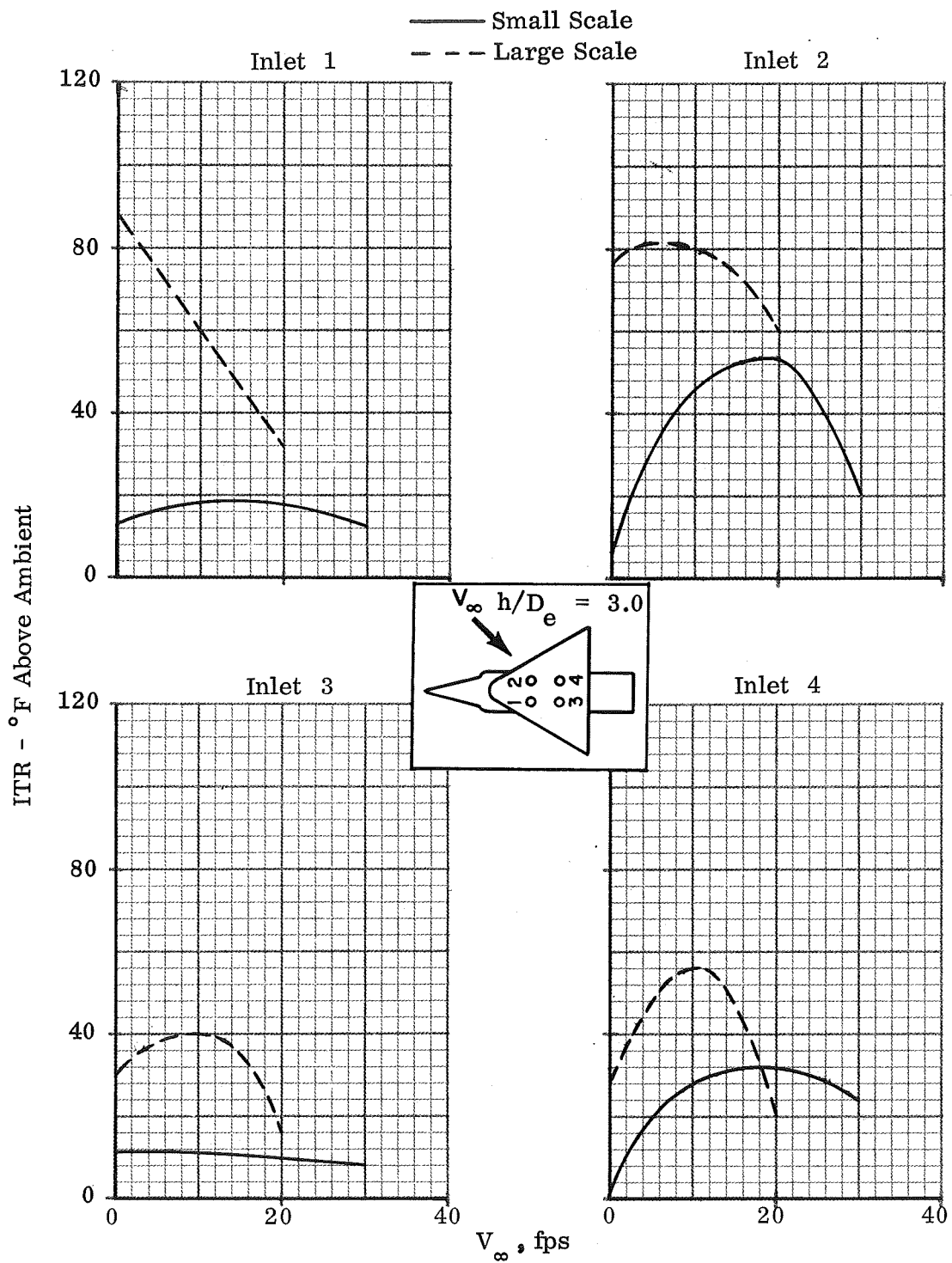
(b) $\psi = -45°$

Figure 36. - Continued.
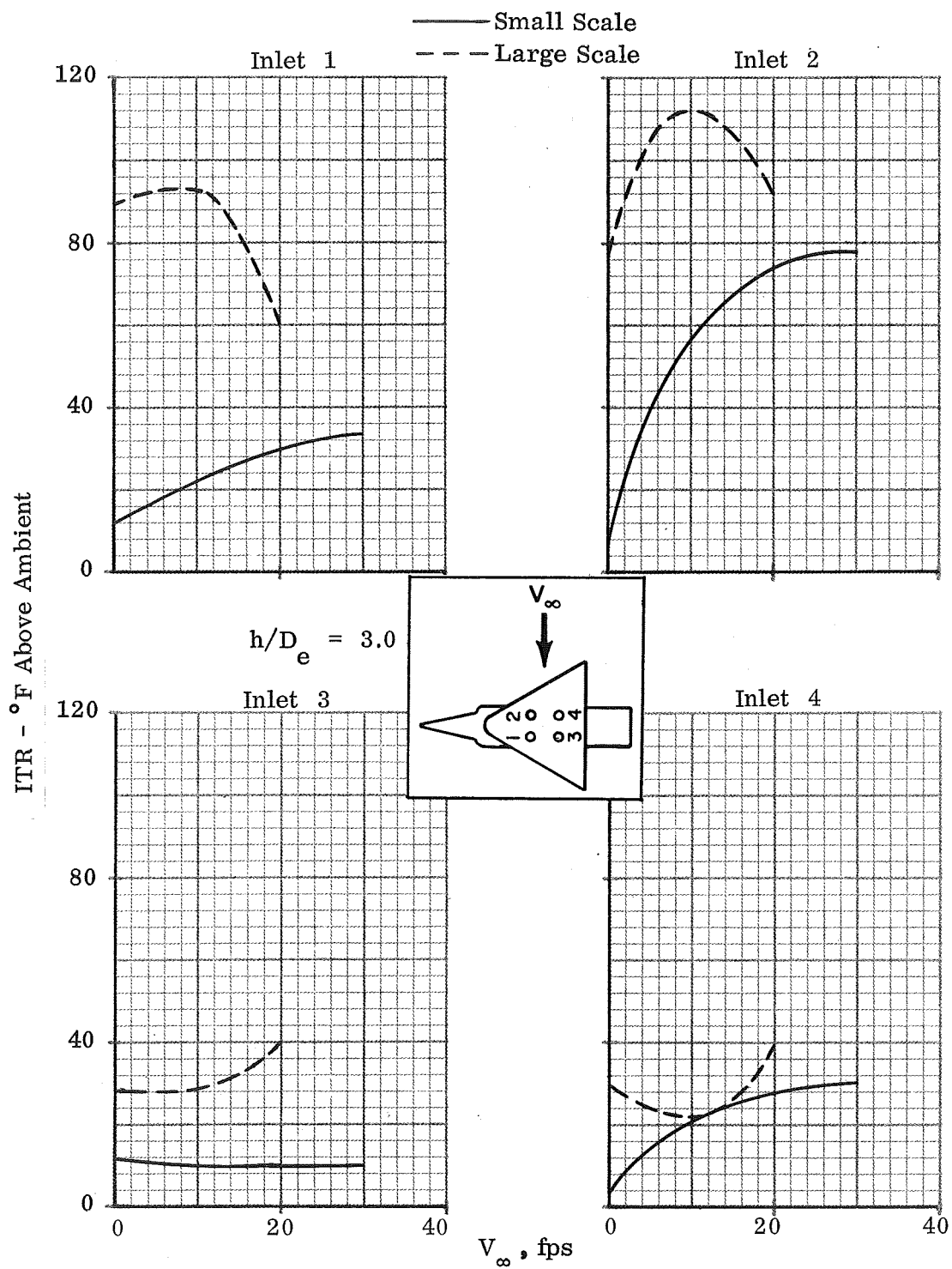
(c) $\psi = -90°$

Figure 36. - Concluded.
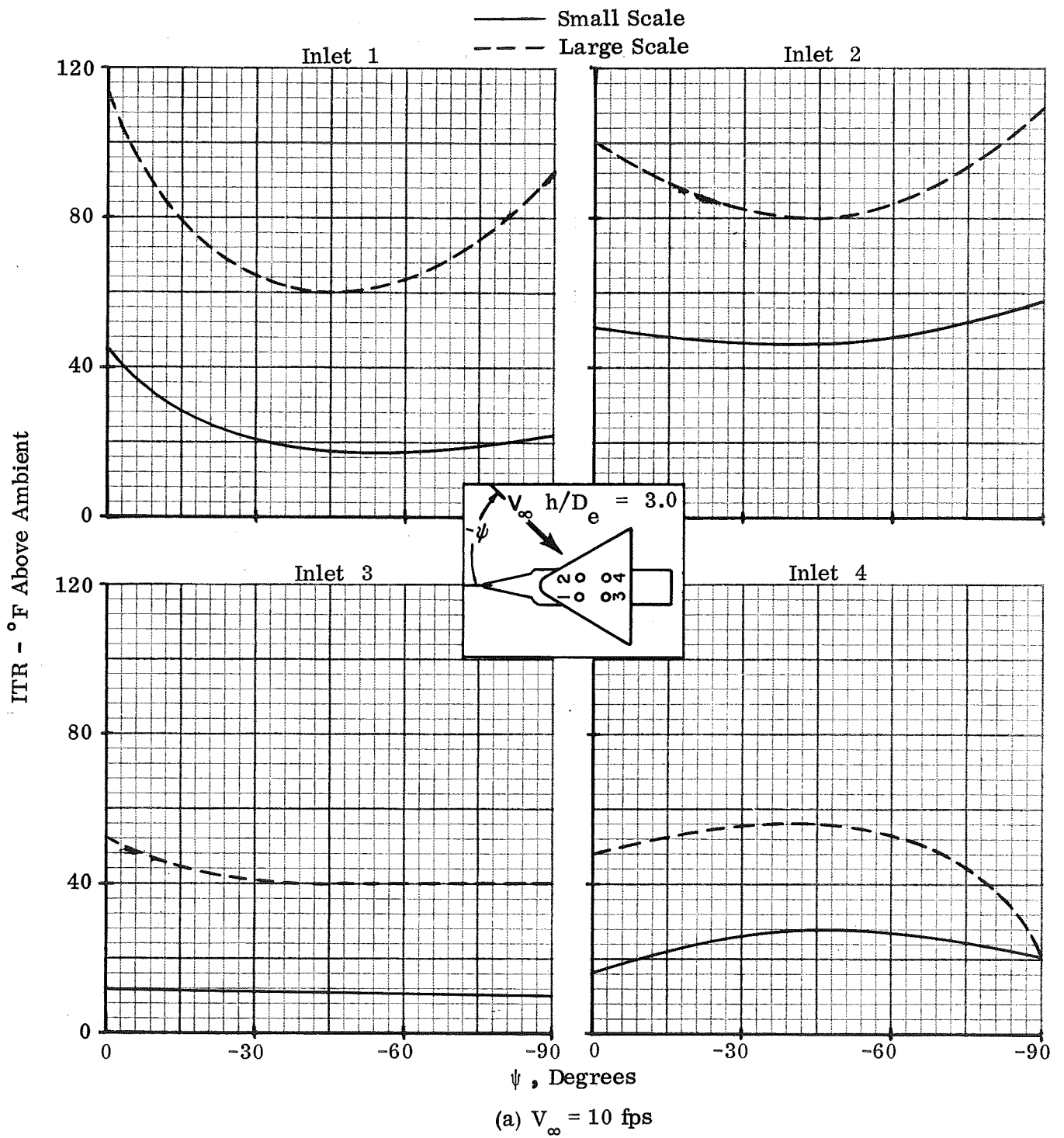
Figure 37. – Comparison of Large and Small Scale ITR vs ψ at Equal Exhaust Conditions, Top Inlets Configuration, $T_j = 1200°F$
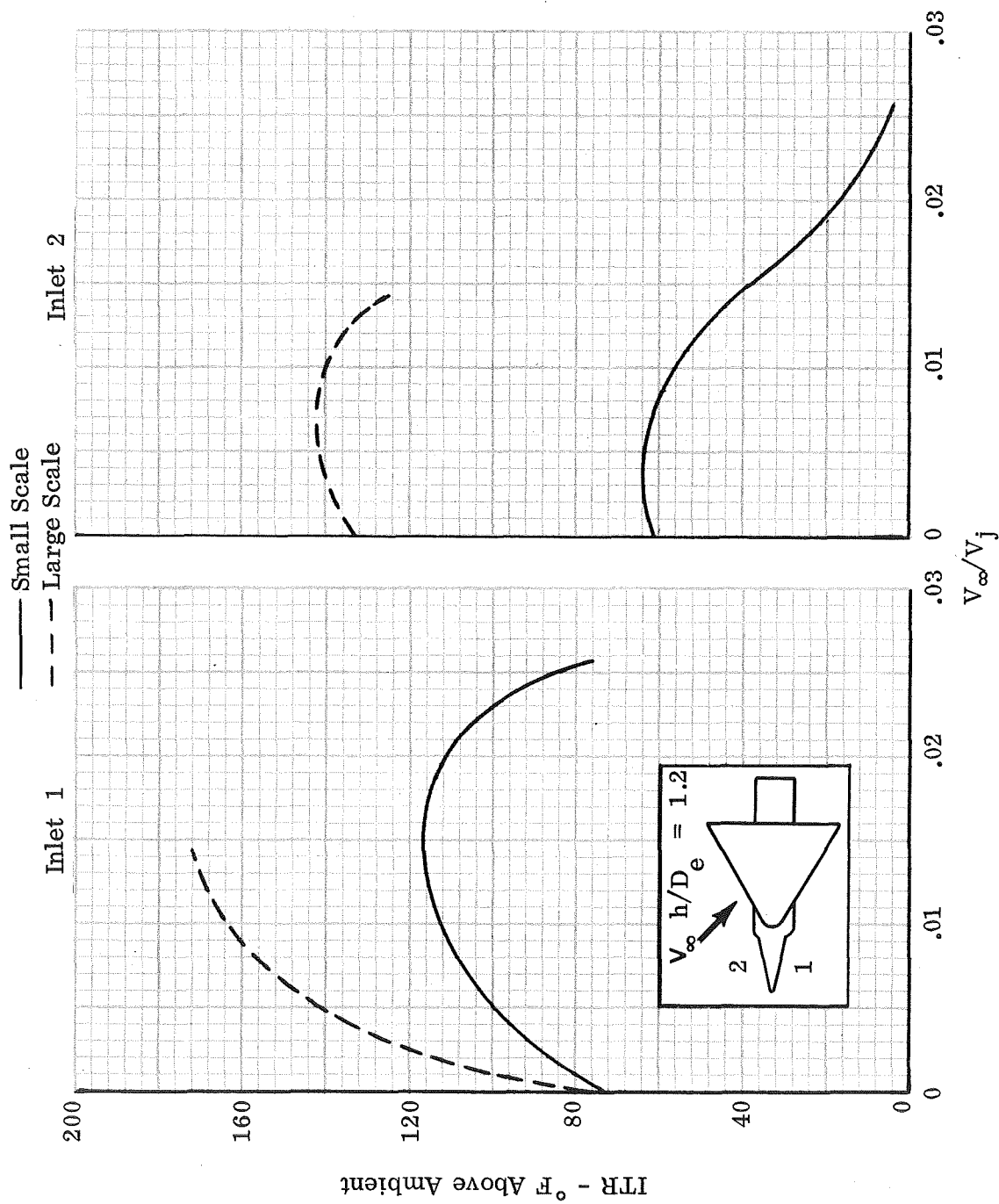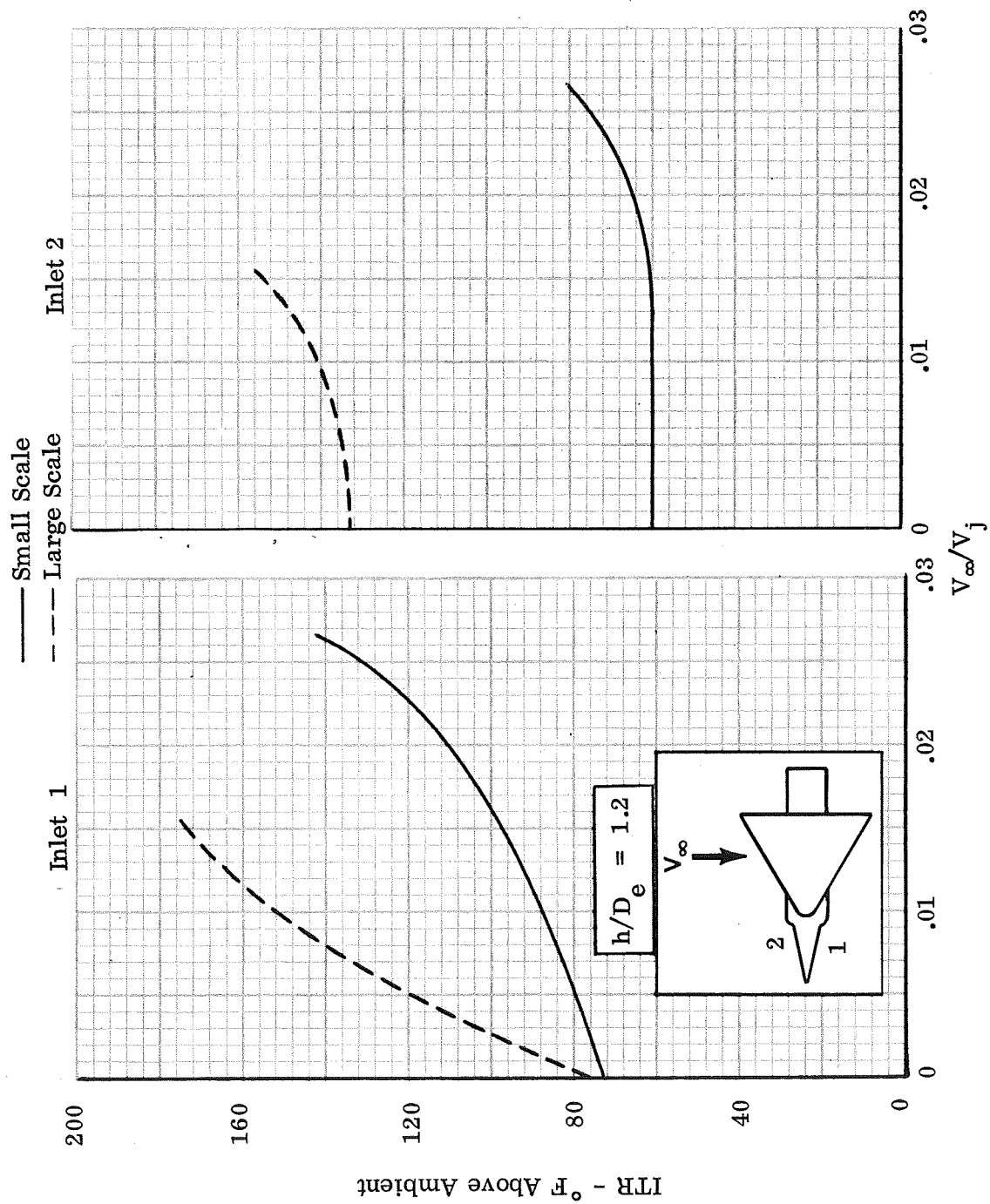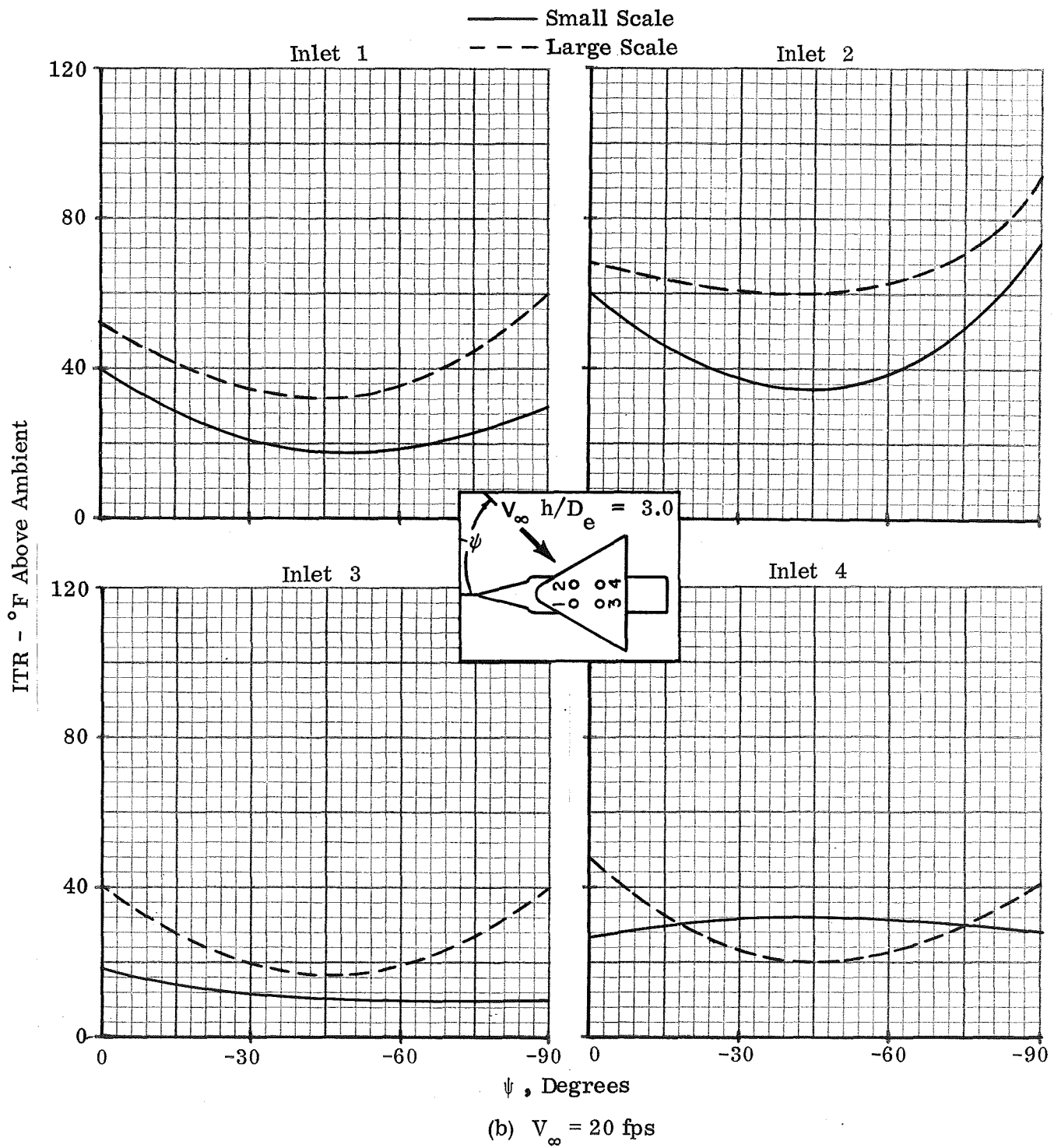
Figure 37. - Concluded.
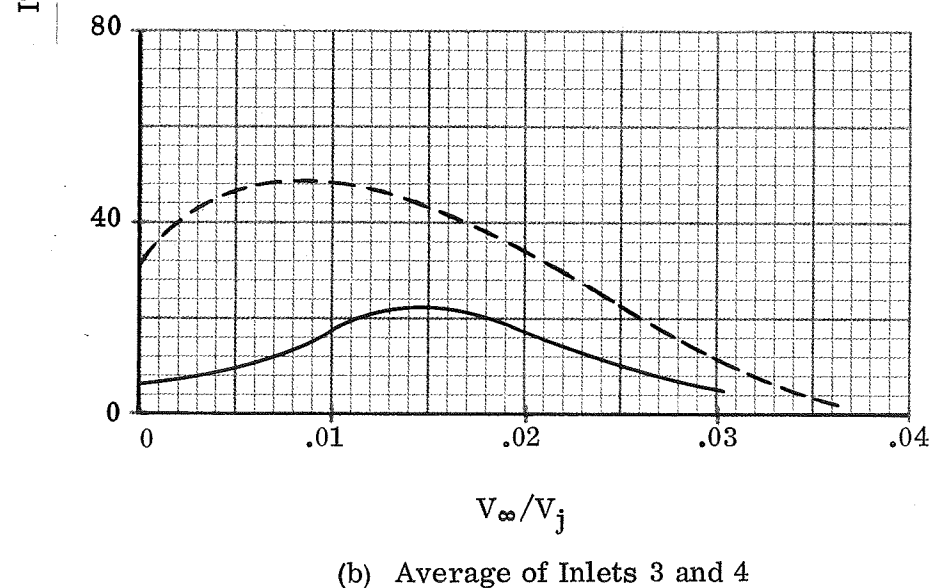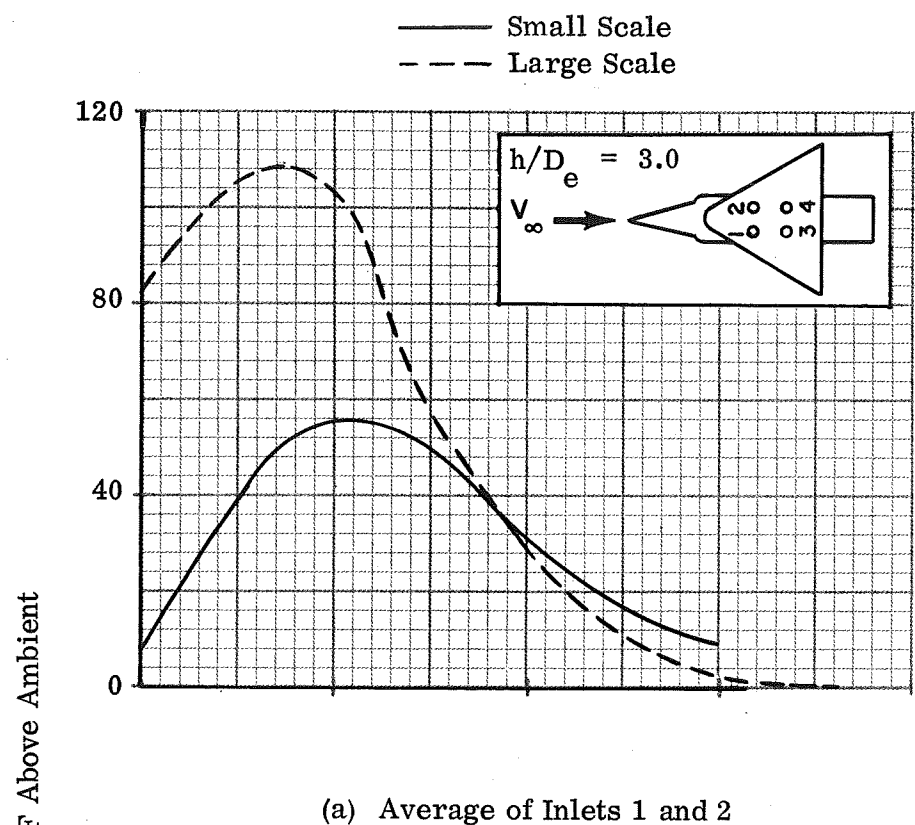
Figure 38. – Comparison of Large and Small Scale ITR vs V_∞/V_j at Equal Exhaust Conditions, Top Inlets Configuration, $\psi = 0°$

————— Side Inlets (Av 1 and 2) $,h/D_e = 1.2$
— — — Top Inlets (Av 1 and 2),
—·— Top Inlets (Av 3 and 4) $h/D_e = 3.0$

$T_j = 1200°F, \psi = 0°$
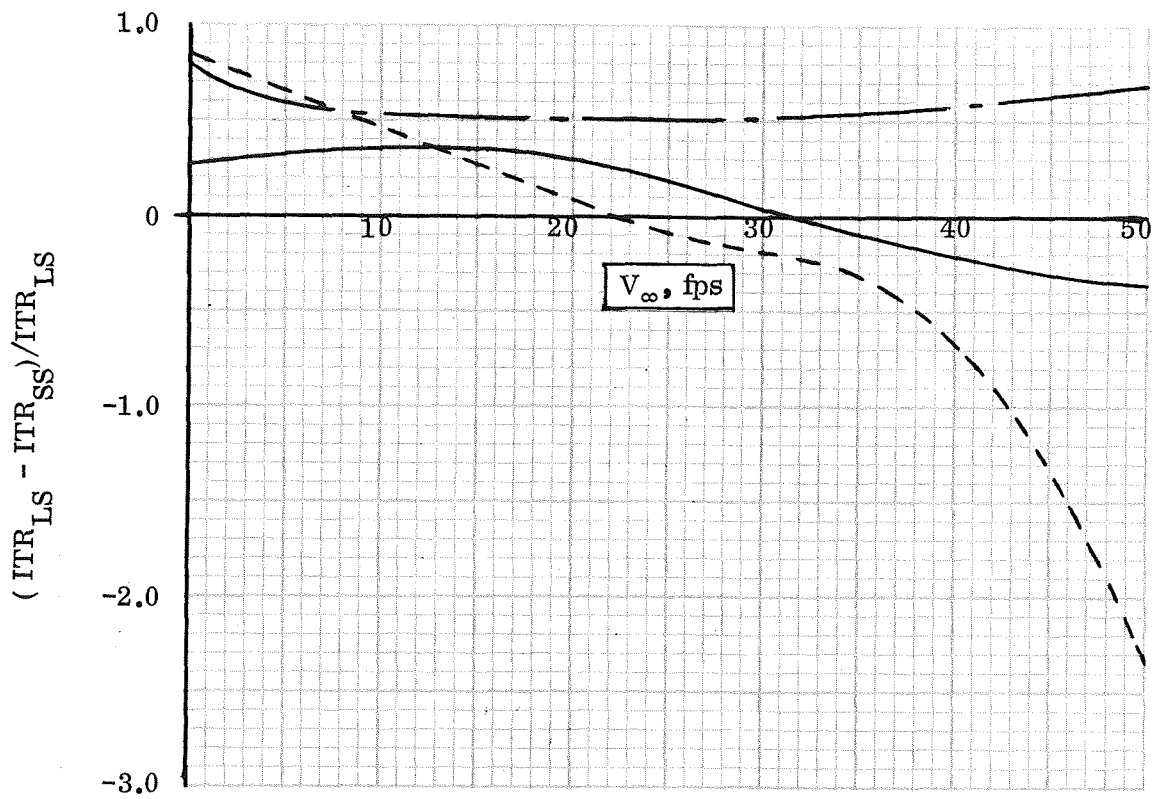
Figure 39. – Summary of Large and Small Scale ITR Compared at Equal Exhaust Conditions

$h/D_e = 1.2$
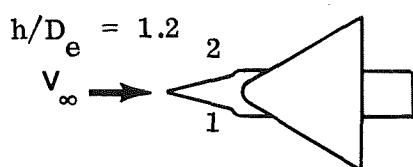
——— Small Scale

— — — Large Scale
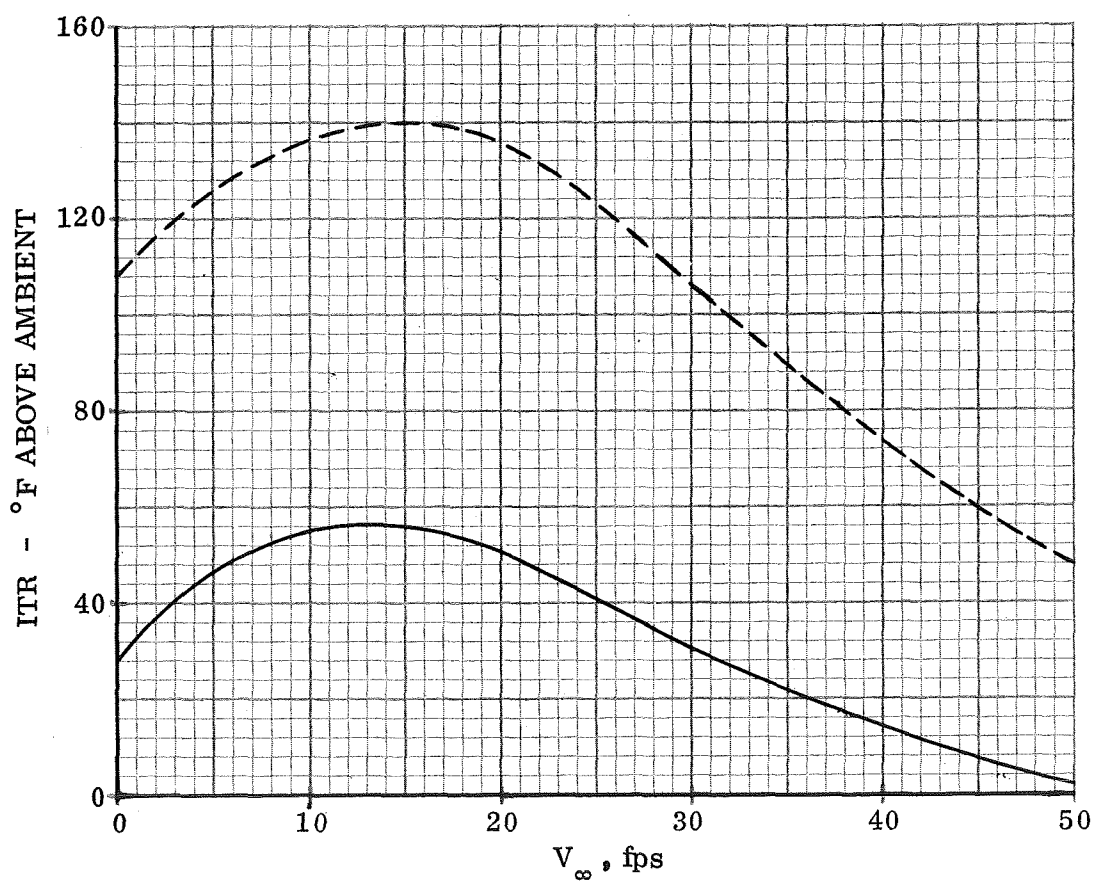
(a) Side Inlets, Average of Inlets 1 and 2

Figure 40. – Comparison of Large and Small Scale ITR vs V_∞

at Equal Buoyancy Conditions, $\psi = 0°$
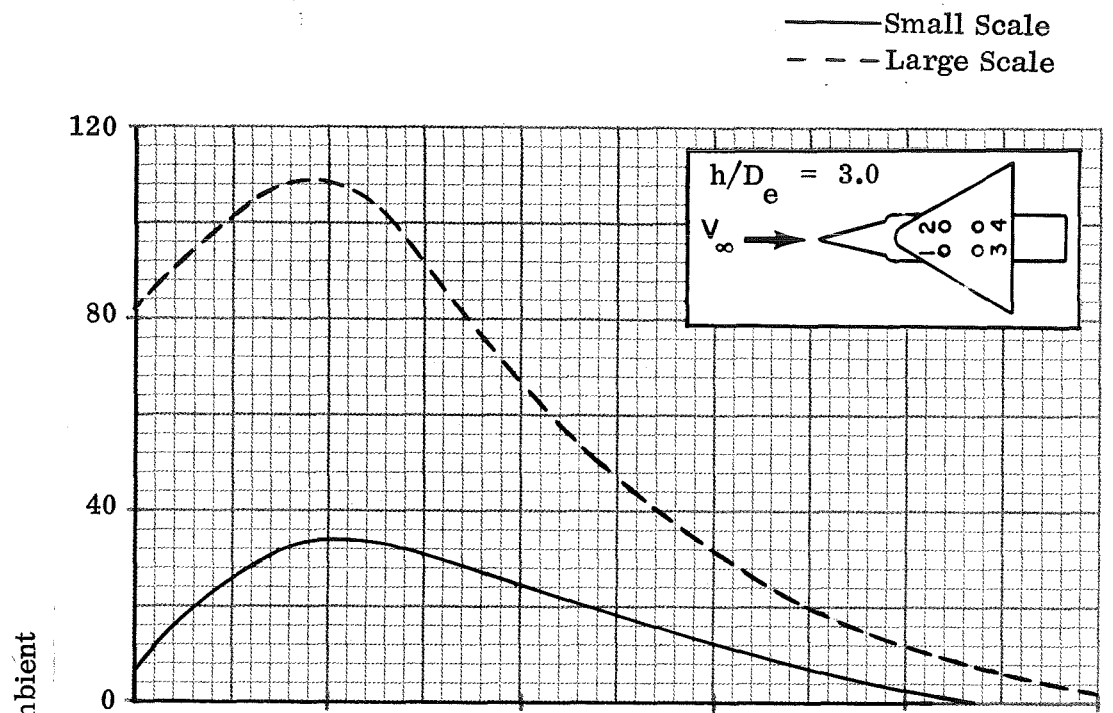
(b) Top Inlets, Average of Inlets 1 and 2
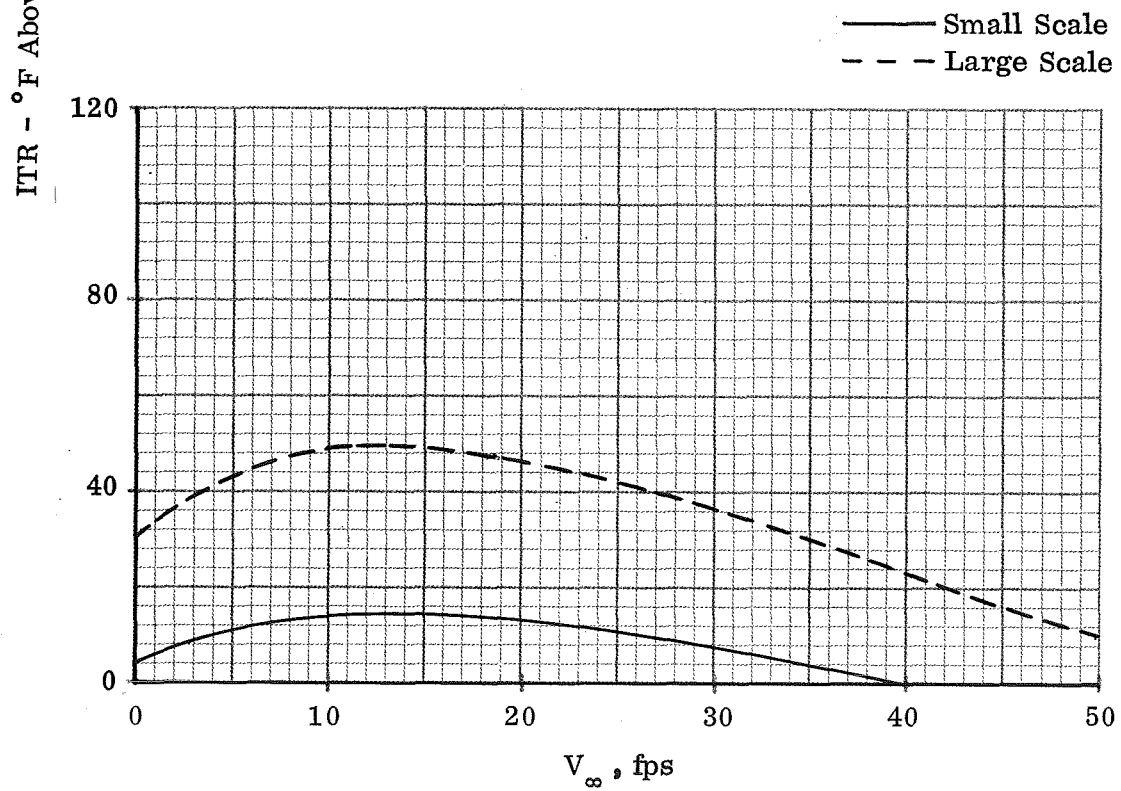
(c) Top Inlets, Average of Inlets 3 and 4

Figure 40. - Concluded.
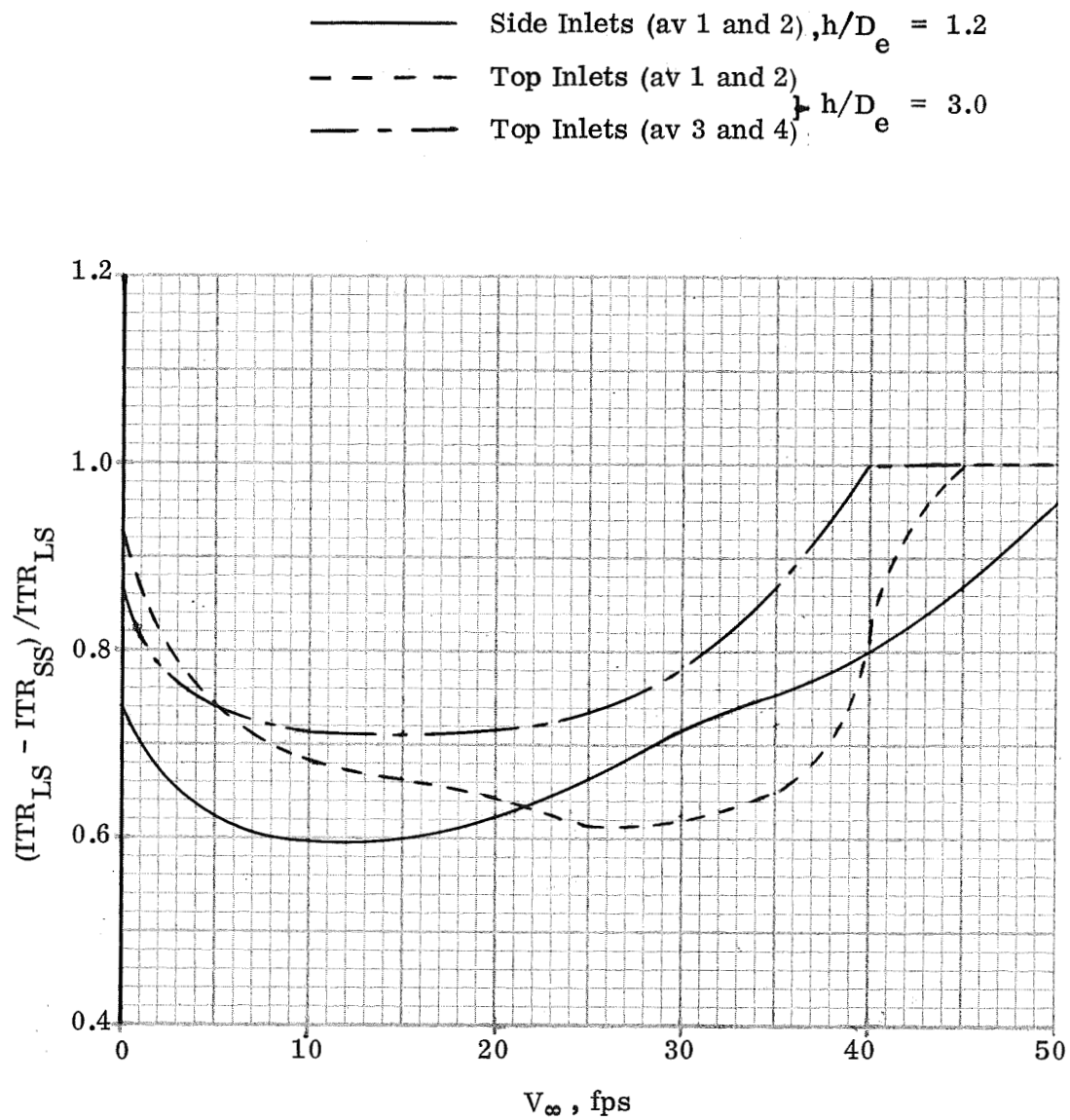
Figure 41. – Summary of Large and Small Scale ITR
Compared at Equal Buoyancy Conditions, $\psi = 0°$.

APPENDIX A

BUOYANCY PARAMETER CORRELATION

The empirical evaluation of candidate dynamic similarity parameters may be accomplished by plotting the dependent variable (in this case $ITR/\Delta T_j$) versus the candidate parameter and examining the results for correlation with the independent variables: V_∞, V_j and T_j. This appendix presents plots of $ITR/\Delta T_j$ versus the buoyancy parameter $(V_j^2/g\,\beta\,\Delta T_j\,D_e)(\theta_a/\theta_j)^{\frac{1}{2}}$ as an example of the method. Since V_∞ does not appear as a factor in the parameter it has been extracted (plots made at constant V_∞) and correlation was sought only on V_j and T_j. Correlation is said to be good if T_j correlates (lines of constant T_j do not appear to be functionally related) and the data scatter is no greater than $ITR/\Delta T_j = \pm 0.006$. This criterion is based on the accuracy of measuring ITR ($\pm 5^\circ$F). Correlation is said to be fair if T_j correlates but the data scatter exceeds $ITR/\Delta T_j = \pm 0.006$, and is poor if T_j does not correlate.

Data for the side inlets configuration are presented in figure A-1. Data for the top inlets configuration are presented in figures A-2 and A-3. It is seen that generally, good to fair correlation was achieved at low V_∞ while the correlation was poor at high $V_\infty$. Since good correlation did not persist over the entire V_∞ range, it was concluded that the candidate parameter was not valid. For the sake of completeness, summary curves are presented in figure 31.

A cursory analysis indicated that correlation was in some cases improved when the term $(\theta_a/\theta_j)^{\frac{1}{2}}$ in the buoyancy parameter was replaced by the forms (θ_a/θ_j) and (θ_j/θ_a). Since correlation was sensitive to this term, further analysis to empirically search for the best form of this term appears warranted.
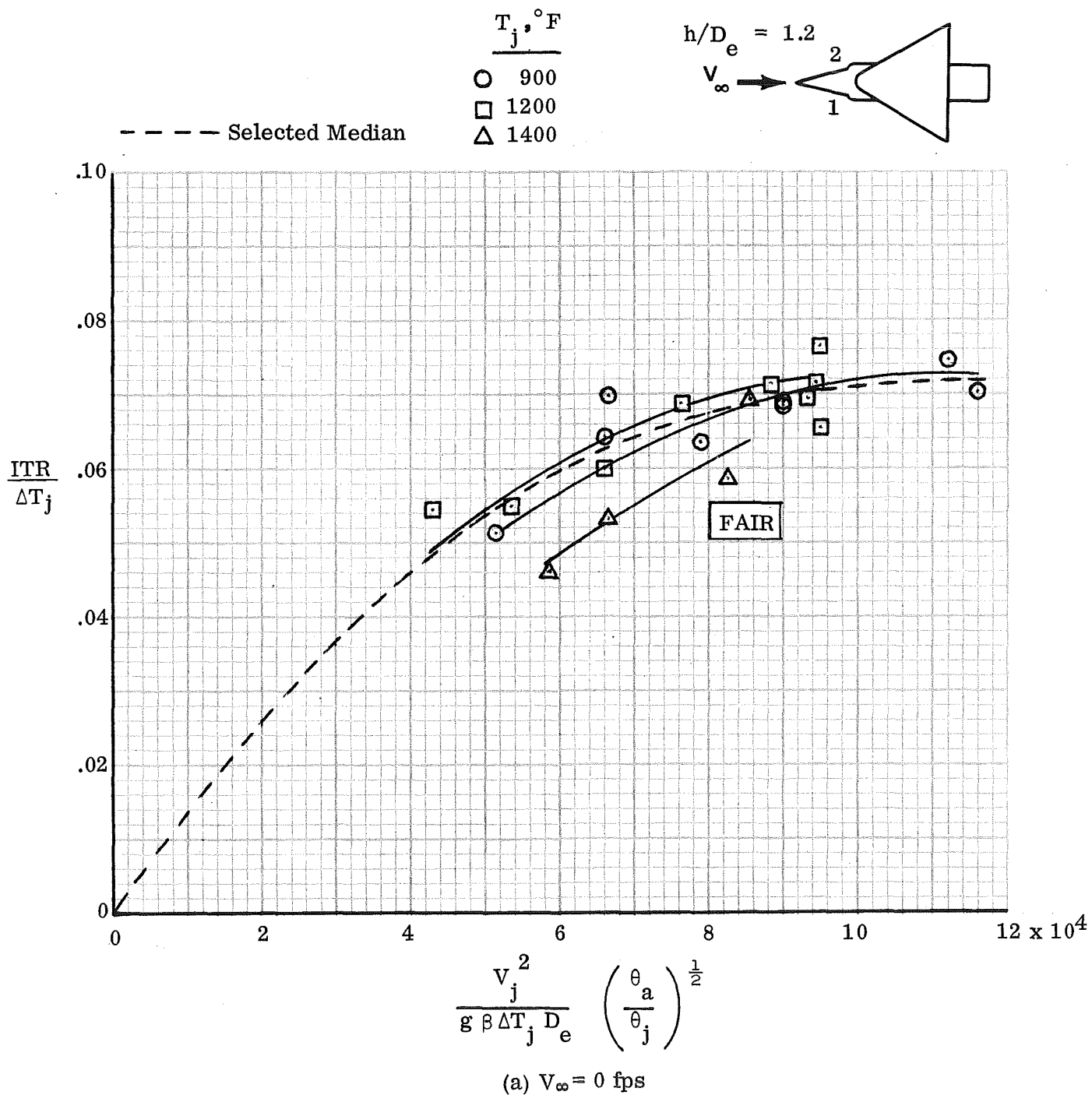
Figure A-1. — Buoyancy Correlation, Side Inlets, Average of Inlets 1 and 2

(b) $V_\infty = 20$ fps

Figure A-1. - Continued

(c) $V_\infty = 30$ fps

Figure A-1. - Continued

(d) $V_\infty = 43$ fps

Figure A-1. - Continued

$$\frac{ITR}{\Delta T_j}$$

$$\frac{V_j^2}{g \beta \Delta T_j D_e} \left(\frac{\theta_a}{\theta_j} \right)^{\frac{1}{2}}$$
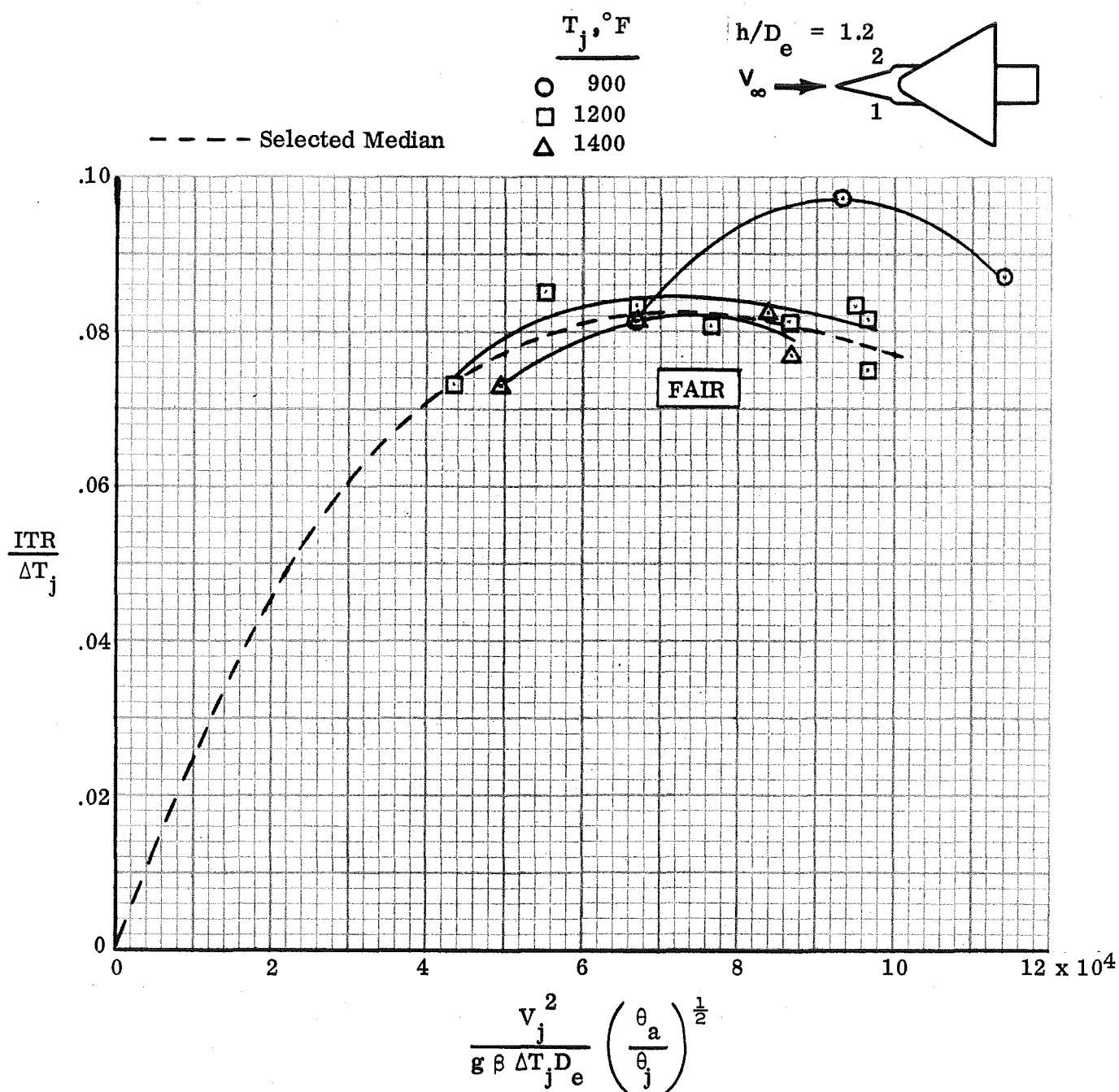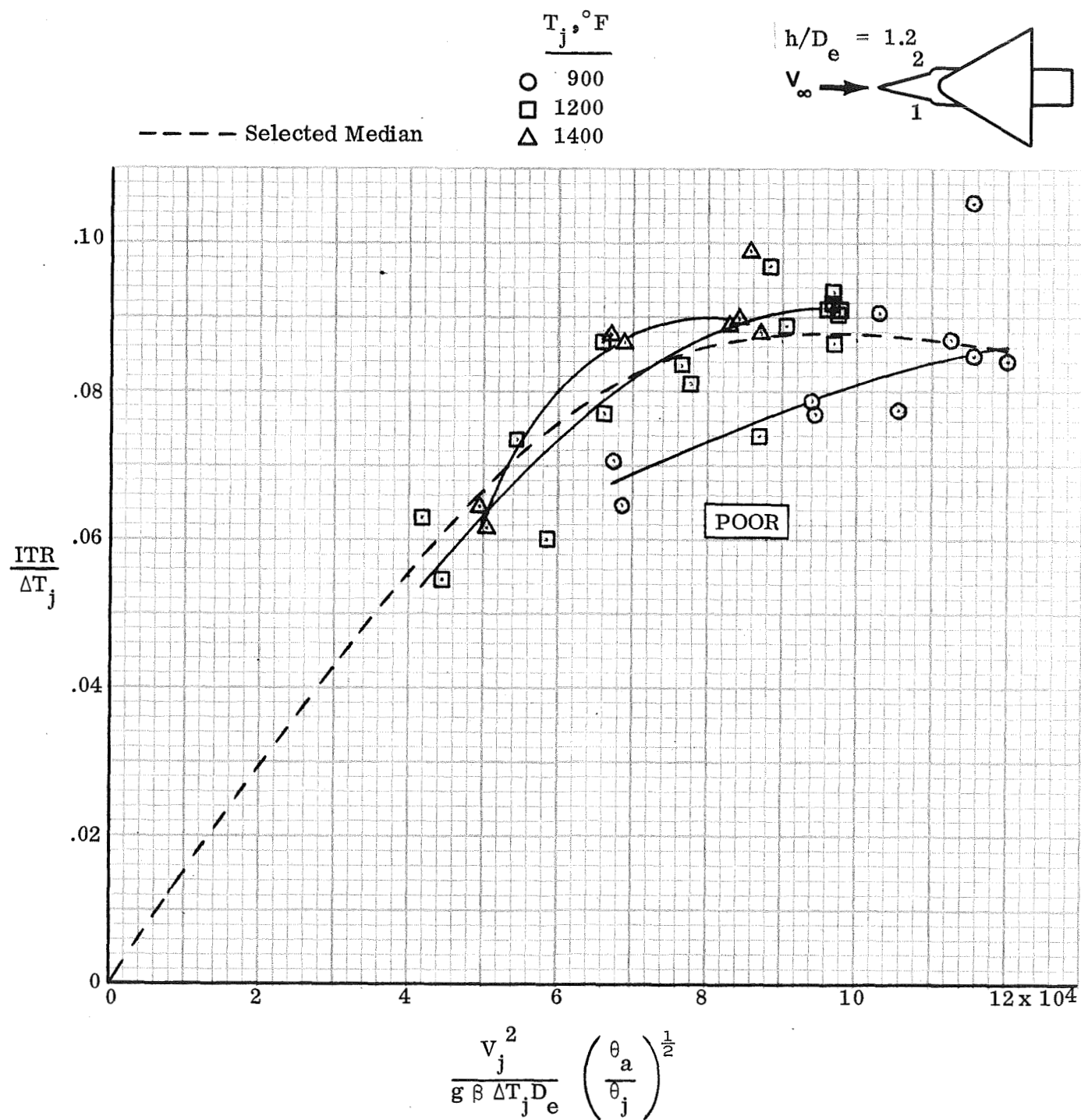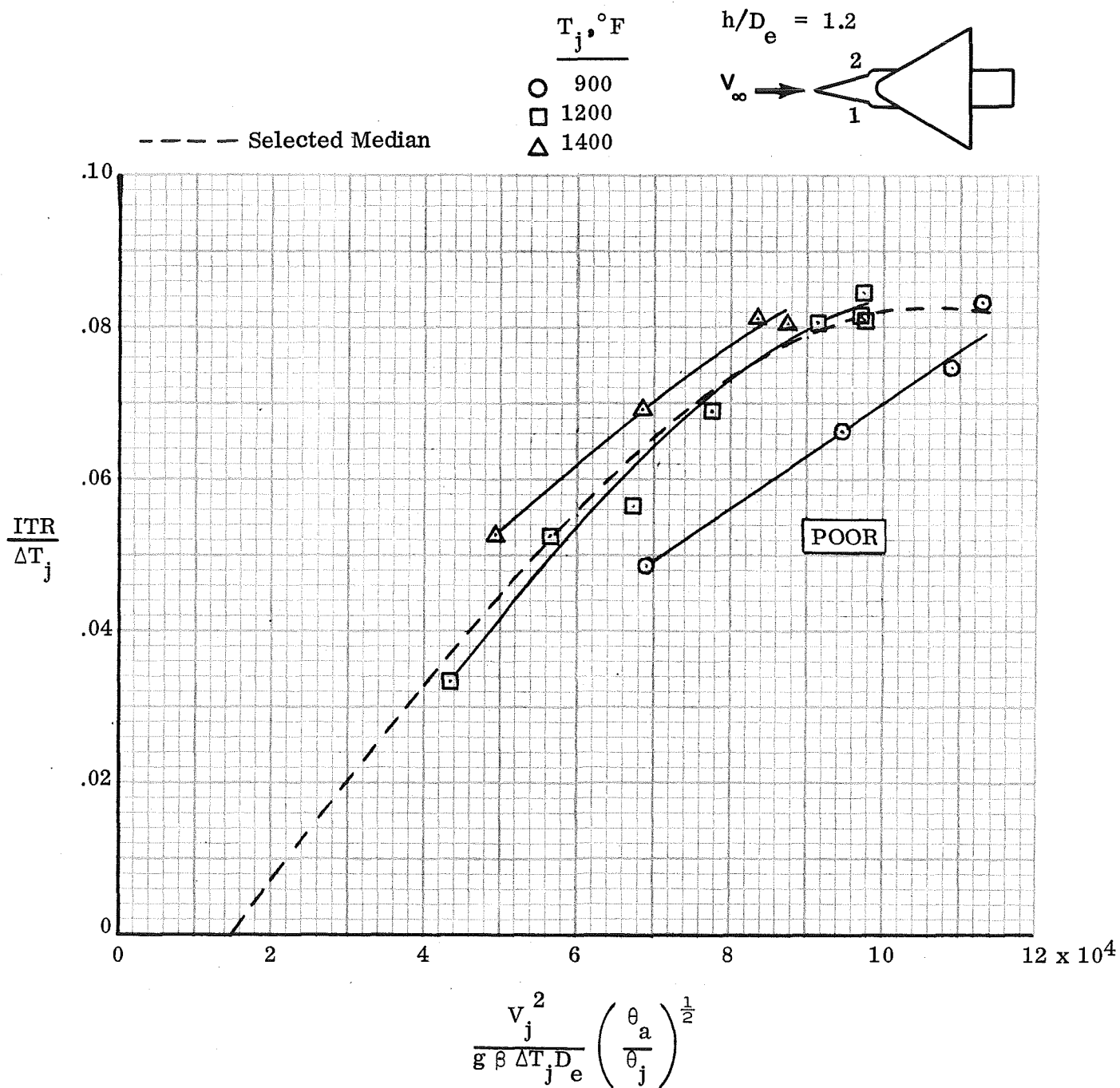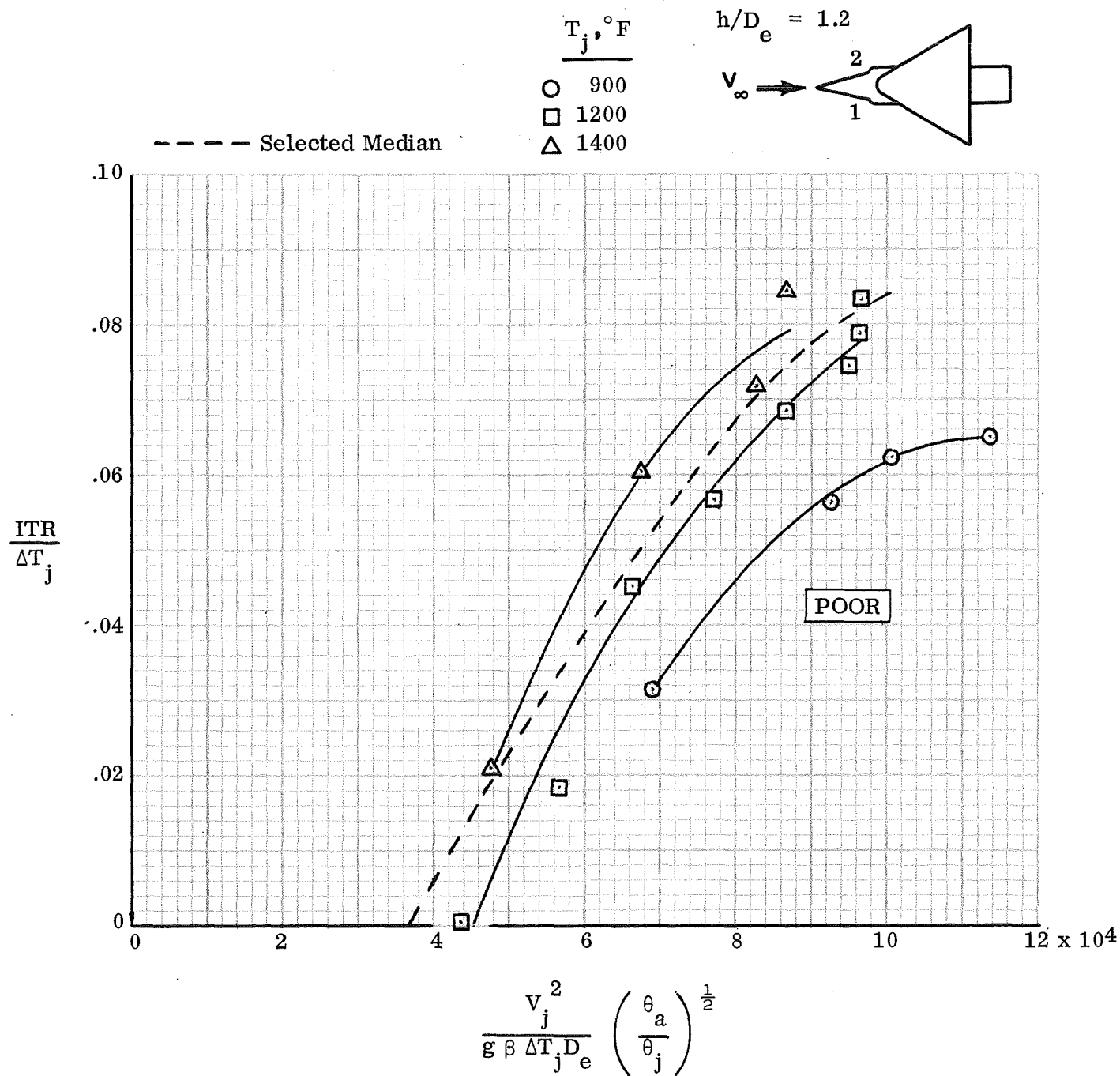
(e) $V_\infty = 53$ fps

Figure A-1. - Concluded
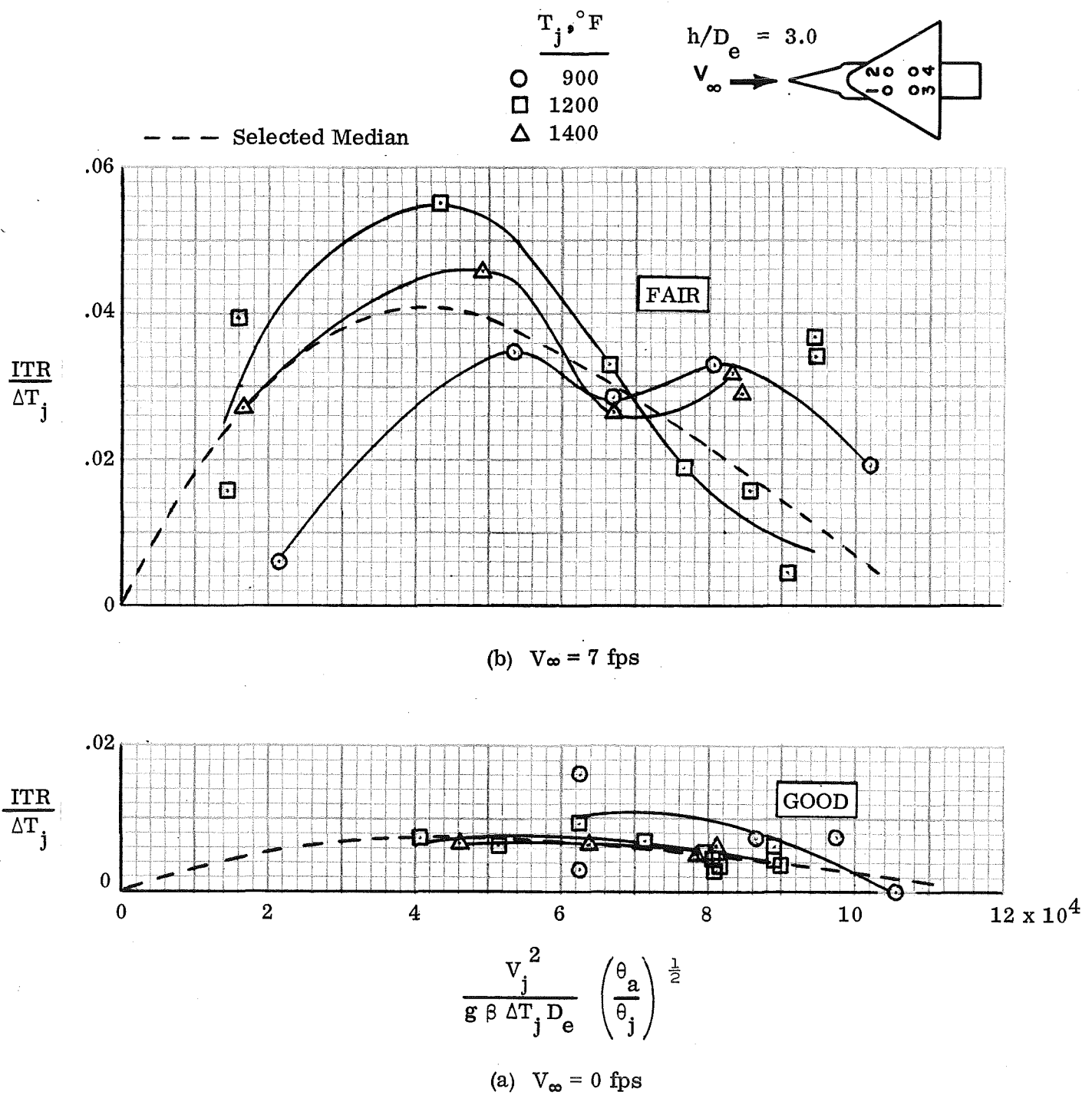
Figure A-2. – Buoyancy Correlation, Top Inlets, Average of Inlets 1 and 2

Figure A-2. — Continued

$T_j, {}^\circ F$ $h/D_e = 3.0$

O   900
□   1200
△   1400

– – –   Selected Median

(e) $V_\infty = 43$ fps

$$\dfrac{ITR}{\Delta T_j}$$

$$\dfrac{V_j^{\,2}}{g\,\beta\,\Delta T_j\,D_e}\left(\dfrac{\theta_a}{\theta_j}\right)^{\frac{1}{2}}$$
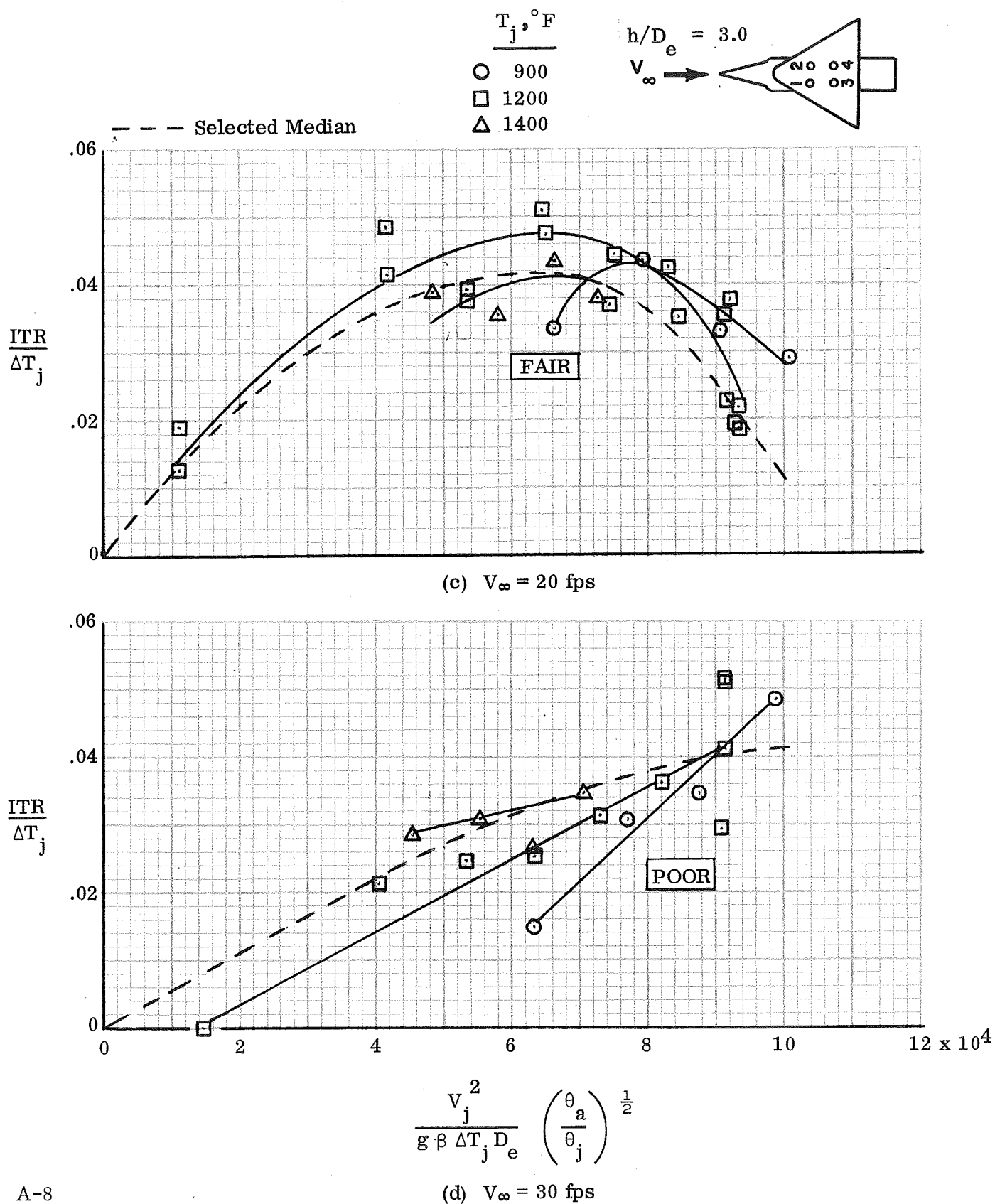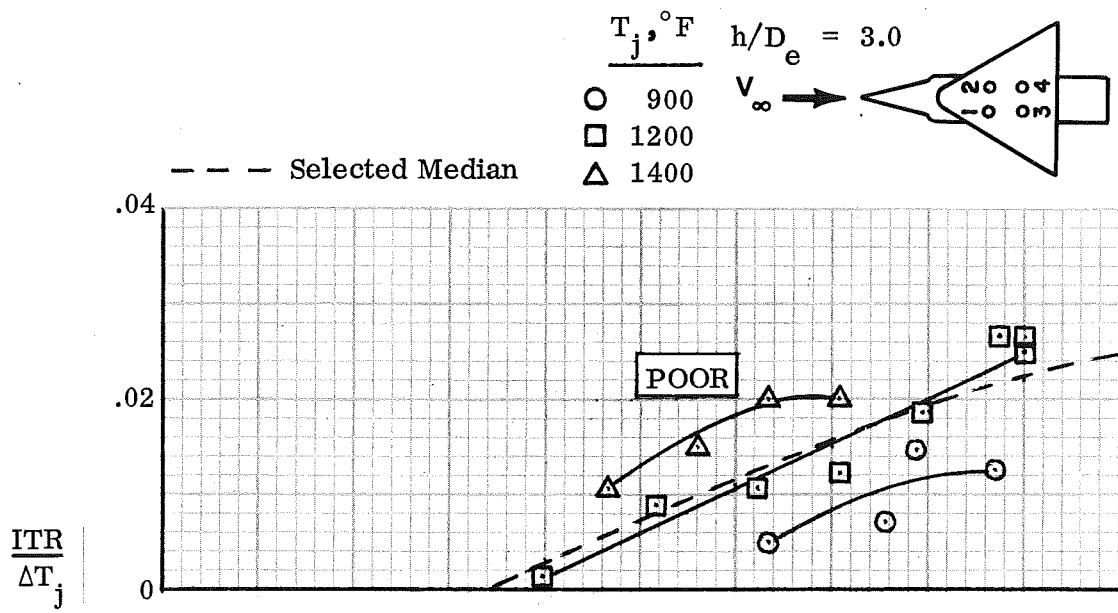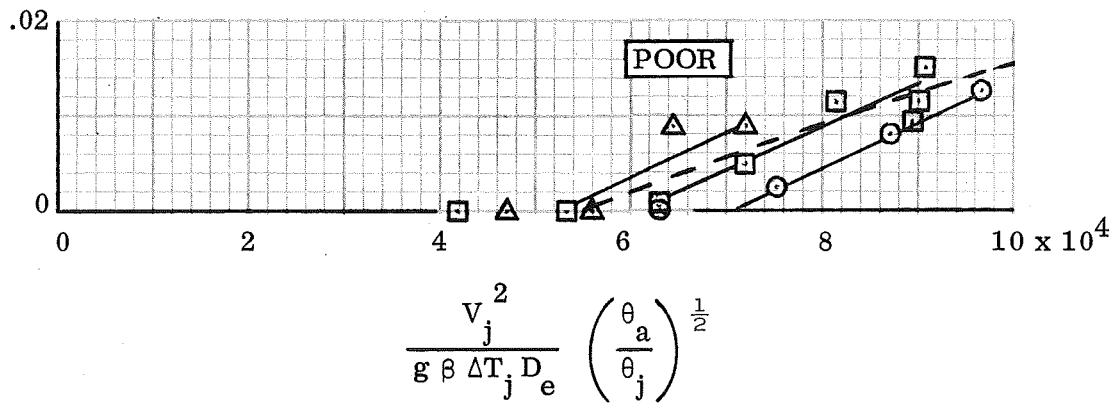
(f) $V_\infty = 53$ fps

Figure A-2. – Concluded

$T_j, °F$

○ 900
□ 1200
△ 1400

— — — Selected Median

$h/D_e = 3.0$

$V_\infty \rightarrow$

.02

$\dfrac{ITR}{\Delta T_j}$

GOOD

0

(a) $V_\infty = 0$ fps

.02

$\dfrac{ITR}{\Delta T_j}$

FAIR

0

(b) $V_\infty = 7$ fps

.02

$\dfrac{ITR}{\Delta T_j}$

GOOD

0

0   2   4   6   8   10 12×10^4

$$\frac{V_j^2}{g \, \beta \, \Delta T_j \, D_e} \left(\frac{\theta_a}{\theta_j} \right)^{\frac{1}{2}}$$

(c) $V_\infty = 20$ fps
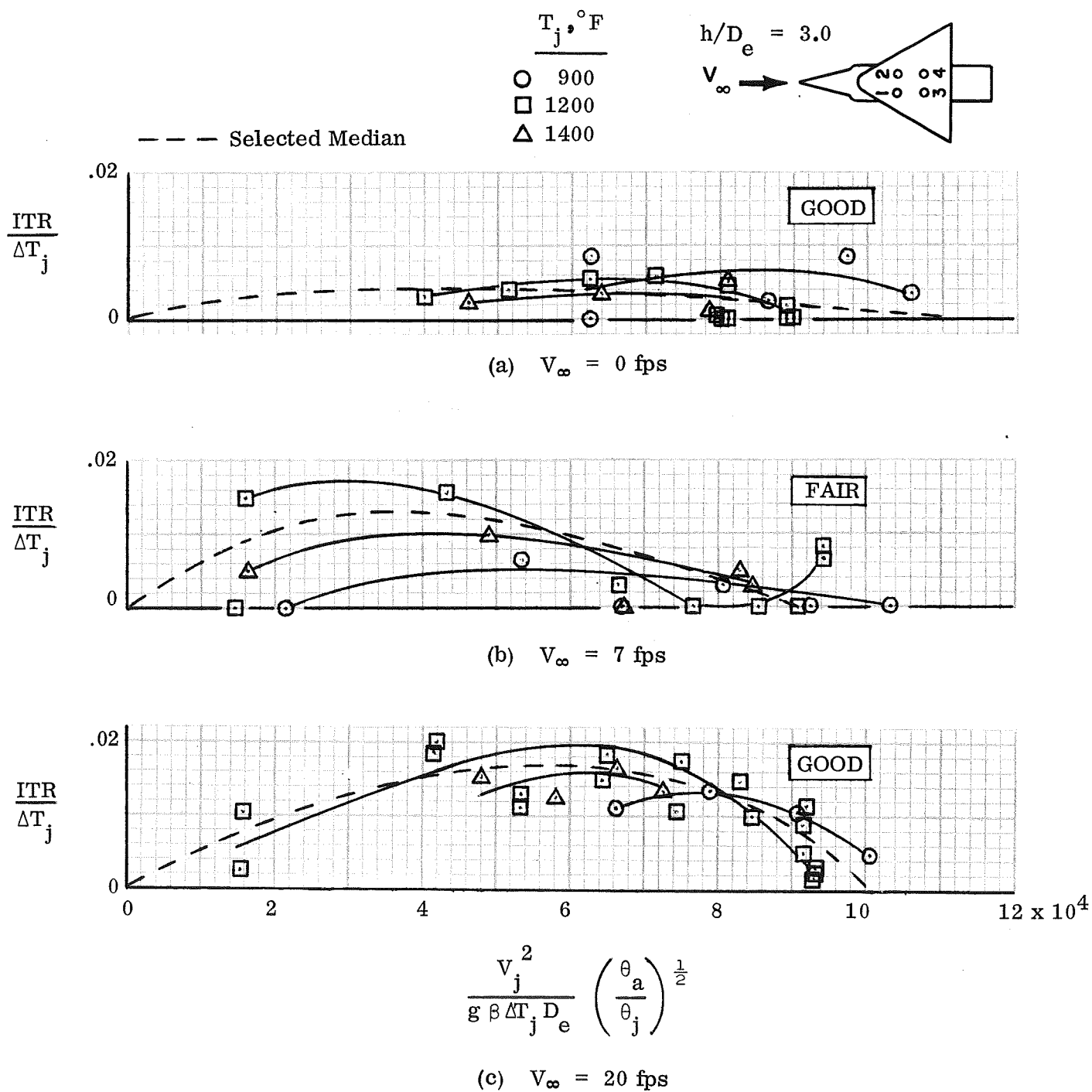
Figure A-3. − Buoyancy Correlation, Top Inlets, Average of Inlets 3 and 4

$$\frac{ITR}{\Delta T_j}$$

(d) $V_\infty = 30$ fps

(e) $V_\infty = 43$ fps

$$\frac{V_j^2}{g\,\beta\,\Delta T_j\,D_e}\left(\frac{\theta_a}{\theta_j}\right)^{\frac{1}{2}}$$
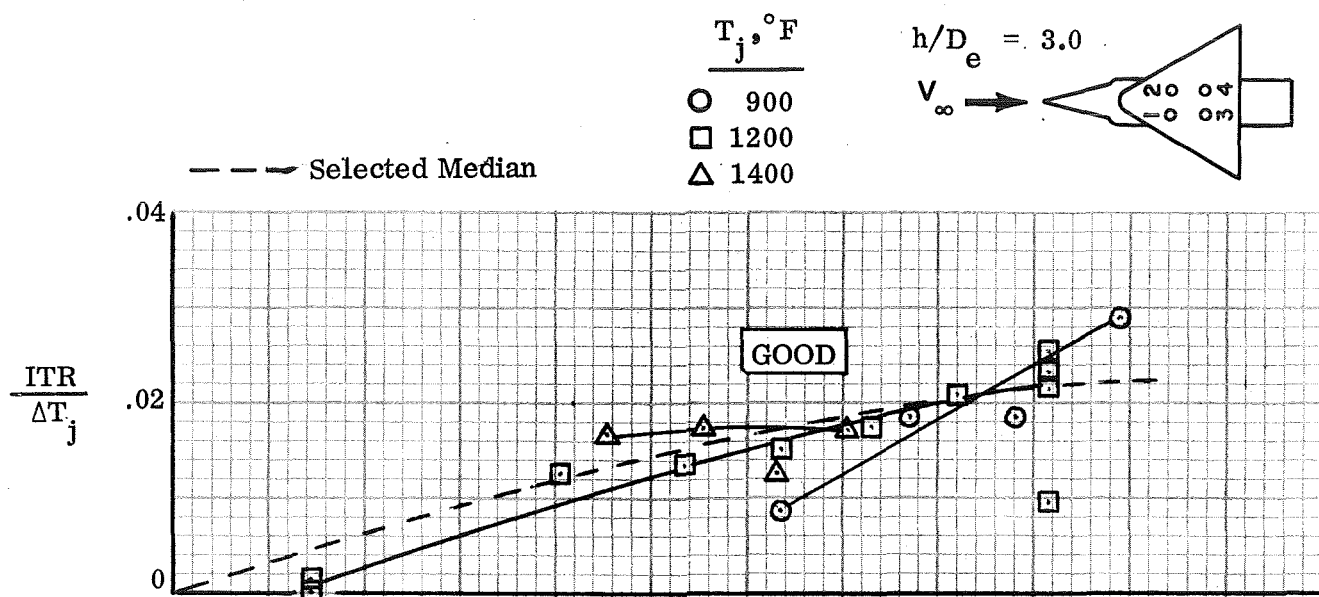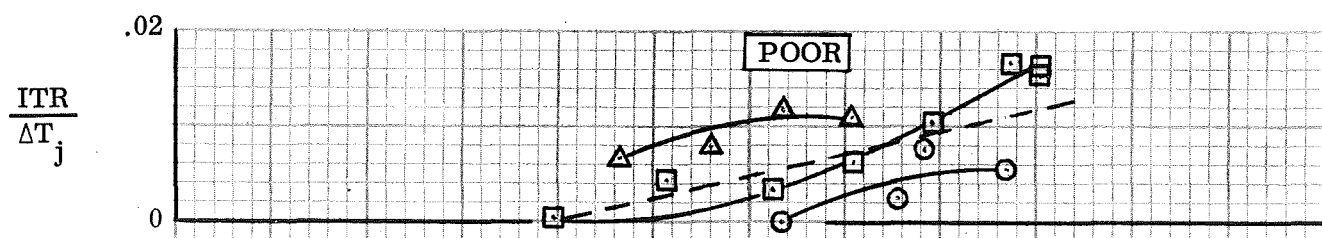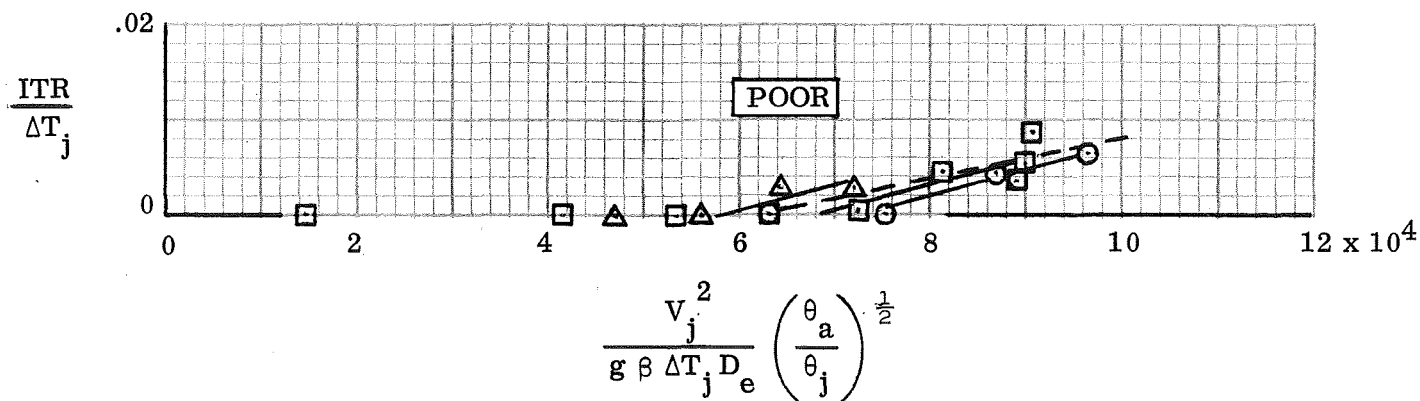
(f) $V_\infty = 53$ fps

Figure A-3. - Concluded

DISTRIBUTION LIST

NAS1-9584   No.
                                                            Copies

NASA Langley Research Center
Hampton, Virginia 23365
Attention: Research Program Records Unit, Mail Stop 122   1
             Raymond L. Zavasky, Mail Stop 117   1
             H. Clyde McLemore, Mail Stop 355   8
             Richard J. Margason, Mail Stop 404   3

NASA Ames Research Center
Moffett Field, California 94035
Attention: Library, Mail Stop 202-3   1
             Jerry P. Barrack, Mail Stop 221-2   3

NASA Flight Research Center
P. O. Box 273
Edwards, California 93523
Attention: Library   1

Jet Propulsion Laboratory
4800 Oak Grove Drive
Pasadena, California 91103
Attention: Library, Mail 111-113   1

NASA Manned Spacecraft Center
2101 Webster Seabrook Road
Houston, Texas 77058
Attention: Library, Code BM6   1

NASA Marshall Space Flight Center
Huntsville, Alabama 35812
Attention: Library   1

NASA Wallops Station
Wallops Island, Virginia 23337
Attention: Library   1

NASA Lewis Research Center
21000 Brookpark Road
Cleveland, Ohio 44135
Attention: Library, Mail Stop 60-3   1
             Nestor Clough, Mail Stop 100-1   3

NASA Goddard Space Flight Center
Greenbelt, Maryland 20771
Attention: Library   1

NASA John F. Kennedy Space Center
Kennedy Space Center, Florida 32899
Attention: Library, Code IS-CAS-42B   1

NASA CR-66965

DISTRIBUTION LIST

NAS1-9584
No.
Copies

National Aeronautics and Space Administration
Washington, D. C. 20546
Attention: Library, Code USS-10   1
            NASA Code RA   1

Lockheed-Georgia Company
86 South Cobb Drive
Marietta, Georgia 30060
Attention: A. Harris   2

Nielsen Engineering and Research, Inc.
3967 East Bayshore
Palo Alto, California 94303
Attention: Jack N. Nielsen, President   1

Vanderbilt University
Department of Mechanical Engineering
Nashville, Tennessee 37203
Attention: Professor John W. Tatom, Box 11, Station B   1

Northrop Corporation
3901 West Broadway
Hawthorne, California 90250
Attention: Gordon R. Hall, Internal Aero & Propulsive
            Branch, Organization 3711-31   2

Dynasciences Corporation
Township Line Road
Blue Bell, Pennsylvania 19422
Attention: Eugene Kisielowski, Director, Aero. Engineering 3

U. S. Army Aviation Materiel Laboratory
Fort Eustis, Virginia 23604
Attention: John White   1

Headquarters
Wright-Patterson Air Force Base, Ohio 45433
Attention: D. Hohler   1
            G. Sealy   1
            Lt. V. K. Smith III   1
            C. Westbrook   1

Department of the Navy
Bureau of Weapons
Washington, D. C. 20525
Attention: Robert Brown, RAPP14   1

Department of the Navy
Bureau of Ships
Washington, D. C. 20360
Attention: G. L. Graves   1

DISTRIBUTION LIST

NAS1-9584

No.
Copies

North American Aviation, Inc.
International Airport
Los Angeles, California   90009
Attention: Rex Carpenter   1
            Gordon Campbell   1

Pratt and Whitney Aircraft
400 Main Street
East Hartford, Connecticut   06108
Attention: W. Sens   1

General Electric Company
1000 Western Avenue
Lynn, Massachusetts   01906
Attention: Klem Gunn   1

Allison Division of General Motors
P. O. Box 894
Indianapolis, Indiana   46206
Attention: C. E. Hockert   1

The Boeing Company
Commercial Airplane Division
P. O. Box 707
Renton, Washington   98055
Attention: Walter Swann   1

The Boeing Company
Vertol Division
Morton, Pennsylvania   19070
Attention: Bernard Fry   1

McDonnell Douglas Corporation
Box 516
St. Louis, Missouri   63166
Attention: Ralph Herzmark   1

McDonnell Douglas Corporation
Aircraft Division
3855 Lakewood Boulevard
Long Beach, California   90808
Attention: W. J. Skillman   1

Lockheed-California
Burbank, California   91503
Attention: Richard Shearer   1
            Donald Seager   1

Ryan Aeronautical Company
2701 Harbor Drive
San Diego, California   92101
Attention: John B. Dain   1

DISTRIBUTION LIST

NAS1-9584   No.
                                                      Copies

Ling-Temco-Vought, Inc.
Dallas, Texas 75221
Attention: K. R. Marsh   1

Fairchild-Hiller
Republic Aviation Division
Farmingdale, Long Island, New York 11735
Attention: G. Rosenthal   1
            J. Lyttle   1

Purdue University
Lafayette, Indiana 47907
Attention: Dr. J. G. Skifstad, Associate Professor,
            Mechanical Engineering   1

NASA Scientific and Technical Information Facility
P. O. Box 33
College Park, Maryland 20740   13 plus reproducible